AD NUMBER
AD381224
CLASSIFICATION CHANGES
TO: **unclassified**
FROM: **confidential**
LIMITATION CHANGES
TO: **Approved for public release, distribution unlimited**
FROM: **Distribution authorized to U.S. Gov't. agencies and their contractors; Administrative/Operational Use; 15 May 1967. Other requests shall be referred to Rocket Propulsion Lab., Air Force Systems Command, Edwards AFB, CA.**
AUTHORITY
31 May 1979, DoDD 5200.10, per doc marking; AFRPL ltr, 5 Feb 1986

SECURITY MARKING

The classified or limited status of this report applies to each page, unless otherwise marked.

Separate page printouts MUST be marked accordingly.

THIS DOCUMENT CONTAINS INFORMATION AFFECTING THE NATIONAL DEFENSE OF THE UNITED STATES WITHIN THE MEANING OF THE ESPIONAGE LAWS, TITLE 18, U.S.C., SECTIONS 793 AND 794. THE TRANSMISSION OR THE REVELATION OF ITS CONTENTS IN ANY MANNER TO AN UNAUTHORIZED PERSON IS PROHIBITED BY LAW.

NOTICE: When government or other drawings, specifications or other data are used for any purpose other than in connection with a definitely related government procurement operation, the U. S. Government thereby incurs no responsibility, nor any obligation whatsoever; and the fact that the Government may have formulated, furnished, or in any way supplied the said drawings, specifications, or other data is not to be regarded by implication or otherwise as in any manner licensing the holder or any other person or corporation, or conveying any rights or permission to manufacture, use or sell any patented invention that may in any way be related thereto.

(UNCLASSIFIED TITLE)

FINAL REPORT OF HIGH ENERGY ADVANCED THROTTLING CONCEPT STUDY

J. P. MITCHELL
Pratt & Whitney Aircraft
Division of United Aircraft Corporation
Florida Research and Development Center

TECHNICAL REPORT AFRPL-TR-67-140
MAY 1967

PATENT SECRECY NOTICE

PORTIONS OF THIS DOCUMENT CONTAIN SUBJECT MATTER COVERED BY A U.S. PATENT OFFICE SECRECY ORDER WITH MODIFYING SECURITY REQUIREMENTS PERMIT. HANDLING SHALL BE IN ACCORDANCE WITH THE PERMIT AS DESCRIBED ON PAGE A AND INDICATED HEREIN. VIOLATORS MAY BE SUBJECT TO THE PENALTIES PRESCRIBED BY, TITLE 35, U. S. C. (1952), SECTIONS 182 AND 186.

Rocket Propulsion Laboratory
Air Force Systems Command
Edwards Air Force Base
[illegible] California

"When U. S. Government drawings, specifications, or other data are used for any purpose other than a definitely related Government procurement operation, the Government thereby incurs no responsibility nor any obligation whatsoever, and the fact that the Government may have formulated, furnished, or in any way supplied the said drawings, specifications, or other data, is not to be regarded by implication or otherwise, or in any manner licensing the holder or any other person or corporation, conveying any rights or permission to manufacture, use, or sell any patented invention that may in any way be related thereto."

"In addition to security requirements which must be met, this document is subject to special export controls and each transmittal to foreign governments or foreign nationals may be made only with prior approval of AFRPL (RPPR/STINFO), Edwards, California 93523."

PATENT SECRECY NOTICE

Material in this publication relating to

DUAL ORIFICE INJECTION

reveals subject matter contained in U. S. Patent Application Serial No. 426,711 entitled "Dual Orifice Impingement Injector", which has been placed under Secrecy Order issued by the Commissioner of Patents. This Secrecy Order has been modified by a **SECURITY REQUIREMENTS PERMIT.**

A Secrecy Order prohibits publication or disclosure of the invention, or any material information with respect thereto. It is separate and distinct, and has nothing to do with the classification of Government contracts.

By statute, violation of a Secrecy Order is punishable by a fine not to exceed $10,000 and/or imprisonment for not more than two years.

A **SECURITY REQUIREMENTS PERMIT** authorizes disclosure of the invention or any material information with respect thereto, to the extent set forth by the security requirements of the Government contract which imposes the highest security classification on the subject matter of the application, except that export is prohibited.

Disclosure of this invention or any material information with respect thereto is prohibited except by written consent of the Commissioner of Patents or as authorized by the permit.

The foregoing does not in any way lessen responsibility for the security of the subject matter as imposed by any Government contract or the provisions of the existing laws relating to espionage and national security.

AFRPL-TR-67-140

(UNCLASSIFIED TITLE)

FINAL REPORT OF HIGH ENERGY ADVANCED THROTTLING CONCEPT STUDY

J. P. MITCHELL

FOREWORD

This Final Report is submitted in compliance with the requirements of Part 1B, Modification No. 3, Contract AF 04(611)-11611, High Energy Advanced Throttling Concept Study, and describes the work done during the program which was conducted during the period May 1966 through May 1967.

This publication was prepared by Pratt & Whitney Aircraft Florida Research and Development Center as report PWA FR-2366.

In the preparation of this report, classified information was extracted from the following Technical Documents, High Energy Advanced Throttling Concept Study (Confidential, declassified after 12 years):

1. Final Report, AFRPL-TR-66-43 (PWA FR-1573), 7 March 1966
2. P&WA Florida Proposal (FP) 66-22, 15 February 1966.

This technical report has been reviewed and approved by the Air Force Project Officer, Mr. R. H. Mickola, AFRPL-RPREC.

Pratt & Whitney Aircraft
Florida Research and Development Center
West Palm Beach, Florida
15 May 1967

CONFIDENTIAL ABSTRACT

(C) This report presents the results of an experimental program conducted under Contract AF 04(611)-11611 to evaluate (1) the throttling capability of dual-orifice injectors with F_2/H_2 propellants and (2) performance of the F_2/H_2 propellants in a high-expansion-ratio (180 to 1) thrust chamber. In the program, 15 combustion firing tests were made with an 8500-lb maximum thrust dual-orifice-injector-chamber assembly at simulated altitude conditions. Tests were made at chamber pressures from 850 to 5 psia, and therefore over a throttling range of 170 to 1. The 6 to 14 mixture ratio range was evaluated. Extremely high performance was recorded in the test program. Specific impulse values of from 441 to 475 seconds were measured at high chamber pressures. Outstanding injector and chamber hardware durability were demonstrated. The total test time accumulated in the tests was 1032 seconds, the longest test being of 184 seconds duration.

CONTENTS

CONTENTS (CONTINUED)

ILLUSTRATIONS

ILLUSTRATIONS (CONTINUED)

ILLUSTRATIONS (CONTINUED)

ILLUSTRATIONS (CONTINUED)

ILLUSTRATIONS (CONTINUED)

TABLES

LIST OF ABBREVIATIONS AND SYMBOLS

Symbol	Description	Units
A	Area	$in.^2$
AC_d	Effective area	$in.^2$
c*	Characteristic exhaust velocity	ft/sec
C	Coefficient	
c	Sonic velocity	ft/sec
C_d	Discharge coefficient	
C_s	Nozzle efficiency	%
D,d	Diameter	in.
F	Force, thrust	lb
FS	Flow split	%
I	Impulse	sec
K	Thrust	1000 lb
L*	Characteristic length	in.
MR	Momentum ratio	
OX	Oxidizer	
P	Pressure	$lb/in.^2$
Q	Heat input	Btu/sec
Re	Reynolds number	
T	Temperature	°F,°R
V	Velocity	ft/sec
$\dot{W},\dot{w}$	Weight flow	lb/sec
g	Gravitational constant	32.17 ft/sec^2
h	Heat transfer coefficient	Btu/ft^2-hr-°R
q	Heat flux	$Btu/sec-in.^2$
r	Mixture ratio	
Δ	Differential	
ϵ	Expansion ratio	
η	Efficiency	%
ρ	Density	lb/ft^3
σ	Standard deviation	
P_c	Chamber pressure	$lb/in.^2$
OPIT	Oxidizer primary injector temperature	°R
ONP	Oxidizer flow nozzle inlet pressure	$lb/in.^2$

LIST OF ABBREVIATIONS AND SYMBOLS (Continued)

Symbol	Description	Units
ONDP	Oxidizer flow nozzle differential pressure	$lb/in.^2$
ONT	Oxidizer temperature at the flow nozzle	°R
OSPDP	Oxidizer secondary injector plate differential pressure	$lb/in.^2$
FODP	Fuel flow orifice differential pressure	$lb/in.^2$
FOT	Fuel temperature at the flow orifice	°R
FIDP	Fuel injector differential pressure	$lb/in.^2$
FOP	Fuel orifice inlet pressure	$lb/in.^2$

Subscripts

a	Ambient
c	Corrected, chamber, combustion
d	Discharge
F	Thrust
f	Fuel
i	Injector, initial
m	Measured
o,ox	Oxidizer
p	Primary
s	Secondary, static
t	Total, throat
T	Theoretical, total
uc	Uncorrected
ul	Upper limit
vac	Vacuum
w	Wall
hs	Half shell

SECTION I
INTRODUCTION

(C) This report presents the results of a study conducted under Contract AF 04(611)-11611 for the evaluation of the throttling performance of dual-orifice injectors with F_2/H_2 propellants at simulated altitude conditions. This program is a follow-on to Contract AF 04(611)-9965, under which dual-orifice injectors were first evaluated with F_2/H_2 propellants. The former contract program, which included only sea level tests, was completed in November 1965, and is reported in Reference 1. Combustion performance of subscale (1000-lb maximum thrust) injectors, as well as that of 8500-lb maximum thrust injectors, was evaluated. The subscale injector program demonstrated injector durability and good performance over the 25- to 320-psia chamber pressure range (i.e., over a thrust range of approximately 10 to 1). The 8.5K injectors provided c* performance that was essentially constant and above 96% over the 28- to 824-psia chamber pressure range (i.e., over a thrust range of approximately 30 to 1). However, because of insufficient hydrogen flow through the Rigimesh faceplate, the 8.5K injector face was burned slightly at chamber pressures up to 300 psia and resulted in a complete injector failure at 824-psia chamber pressure.

(C) In this follow-on program, tests were made at altitude-simulated exhaust conditions with the 8500-lb maximum thrust injector to evaluate performance over its complete throttling range. Fifteen tests were made at chamber pressures from 5 to 850 psia and therefore over a throttling range of 170 to 1. Eight of these tests were made at low chamber pressures between 5 and 30 psia and 7 tests were made in the 300- to 850-psia chamber pressure range to evaluate performance and injector durability. In these altitude tests, a transpiration-cooled injector faceplate more permeable than that in the previously conducted sea level tests was used. Adequate face cooling was demonstrated over the entire 5- to 850-psia chamber pressure range.

(U) The tests were conducted in a recently completed altitude system at FRDC, which has a continuous exhausting capability and is suitable for HF exhaust products. The small-exit-diameter 8.5K sea level chambers were adapted to the large-diameter diffuser of the altitude system by a nozzle extension constructed from an RL10 rocket engine thrust chamber. This extension increased the expansion ratio from approximately 4 to 180 and provided a smooth nozzle contour that was near optimum. Thus, valuable specific impulse performance data as well as c* data were obtained in the tests.

(U) The following sections describe the results of the contract program according to the following breakdown:

Section	II	Summary of Results
	III	Conclusions and Recommendations
	IV	Test Results
	V	Hardware
	VI	Test Facility

SECTION II
SUMMARY OF RESULTS

(C) The throttling capabilities of dual-orifice injectors have been demonstrated with fluorine/hydrogen propellants. Dual orifice injectors were first evaluated with F_2/H_2 propellants in Contract AF 04(611)-9965. In that contract 47 tests were made with 1000-lb and 8500-lb maximum thrust injectors at sea level conditions. In this program 15 additional tests were made with the 8500-lb maximum thrust dual orifice injector. These tests were made at altitude-simulated conditions. Chamber pressures from 5 to 850 psia and mixture ratios from 6 to 14 were evaluated in the altitude tests (table I). The accumulated total firing time was 1032 seconds. This time, together with that of the sea level tests, increases the total firing time obtained with dual orifice injectors in F_2/H_2 combustion tests to 2728 seconds accumulated in 62 tests.

(C) Table I. Test Summaries

	Contract AF 04(611)-9965		Contract AF 04(611)-11611
	1K	8.5K	8.5K
Number of tests	33	14	15
Total firing duration, sec	1512	184	1032
Chamber pressure range, psia	25 to 320	28 to 824	5 to 850
Approximate thrust range	10 to 1	30 to 1	170 to 1
Mixture ratio range	6 to 16	5 to 15	6 to 14

(C) Seven altitude tests were made at high chamber pressures in the 300 to 850 psia range. In these tests c* efficiency and specific impulse data were evaluated at mixture ratios of 8, 10, and 12. Figure 1 presents the c* efficiency data plotted as a function of mixture ratio. All of the c* data were above 96% except for one data point obtained at a chamber pressure of 450 and a mixture ratio of 8.

(C) The specific impulse data obtained in the tests are presented in figure 2. These data are some of the highest ever recorded in a chemical bipropellant rocket combustion firing. Note that specific impulse performance was highest at a mixture ratio of 8 and dropped off with increasing mixture ratio. Some of this drop is due to c* efficiency which also generally decreased with increasing mixture ratio. The remainder of the dropoff in specific impulse performance is due to recombination or kinetic losses. The kinetic losses were calculated by a modified Bray analysis for the 8.5K chamber and compared with the experimental data. The calculated and experimental data were in good agreement as illustrated in figure 3 for the 850-psia chamber pressure level.

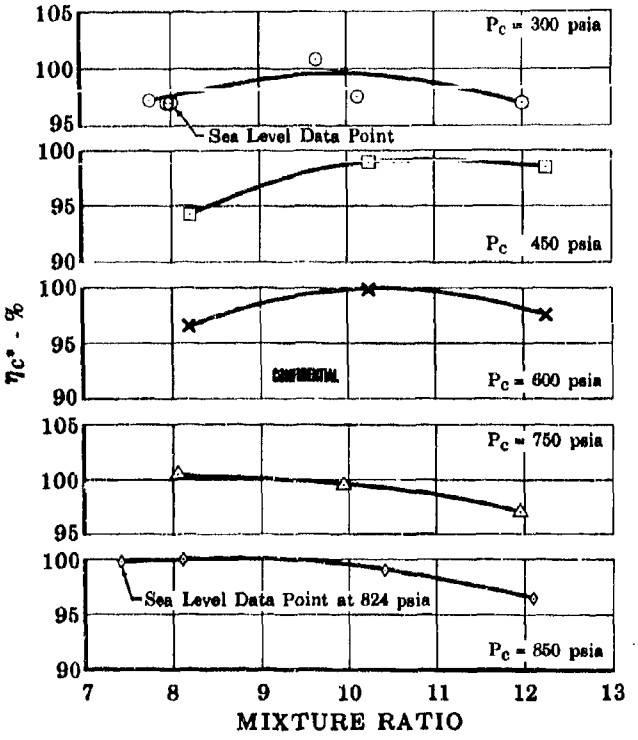

Figure 1. c* Performance FD 20983

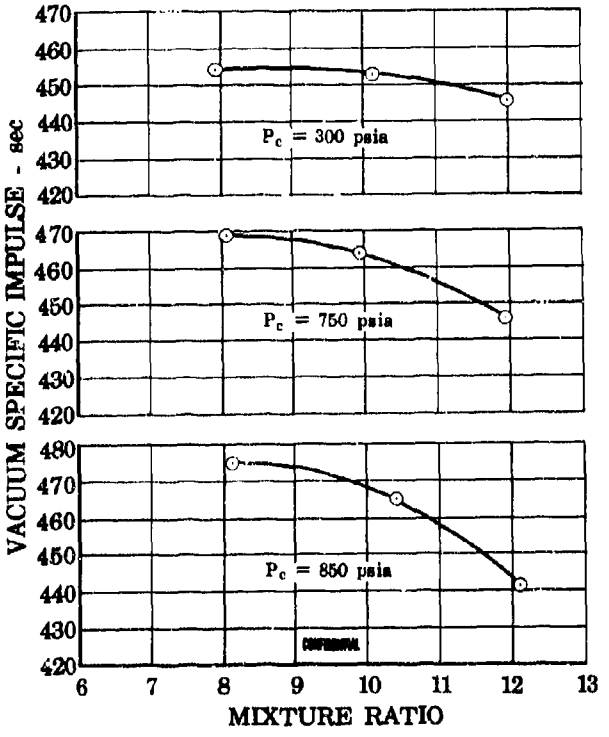

Figure 2. Specific Impulse Performance FD 20942

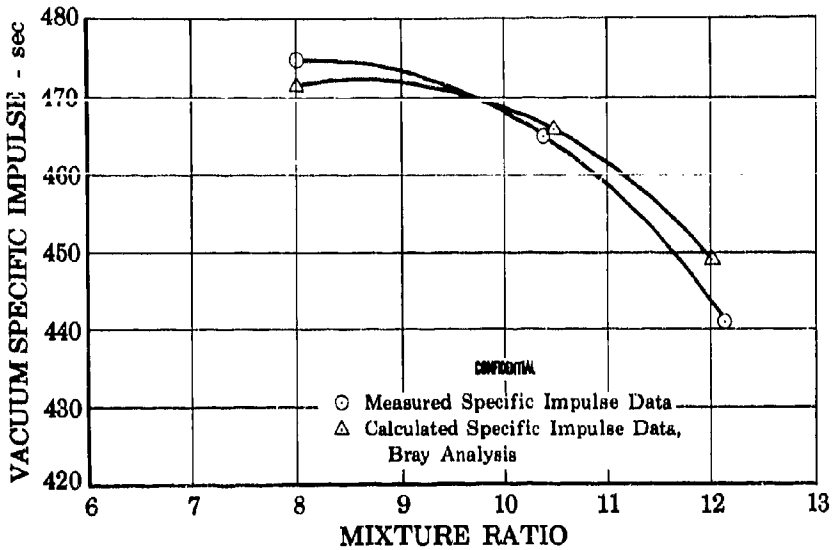

Figure 3. Comparison of Measured and Calculated Performance - P_c = 850 psia FD 20945

(C) Eight tests were made at low chamber pressures in the 5 to 30 psia range to evaluate effects of mixture ratio and injector flow split[1] on c* efficiency. Figure 4 summarizes the results obtained in these low pressure tests. Performance was generally higher at lower mixture ratios as shown. Regarding injector flow split, it was found that stability was best with all of the flow injected through the primary injector. Performance, however, was generally higher at lower flow splits apparently because better mixing between the coaxial fluorine and hydrogen streams occurs with some fluorine flow injected through the fluorine secondary injection orifices. The optimum flow splits that provide highest performance are given in figure 5.

(C) The throttling performance is shown in figure 6 for optimized flow splits. Note that high performance was obtained over a 170 to 1 thrust[2] range.

---

[1] Throughout this report, injector flow split refers to the fluorine flow split between the primary and secondary dual-orifice injectors. The flow split is expressed as the ratio of primary-to-total fluorine flow.

[2] In figure 6 as in other figures in this report, "thrust-%" is used as the independent variable. For simplicity, thrust is assumed to be directly proportional to chamber pressure and therefore "thrust-%" is calculated by the following equation

$$\text{Thrust-\%} = \frac{P_c}{850} \times 100\%.$$

Note that 850 psia is the maximum chamber pressure evaluated with the 8.5K injector.

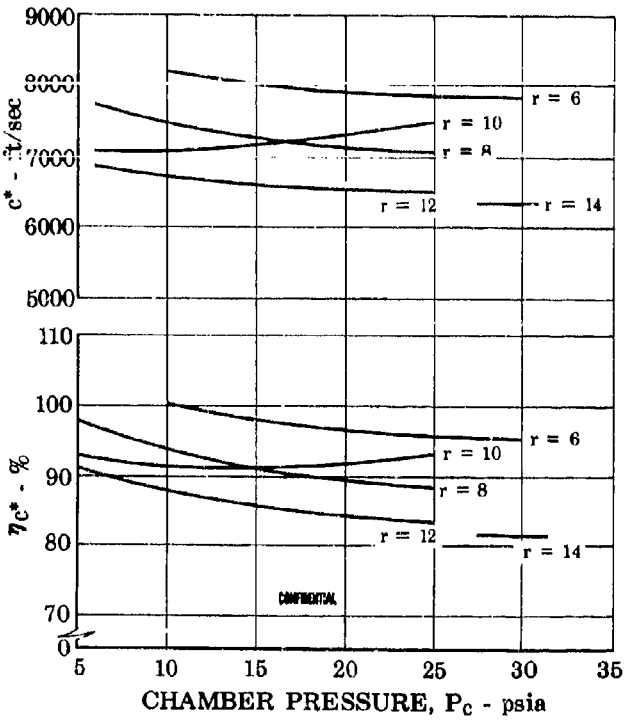

Figure 4. Low Chamber Pressure c* and η_{c^*} Performance at Optimum Flow Splits FD 20965

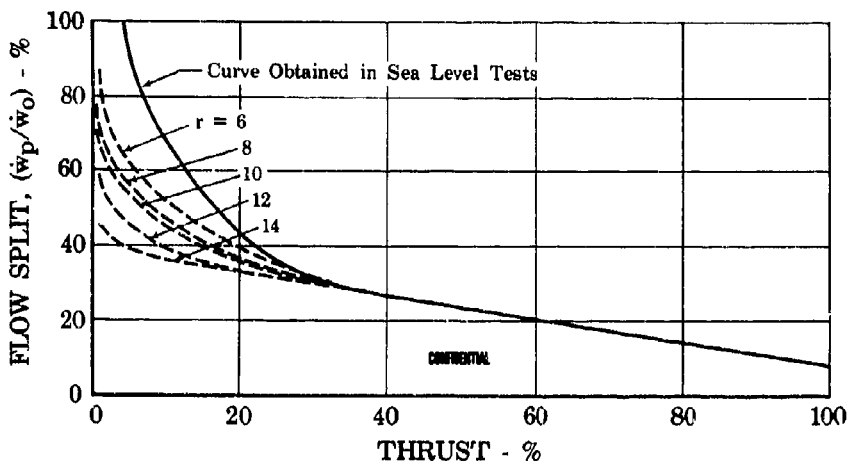

Figure 5. Variation of Optimum Injector Flow Split With Thrust and Mixture Ratio FD 20944

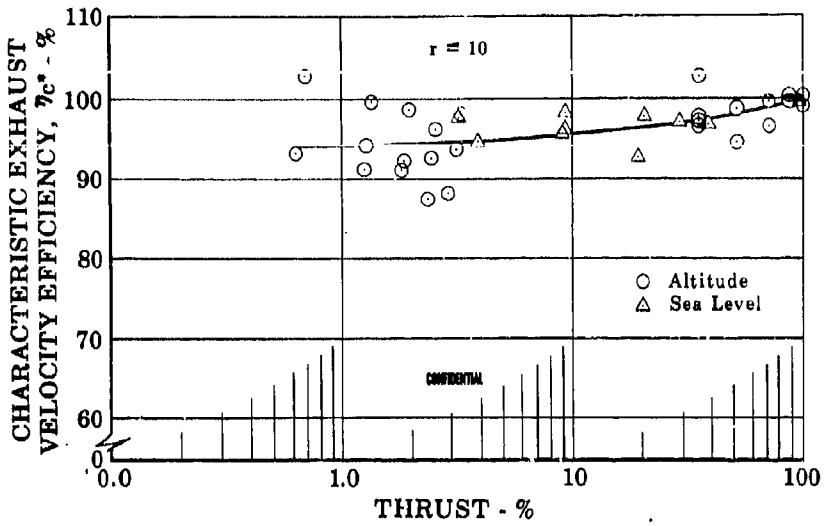

Figure 6. 8.5K Injector Throttling Performance for $r \leq 10$ and Optimum Injector Flow Splits FD 20988

(C) Exceptionally good hardware durability was demonstrated in the test program. The durability is particularly impressive when the wide range of pressures and heat fluxes that were covered and the extended test durations accomplished are considered. Tests of 35 seconds duration were made at 850, 750, 600, 450, and 300 psia. In each test mixture ratios of 8 to 12 were evaluated. In the 850-psia test the throat heat flux was approximately 30 Btu/in^2 sec. At the low chamber pressures the test time accumulated in 8 tests was 827.4 seconds and the longest test was just over 3 minutes.

SECTION III
CONCLUSIONS AND RECOMMENDATIONS

A. CONCLUSIONS

(C) Dual-orifice injectors will provide high combustion performance with fluorine/hydrogen propellants over a wide thrust range. The 8.5K dual-orifice injector tested in the program provided good performance over a 170-to-1 thrust range.

(C) Dual-orifice injectors can be designed for good fluorine compatibility. With the exception of minor face burning, there was no injector hardware damage after 1032 seconds operating time and 15 tests. Outstanding durability was also demonstrated for the copper workhorse chamber that was convectively cooled by hydrogen in the tests. This durability is impressive because the chamber was operated at steady-state conditions for 35 seconds at high chamber pressures where the throat heat flux was as high as 30 Btu/in^2-sec.

B. RECOMMENDATION

(C) Additional tests should be made using the residual 8.5K hardware to evaluate effects of throat radius-of-curvature on specific impulse performance. In the tests made in this program, it was found that specific impulse decreased with increasing mixture ratio because of recombination or kinetic losses in the sharp-corner-throat chamber. Tests should be made with other chambers to evaluate the theoretical advantage of large radius of curvatures.

SECTION IV
TEST RESULTS

A. GENERAL

(C) Fifteen altitude tests were made at chamber pressures from 5 to 850 psia; the total firing time was 1032 seconds; and mixture ratios from 6 to 14 were evaluated. Two types of tests were made. At low chamber pressures between 5 and 30 psia, mixture ratio and fluorine-dual-orifice-injector flow split excursions were made. At high chamber pressure between 300 and 850 psia where the flow contribution of the primary injector is small, only mixture ratio excursions were accomplished. The low chamber pressure tests were programed to obtain 12 data points per test while operating at a given chamber pressure. The procedure followed was to make a fluorine flow split excursion (involving operation at three different flow splits) at four different mixture ratios. At each data point the 8.5K engine was operated from 5 to 10 seconds to obtain steady-state conditions. In the high chamber pressure tests, mixture ratio excursions were made in separate tests at chamber pressures of 300, 450, 600, 750, and 850 psia. The high chamber pressure tests were of 35 seconds duration; at each chamber pressure and mixture ratio the engine was operated for approximately 10 seconds to establish steady-state conditions. A discussion of the tests is presented in the following paragraphs. Paragraph B describes important aspects of each test and paragraph C presents the test data and performance discussions.

B. TEST SUMMARY

(C) A test summary is presented in table II. As indicated, a flow split and mixture ratio excursion test at 30 psia was attempted in test No. 2 following the initial checkout test. However, the inner fluorine injector seals began to leak and the test was automatically aborted. To prevent leakage into the seal cavity, the cavity was pressurized with nitrogen at a slightly higher pressure than the fluorine injector supply pressures. In test No. 3 additional fluorine leakage into the cavity occurred at the 100% flow split (i.e., with all of the flow through the primary injector) 40 seconds into the test and consequently the Teflon-coated O-rings were replaced with aluminum-plated stainless steel V-type seals for subsequent tests. The nitrogen pressurization system for the seal cavity was retained and no additional injector seal problems were encountered. Additional discussions of the injector seals can be found in Section V, Hardware Descriptions.

(C) Inspection of the injector faceplate after test No. 3 revealed that the faceplate was deflected rearward approximately 0.025 inch and was slightly burned near its center. The deflection occurred because the faceplate was inadequately supported at its center. A spacer was placed behind the faceplate in subsequent tests to prevent deflection. To prevent additional faceplate burning, 78 small (0.020-in. dia) holes were drilled in the center portion of the faceplate (see Section V, paragraph C2) through which some of the hydrogen fuel was injected to provide additional face cooling by breaking up the recirculation flow pattern in the center of the injector.

(C) Table II. 8.5K Test Summary

Test No.	Chamber Pressure, psia	Mixture Ratio	Duration, sec	Flow Split, $\dot{w}_p/\dot{w}_o$, %	Remarks
1	18	10	15.1		Satisfactory test. Checkout test. All systems operated properly.
2			1.2		Test was prematurely aborted when the monitored pressure between the double fluorine injector seals rose, indicating leakage. A nitrogen pressurization system was added to the interseal cavity and the cavity was pressurized above the anticipated injector fluorine pressures for subsequent tests.
3	30	14	39.8	50-100	Satisfactory test. Test was scheduled for 200 seconds but was aborted by the test engineer when the injector faceplate deflected rearward, thereby reducing the combustion efficiency and increasing propellant flow rates. The increased flow rates increased the fluorine injector pressures, which then exceeded the interseal nitrogen cavity pressure causing fluorine leakage and an abort. The faceplate will be supported to prevent deflection in future tests. Permeable faceplate replaced.
4	25	6-12	116.6	50-100	Satisfactory test. Mixture ratio and flow split excursions. All twelve data points obtained. Slight injector face burning. Suspect that burning took place during engine shutdown. Fuel lag time at shutdown was increased to prevent further face burning.

(C) Table II. 8.5K Test Summary (Continued)

Test No.	Chamber Pressure, psia	Mixture Ratio	Duration, sec	Flow Split, $\dot{w}_p/\dot{w}_o$, %	Remarks
5	20	6-12	141.7	50-100	Satisfactory test. Mixture ratio and flow split excursions. All twelve data points obtained. No further injector face burning.
6	15	6-12	158.1	50-100	Satisfactory test. Mixture ratio and flow split excursions. All twelve data points obtained.
7	10	6-12	170.9	50-100	Satisfactory test. Mixture ratio and flow split excursions. All twelve data points obtained.
8	5	6-12	184.0	50-100	Satisfactory test. Mixture ratio and flow split excursions. All twelve data points obtained. Additional injector face burning occurred due to extremely low coolant flow through the injector faceplate. Faceplate was replaced with a repaired faceplate that was used in tests No. 1 through 3.
9	300	8-10	26	17	Satisfactory test. Mixture ratio excursion test was scheduled for 35 seconds but was automatically aborted when during the final mixture ratio change the mixture ratio momentarily exceeded the maximum allowable of 15. For subsequent tests this abort will be disarmed for 2 seconds when the mixture ratio changes are made. Slight injector face burning occurred during start transient. Initial valve settings were changed to avoid further burning.
10	450	8-12	35	15	Satisfactory test. Mixture ratio excursion. No further injector face burning.

(C) Table II. 8.5K Test Summary (Continued)

Test No.	Chamber Pressure, psia	Mixture Ratio	Duration, sec	Flow Split, $\dot{w}_p/\dot{w}_a$, %	Remarks
11	600	8-12	35	8.3	Satisfactory test. Mixture ratio excursion. Test stand was temporarily down so the faceplate burning that occurred during test No. 9 was repaired. Nozzle extension was damaged during this test and was replaced. A Mae West pressure bleed was installed on replacement nozzle extension to avoid the type of failure that occurred. A check of the thrust data revealed erroneous readings for test No. 9. The thrust system was checked and it was decided to rerun test No. 9.
12	300	8-12	35	17	Satisfactory test. Mixture ratio excursion. Repeat of test No. 9 giving satisfactory thrust results.
13			3.9		750 psia chamber pressure test was attempted. Test was prematurely aborted when the differential pressure across the injector secondary oxidizer plate became excessive during the start transient. The start transient time was lengthened. No apparent injector damage was noted.
14	750	8-12	35	7.5	Satisfactory test. Mixture ratio excursion. The nozzle extension was damaged when fuel tank pressure fell off during the test. Four coolant tubes were blown just aft of the Mae West and some of the braze between the tubes was melted in the vicinity of the coolant exit manifold. Steps were taken to conserve hydrogen prior to the actual run to keep up the tank pressure.
15	850	8-12	35	7.5	Satisfactory test. Mixture ratio excursion. No further nozzle extension or injector damage.

CONFIDENTIAL

CONFIDENTIAL

(C) Tests No. 4, 5, 6, 7, and 8 were made at chamber pressures of 25, 20, 15, 10, and 5 psia. During each test all programed test points were achieved; mixture ratios of 6, 8, 10, and 12, and flow splits of 50, 75, and 100% were evaluated. During these low chamber pressure tests, the flow split and mixture ratio excursions were accomplished by using two multiposition switches: one that changed the mixture ratio and the other that changed the position of the flow divider valve. In the tests, the engine was started at a mixture ratio of 6 and with a 50% flow split. After chamber pressure had been steady for approximately 5 to 10 seconds, the flow divider valve switch was manually adjusted by the test engineer to obtain first 75% and then 100% flow splits, all at a mixture ratio of 6. Next the mixture ratio was changed to 8 where another flow split excursion was made. Subsequently, flow split excursions were made at 10 and 12 following the same procedure.

(C) Following test No. 4, additional slight face burning was noted. The fuel lag time at shutdown was increased and no additional burning was noted until test No. 8 at 5 psia chamber pressure. The face burning which occurred during this test is attributed to the extremely low fuel flow and hence face cooling flow through the permeable faceplate.

(C) Test No. 9, a 26-second mixture ratio excursion at 300 psia chamber pressure, was the first of the high chamber pressure tests. Data at mixture ratios of 8 and 10 were obtained; however, the test was terminated when the mixture ratio was changed to 12. A momentary high mixture ratio ($r > 15$) occurred, thus triggering the high mixture ratio automatic abort. This automatic abort was disarmed for 2 seconds during the mixture ratio changes in subsequent tests to avoid this problem. A post-test inspection of the injector faceplate following test No. 9 revealed slight faceplate burning near the center. The burning was attributed to a high mixture ratio transient. The start transient was changed to avoid high mixture ratios and further faceplate burning.

(C) Mixture ratio excursions covering the 8 to 12 ratio were successfully made in test numbers 10 and 11 at 450 and 600 psia chamber pressure tests, respectively. Following these tests, data analysis revealed erroneous thrust measurements for the first three high chamber pressure tests (tests No. 9, 10, and 11). The thrust system was repaired as described in Appendix III. Also following test No. 11 an inspection of the hardware revealed that several tubes in the nozzle extension had been pushed away from the nozzle extension pressure shell (which is referred to as the "Mae West") thus destroying the smooth nozzle contour. This occurred when an excessive pressure built up between the stainless steel tubes and the Mae West. Photographs of the bulged tubes can be found in Section V, paragraph C. The nozzle extension was subsequently replaced and a Mae West pressure bleed was added to avoid a similar failure. At this time the injector faceplate was removed and more 0.020-inch diameter holes were drilled in the faceplate to provide additional cooling.

(C) After the test hardware had been reinstalled in the test stand and the thrust measurement system repaired, another test (test No. 12) was made at 300 psia chamber pressure to check out the thrust system. Good thrust data were obtained in this test at all three mixture ratios: 8, 10, and 12. The target chamber pressure for test No. 13 was 750 psia. This test was automatically aborted during the start transient, however. The abort occurred because the pressure increased faster in the fluorine injector secondary manifold than in the fuel injector manifold, thus causing a high pressure differential across the secondary injector spudplate, which triggered an automatic abort. A post-test inspection of the injector revealed no damage. The chamber pressure ramp rate was decreased and test No. 14 was a successful 35-second mixture ratio excursion at the 750 psia chamber pressure level. However, during the test the fuel supply tank pressure dropped off from 2000 psia to approximately 1700 psia, because of excessive venting of the tank and its tube trailer supply just before the test. This decrease in supply pressure resulted in decreased coolant flow through the chamber and nozzle extension. A post-test inspection of the hardware revealed nozzle extension damage. Four of the 180 coolant tubes were burst open on the inside diameter of the extension. The final test (test No. 15) was made with the nozzle extension. This test was a successful 35-second mixture ratio excursion at a chamber pressure of 850 psia. A post-test inspection revealed no damage to the injector and sea level chamber and no further damage to the nozzle extension. Photographs of all the test hardware are presented in Section V, paragraph C.

C. PERFORMANCE DATA

1. Tabulated Test Data

(U) The performance data obtained in the altitude tests are presented in table III. The equations used to compute the performance parameters given in the table are presented in Appendix II. With the exception of the data obtained in test No. 3, the performance data represent averages obtained for steady-state periods of from 2 to 6 seconds duration. In test No. 3, because the test was prematurely aborted, it was necessary to use shorter data average periods.

(U) The characteristic exhaust velocity (c*) and characteristic exhaust velocity efficiency (η_{c^*}) data were computed from two different measurements of chamber pressure. One chamber pressure measurement was taken at the chamber wall just upstream of the point where the chamber begins to converge to the throat. The other chamber pressure measurement was taken near the injector face.

(U) The c* and η_{c^*} computed from the face-tap chamber pressure measurements are corrected for a momentum loss of 0.5%. The η_{c^*} for both the chamber tap and face tap were also corrected for (1) the measured heat loss to the chamber and (2) the chamber throat flow discharge coefficient. The performance corrections are discussed in subparagraph 5. In the performance discussions presented in subsequent subparagraphs, c* data obtained from the chamber-tap chamber pressure measurements are used because these data do not require a momentum-loss correction.

(C) Table III. 8.5K Injector Altitude Test Results

Test No.	Chamber Pressure, psia	Thrust, %	Total Propellant Flow, pps	Mixture Ratio	c* Face Tap, ft/sec	c* Chamber Tap, ft/sec	ηc^* Face Tap, %	ηc^* Chamber Tap, %	Vacuum Thrust, lb	I_{vac}, sec	ηI_{vac}, %	ηC_F, %	Ox Frt Inj ΔP, psid	Ox Rec Inj ΔP, psid	Ox Ave Inj Vel, ft/sec	Fuel Inj ΔP, psid	Fuel Inj Vel, ft/sec	Momentum Ratio	Ox Flow Split, %	Peak-to-Peak P_c', psi	P_c Frequency, cps	
1			Checkout Test																			
2			Abort																			
3	30.2	3.54	0.93	14.1	6436	6376	80.4	82.3					15.8	2.86	21.2	3.6	1377	2.4	50	1.0		
	30.5	3.58	1.01	14.3	5984	5910	77.6	76.6					28.7	1.69	34.5	4.3	1370	1.6	75	0.3		
	31.1	3.66	1.14	14.1	5344	5295	68.9	68.1					135.9	0	39.2	5.2	1350	1.6	100	0.8		
4	26.7	3.14	0.88	5.9	7377	7712	91.6	93.2					18.1	2.45	42.8	8.7	2103	5.8	50	2.1		
	27.9	3.28	0.87	5.9	7532	8098	96.2	97.9					24.2	1.38	49.9	8.4	2122	4.7	75	1.8		
	28.2	2.73	0.88	5.9	6607	6724	80.2	81.6					68.3	0	133.6	9.8	2602	2.1	100	1.2		
	21.8	2.56	0.88	7.8	6149	6267	76.6	77.8					71.4	0	133.3	6.9	2182	1.3	100	0.6		
	24.8	2.91	0.89	7.8	6943	7060	86.3	87.7					32.9	1.17	66.9	6.5	1938	2.3	75	1.4		
	24.9	2.92	0.89	7.8	6955	7067	86.6	88.0					8.4	1.49	15.8	6.6	1911	9.8	50	1.3		
	25.8	3.03	0.71	9.7	7036	7154	89.2	89.6					7.7	1.42	14.1	4.9	1357	7.2	50	1.2		
	26.9	3.16	0.71	9.7	7332	7457	93.5	93.4					13.4	1.09	24.4	4.8	1490	4.0	75	2.0		
	21.9	2.38	0.71	9.7	5985	6078	76.0	76.4					43.9	0	76.8	4.5	1823	1.6	100	0.9		
	19.4	2.28	0.71	11.3	5283	5352	68.1	68.2					47.3	0	84.7	4.5	1759	1.2	100	0.4		
	22.4	2.64	0.71	11.5	6125	6209	78.7	78.9					16.9	0.93	29.3	4.2	1314	2.8	75	1.7		
	23.6	2.78	0.71	11.5	6435	6529	82.7	82.9					7.5	1.35	13.5	4.1	1440	5.8	50	2.5		
5	22.1	2.59	0.55	6.0	7459	7530	91.0	91.9					6.8	1.40	16.8	7.8	2299	14.4	50	1.2		
	22.0	2.58	0.55	6.0	7769	7858	94.7	95.8					12.5	0.75	30.4	7.7	2225	7.9	75	1.3		
	19.4	2.38	0.55	6.0	6854	6934	83.7	84.7					42.1	0	98.2	8.1	2512	2.7	100	0.5		
	17.7	2.08	0.55	7.8	6200	6257	77.6	77.8					48.2	0	109.1	5.9	2174	1.6	100	0.4		
	18.0	2.11	0.56	7.9	6260	6306	78.5	78.9					17.2	0.69	48.1	6.0	2139	3.7	75	2.2		
	19.9	2.34	0.56	7.9	6896	6962	86.4	87.2					5.5	1.11	13.5	5.9	1937	11.8	50	1.5		
	19.8	2.33	0.57	9.8	6798	6858	86.7	87.5					4.9	1.13	11.4	4.5	1623	9.2	50	1.4		
	21.0	2.47	0.57	9.8	7192	7265	91.7	92.7					8.7	0.84	19.2	4.3	1532	5.2	75	0.9		
	17.3	2.04	0.57	9.8	5930	5997	75.8	76.5					29.4	0	62.0	4.8	1863	1.9	100	0.4		
	15.7	1.84	0.57	11.7	5367	5400	69.4	69.8					31.6	0	66.3	3.9	1741	1.6	100	0.4		
	18.3	2.15	0.57	11.6	6200	6242	80.1	80.6					9.9	0.73	22.4	3.7	1507	3.7	75	1.0		
	19.5	2.29	0.57	11.7	6609	6662	85.4	86.1					4.4	1.14	10.3	3.6	1394	7.6	50	1.1		
6	15.8	1.86	0.41	5.8	7314	7554	91.9	92.4					8.8	1.42	29.3	7.0	2378	8.7	50	1.5		
	16.9	1.99	0.41	5.8	8040	8091	98.2	98.8					16.2	0.98	52.0	6.6	2189	4.5	75	1.2		
	15.0	1.76	0.41	5.8	7130	7198	87.4	88.0					45.8	0	147.6	6.9	2473	1.8	100	0.8		
	14.4	1.69	0.42	7.7	6722	6764	84.4	84.9					47.0	0	147.5	5.0	2070	1.2	100	0.5		
	15.6	1.83	0.42	7.7	7240	7272	90.7	91.1					15.5	1.02	46.9	5.4	2008	3.5	75	2.1		
	15.8	1.86	0.42	7.7	7321	7351	92.0	92.4					7.0	1.29	20.9	5.3	1904	7.3	50	2.9		
	15.4	1.81	0.42	9.7	7090	7117	90.9	91.2					7.1	1.39	19.5	4.1	1648	5.3	50	2.7		
	15.3	1.80	0.42	9.6	7043	7068	90.2	90.6					10.8	0.88	22.4	4.0	1571	3.3	75	1.1		
	12.3	1.45	0.42	9.6	5607	5702	73.2	73.2					27.8	0	77.4	4.6	1996	1.7	100	0.4		
	12.1	1.42	0.43	11.5	5490	5593	72.8	72.8					30.8	0	83.5	3.5	1745	1.1	100	0.4		
	14.6	1.72	0.43	11.6	6634	6662	86.1	86.5					13.1	0.93	39.7	3.2	1437	2.0	75	1.2		
	15.0	1.77	0.43	11.9	6827	6850	89.0	89.3					6.3	1.41	18.3	3.2	1378	3.9	50	1.8		
7	10.97	1.29	0.28	6.2	7624	7655	94.2	94.6					12.70	1.38	39.1	5.18	2297	4.0	50	1.62		
	11.45	1.35	0.28	6.2	8020	8046	99.0	99.3					17.10	0.91	81.0	4.84	2114	9.7	75	1.66		
	11.19	1.32	0.28	8.1	7817	7855	96.3	97.0					35.79	0	171.8	4.84	2114	1.3	100	0.66		
	10.82	1.27	0.29	8.0	7377	7407	93.7	94.1					42.16	0	192.8	3.72	1821	0.7	100	0.37		
	10.65	1.25	0.29	8.0	7277	7288	92.1	92.5					22.73	1.16	105.1	3.86	1851	1.4	75	3.27		
	10.74	1.27	0.29	8.1	7317	7330	92.9	93.1					12.48	1.35	55.3	3.73	1726	2.5	50	2.21		
	10.54	1.24	0.29	9.9	7040	7049	90.9	91.0					11.83	1.55	50.2	3.06	1561	2.0	50	1.56		
	9.28	1.09	0.29	9.9	6206	6216	80.2	80.4					15.32	1.06	85.2	3.44	1760	1.7	75	2.31		
	9.74	1.14	0.29	9.9	6528	6542	84.3	84.5					28.34	0	122.0	3.35	1706	0.9	100	1.12		
	9.32	1.10	0.29	11.9	6123	6193	80.9	81.2					31.93	0	135.1	2.77	1521	0.6	100	0.56		
	9.80	1.15	0.30	11.9	6489	6505	84.9	85.1					18.00	1.29	74.9	2.71	1441	1.0	75	1.59		
	9.96	1.17	0.30	11.9	6580	6594	86.2	86.4					12.34	1.89	51.0	2.77	1437	1.3	50	1.41		
8	5.72	0.67	0.15	6.1	7508	7521	94.6	94.7					13.57	1.84	142.7	3.05	2261	1.9	50	1.25		
	5.10	0.60	0.15	6.2	6796	6814	85.5	85.8					14.93	1.49	137.4	3.35	2436	1.8	75	1.00		
	6.38	0.75	0.14	8.2	8560	8569	107.2	107.3					34.73	0	330.3	2.73	2014	0.8	100	1.59		
	5.52	0.65	0.15	8.1	7277	7272	93.9	93.8					36.30	0	327.9	2.26	1830	0.4	100	1.69		
	6.04	0.71	0.15	8.1	7930	7881	102.4	102.4					18.61	1.56	183.8	2.17	1692	0.8	75	1.03		
	5.34	0.63	0.15	8.0	6966	6977	90.1	90.2					11.13	1.86	96.6	2.49	1928	1.6	50	0.69		
	5.07	0.60	0.15	10.4	6343	6346	86.1	86.1					9.64	1.91	80.4	2.01	1649	1.3	50	0.90		
	5.48	0.64	0.15	10.1	7078	7077	93.0	93.0					12.42	1.80	104.5	1.95	1514	0.9	75	0.79		
	4.43	0.52	0.15	10.2	5767	5733	76.0	75.5					21.15	0	178.8	2.40	1881	0.7	100	1.60		
	4.37	0.51	0.15	12.4	5643	5622	75.4	75.2					26.12	0	217.6	1.93	1606	0.4	100	2.28		
	5.29	0.62	0.15	12.4	6796	6794	90.7	90.7					17.16	2.09	141.1	1.72	1340	0.5	75	1.01		
	5.15	0.60	0.15	12.3	6579	6585	87.9	88.0					11.34	2.16	93.0	1.72	1340	0.8	50	0.81		
9	301	35.6	7.359	7.73	8174	8081	98.3	97.3					84.3	20	33.0	53	2045	5.06	17.0	12		135
	303	35.8	7.215	9.66	8250	8242	100.6	100.6					80.5	11	32.3	35	1685	3.38	16.5	4		135
10	443	52.1	11.06	8.22	7987	7850	95.9	94.3					141	26	43.0	75	2031	3.50	14.3	18		165
	442	52.0	10.70	10.26	8138	8087	99.0	98.4					133	18	44.3	47	1659	2.30	14.4	9		155
	442	52.0	10.87	12.26	7960	7960	98.0	97.9					138	20	45.3	36	1458	1.66	14.1	0		0
11	601	70.7	14.66	8.17	8134	8037	97.4	96.2					83.2	46	51.4	100	2032	1.08	8.40	25		172
	603	70.9	14.39	10.26	8211	8215	99.7	99.7					80.4	41	51.0	58	1589	1.89	8.25	0		0
	603	70.9	14.90	12.25	7931	7937	97.3	97.4					89.0	45	53.7	45	1389	1.33	8.25	0		0
12	303	35.6	7.38	7.92	8021	8037	96.6	96.8	3330	454	92.7	95.7	88.4	13.4	33.7	45	1987	4.70	17.1	7		142
	303	35.6	7.45	10.13	7944	7960	97.2	97.4	3376	453	92.2	94.7	93.4	7.7	34.6	29	1618	2.91	17.0	0		0
	303	35.6	7.35	12.01	7839	7855	97.0	97.2	3371	446	90.8	93.4	103	7.9	40.0	23	1439	2.11	17.4	0		0
13			Abort																			
14	749	88.1	17.41	8.05	8421	8433	100.5	100.6	8165	469	94.9	94.3	96.4	60	60.7	104	1809	2.44	7.59	0		0
	750	88.3	17.82	9.95	8240	8250	99.6	99.7	8258	464	93.5	93.8	105	65	63.1	76	1593	1.60	7.57	8		40
	750	88.3	18.44	11.92	7954	7966	97.1	97.3	8234	446	89.9	92.4	115	71	66.2	59	1413	1.13	7.53	8		40
15	850	100	19.83	8.10	8392	8396	99.8	100.1	9416	475	95.9	95.8	122	81	69.6	136	1881	2.11	7.48	0		0
	847	100	20.23	10.41	8200	8203	99.1	99.2	9406	463	93.7	94.4	133	88	72.0	82	1597	1.35	7.47	25		40
	849	100	21.13	12.11	7879	7877	96.1	96.1	9372	441	88.7	92.2	147	96	76.2	64	1424	0.97	7.43	0		0

(U) The vacuum specific impulse (I_{vac}) and vacuum specific impulse efficiency (ηI_{vac}) are presented for tests made at chamber pressures above 300 psia where nozzle separation did not occur. The ηI_{vac} data were corrected for the measured heat loss to the chamber and nozzle extension.

(U) The sea level data presented in table IV were obtained in tests under Contract AF 04(611)-9965. These data will be compared with the altitude data in the following performance discussions. The c* and η_{c^*} values obtained in the sea level tests computed from chamber pressure measurements were reduced to account for the experimentally determined chamber throat discharge coefficient.

(U) The test data obtained in the tests are discussed in the following subparagraphs. Subparagraph 2 discusses the data obtained in the high chamber pressure tests. The low chamber pressure test data are discussed in subparagraph 3, and subparagraph 4 describes the throttling performance. Subparagraph 5 describes the performance corrections.

2. High Chamber Pressure Tests

a. General

(C) Seven tests were made at chamber pressures in the 300 to 850 psia range. In the tests, mixture ratio excursions covering the 8 to 12 range were accomplished while the chamber pressure was controlled to a constant value. Tests were made at each of the following chamber pressures: 300, 450, 600, 750 and 850 psia. The 180-to-1 expansion ratio nozzle extension was flowing full in these tests and consequently specific impulse as well as characteristic exhaust velocity performance data were obtained. In Section VI, it is shown that the nozzle pressure ratio was high enough in all tests to ensure that the nozzle was not separated.

(C) Combustion stability was obtained in all high-chamber pressure tests. Typical oscillograph traces for the 300 and 850 psia tests are shown in figures 7 and 8. The largest peak-to-peak chamber pressure fluctuation recorded was 4% of the nominal chamber pressure value and the frequency was low (40 to 172 cps). The oscillograph trace for the 600-psia chamber pressure test showing these slight fluctuations are presented in figure 9. In figures 7 through 9, the callouts denote the following:

P_c = Chamber pressure
CPIT = Oxidizer primary injector temperature
ONP = Oxidizer flow nozzle inlet pressure
ONDP = Oxidizer flow nozzle differential pressure
ONT = Oxidizer temperature at the flow nozzle
OSPDP = Oxidizer secondary injector plate differential pressure
FODP = Fuel flow orifice differential pressure
FOT = Fuel temperature at the flow orifice
FIDP = Fuel injector differential pressure
FOP = Fuel orifice inlet pressure

(C) The flow divider valve was prepositioned before each test to provide a predetermined flow split and to ensure low frequency stability. The flow divider valve positions used were selected based on the results of the previously completed sea level tests with the 8.5K injector. Figure 10 shows the flow splits that were used in the high chamber pressure tests.

(C) Table IV. 8.5K Injector Sea Level Test Results

Test No.	Chamber Pressure, psia	Thrust, %	Total Propellant Flow, lb/sec	Mixture Ratio	c* Face Tap, ft/sec	c* Chamber Tap, ft/sec	η_{c^*} Face Tap, %	η_{c^*} Chamber Tap, %	Vacuum Thrust, lb	I_{vac}, sec	$\eta_{I_{vac}}$, %	Ox Pri Inj ΔP, psi	Ox Sec Inj ΔP, psi	Ox Ave Inj Vel, ft/sec	Fuel Inj ΔP, psi	Fuel Inj Vel, ft/sec	Fuel Inj Vel, ft/sec	Momentum Ratio	Ox Flow Split, %	Peak-to-Peak ΔP_c, psi	P_c Frequency, cps
1									Abort												
2	301	35.4	7.49	7.9	7754	7506	93.0	90.0	2631	351	84.6	19.5	26.6	28.5	70.4	2243	2425	8.76	7.2	18.0	155
	309	36.4	7.51	7.8	7934	7684	95.2	92.3	2685	357	86.1	22.2	22.7	27.6	61.6	2259	2271	8.63	8.0	14.0	156
	312	36.7	7.50	7.9	8037	7805	96.5	93.8	2687	358	86.3	22.9	22.5	27.1	64.5	2224	2315	8.76	8.3	17.0	160
	312	36.7	7.51	7.9	8021	7767	96.5	93.4	2684	357	82.6	58.9	19.5	30.2	64.0	2244	2324	7.86	13.6	11.0	156
	316	37.2	7.51	7.9	8120	7788	97.7	94.9	2719	362	87.4	59.0	18.9	30.0	66.0	2213	2348	7.99	13.6	13.0	156
	317	37.3	7.51	7.9	8145	8027	97.9	96.5	2763	368	88.8	176.6	13.6	44.4	61.8	2250	2286	5.28	23.8	19.0	54
	319	37.6	7.49	8.0	8211	8032	98.7	97.4	2779	371	89.5	174.0	12.5	44.0	61.9	2229	2291	5.28	23.7	16.0	54
	314	37.0	7.50	8.0	8062	7950	97.0	95.7	2735	365	88.0	244.5	13.7	53.4	68.3	2263	2416	4.64	28.1	5.0	144
	316	37.2	7.49	8.0	8137	7942	97.9	95.6	2753	367	88.7	235.6	13.0	52.2	66.0	2248	2373	4.64	27.6	5.0	144
	318	37.4	7.51	7.9	8180	8058	98.4	97.0	2789	372	89.7	320.3	10.3	64.0	68.5	2237	2400	3.86	32.2	6.0	154
	318	37.4	7.51	7.9	8166	8050	98.2	96.9	2785	371	89.5	318.5	9.9	63.7	68.0	2242	2395	3.86	32.1	6.0	152
	317	37.3	7.50	8.0	8162	8072	98.2	97.2	2788	372	89.7	380.5	7.9	72.7	66.5	2229	2388	3.35	35.2	6.0	156
	317	37.3	7.50	8.0	8158	8069	98.1	97.1	2800	373	90.1	379.4	7.7	72.5	65.7	2216	2350	3.35	35.1	6.0	158
3	234	27.5	5.86	8.3	7693	7291	92.9	88.1	2071	352	85.3	101.7	21.7	34.0	54.9	2093	2397	6.96	22.4	9.0	122
	237	27.9	5.89	8.5	7746	7473	93.8	90.6	2108	358	86.7	97.8	19.6	32.8	49.7	2031	2334	6.83	22.2	8.0	120
	241	28.4	5.73	9.3	8048	7925	98.3	96.8	2164	374	91.2	138.2	5.5	39.5	34.7	1772	1940	4.25	26.8	12.0	84
	250	29.4	5.64	8.1	8108	7959	98.1	96.4	2223	374	90.7	233.4	5.2	56.3	44.1	2029	2107	3.74	34.6	14.0	52
	250	29.4	5.92	8.1	8143	8018	98.5	97.1	2217	375	90.8	230.6	4.1	55.9	44.6	2037	2125	3.74	34.5	15.0	52
4	52	6.1	1.51	15.2	8632	6586	85.1	84.5	694			53.8	9.5	41.9	7.2	1348	1865	2.32	59.3	1.0	20
5	34	4.0	0.90	6.9	7238	7192	87.6	87.0	546			15.7	2.3	23.0	12.0	2529	2916	14.94	60.0	1.0	152
6	33	3.9	0.83	6.3	7726	7842	93.3	94.7	554			37.5	2.2	56.0	10.9	2567	2812	6.44	80.0	0.5	400-500
7	28	3.3	0.66	4.8	8165	8164	97.3	97.3	499			137.3	0	45.4	12.3	2988	3203	11.85	100.0	0.5	400-500
8	119	14.0	3.02	12.5	7623	7390	95.1	92.2	1089			107.0	6.0	45.1	17.7	1451	1932	2.83	42.4	1.0	116
9	78	9.2	1.86	6.8	8110	7956	97.9	96.1	883			44.8	3.1	31.7	21.7	2370	2616	9.79	47.0	1.0	132
10	78	9.2	1.85	6.8	8079	7941	97.5	95.9	895			71.0	2.7	48.3	21.3	2386	2604	6.44	60.3	1.0	136
11	78	9.2	1.82	6.7	8253	8106	99.6	97.9	902			73.8	1.8	51.0	21.8	2374	2640	6.31	64.0	2.0	136
12	164	19.3	3.93	5.6	8062	7885	95.0	93.0	1442	367	87.4	131.8	4.3	47.7	54.7	2849	2833	8.63	29.5	1.5	120
13	174	20.5	3.98	5.2	3426	8284	99.0	97.3	1509	379	90.1	128.8	4.3	46.8	60.3	2894	2884	9.66	39.0	2.0	52
14	824	97.0	18.65	7.4	8518	8451	100.5	99.7	7184	385	91.7	115.7	79.7	69.5	116.1	2170	1896	2.96	7.4	0	0

CONFIDENTIAL

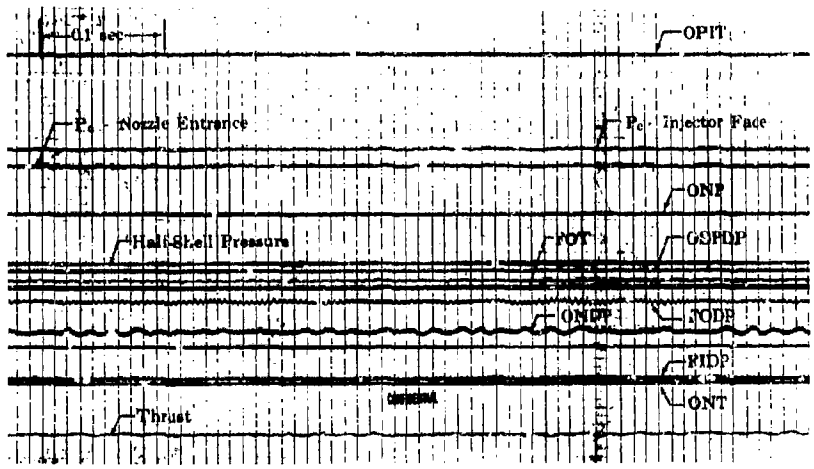

Figure 7. 8.5K Oscillograph for P_c = 300 psia; Mixture Ratio = 12 FD 20649A

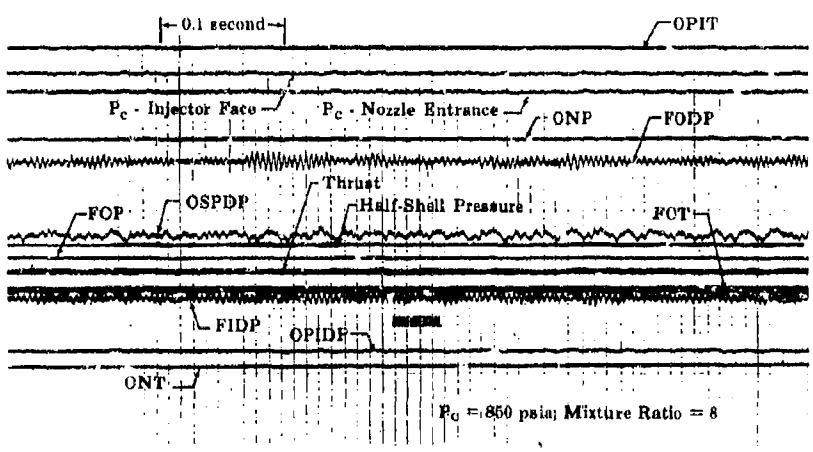

Figure 8. 8.5K Oscillograph for P_c = 850 psia; Mixture Ratio = 8 FD 20655A

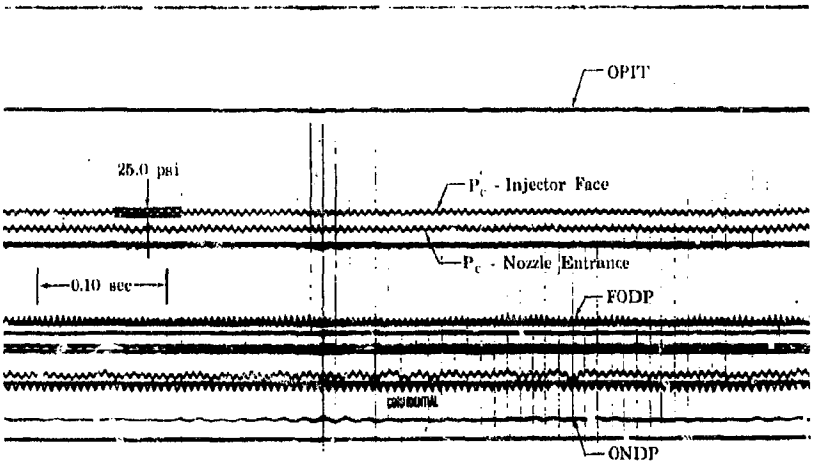

Figure 9. 8.5K Oscillograph for P_c = 600 psia; Mixture Ratio = 8.0 FD 20651A

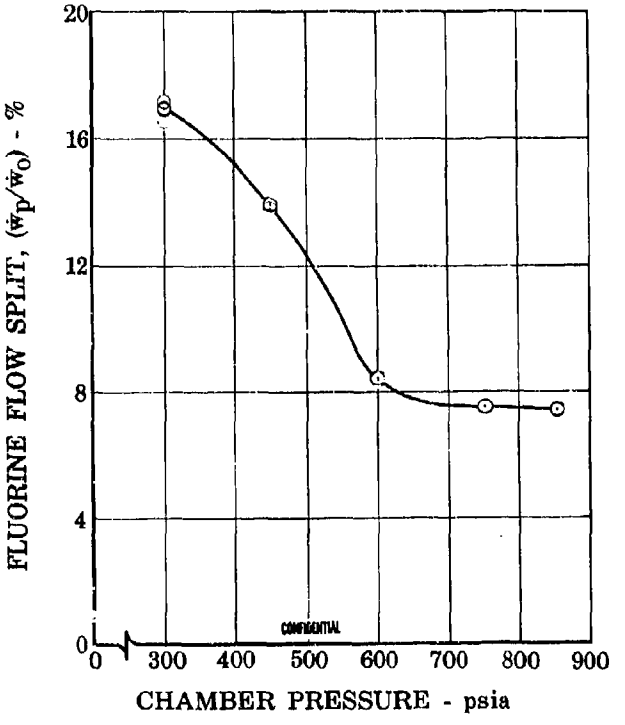

Figure 10. Flow Splits Used in High P_c Tests FD 20952

(C) Figures 11 through 15 present the test data obtained in the high pressure tests plotted as functions of mixture ratio. At the 300-, 750-, and 850-psia chamber pressure levels, specific impulse and nozzle performance data as well as c* data are presented. For 450 and 600 psia, only

c* performance data are given because, in tests at these chamber pressures, erroneously high thrust data were obtained. When this was discovered after the 600-psia test (test No. 11), extensive investigations of the thrust systems were made. Several small problems were solved, then repeated

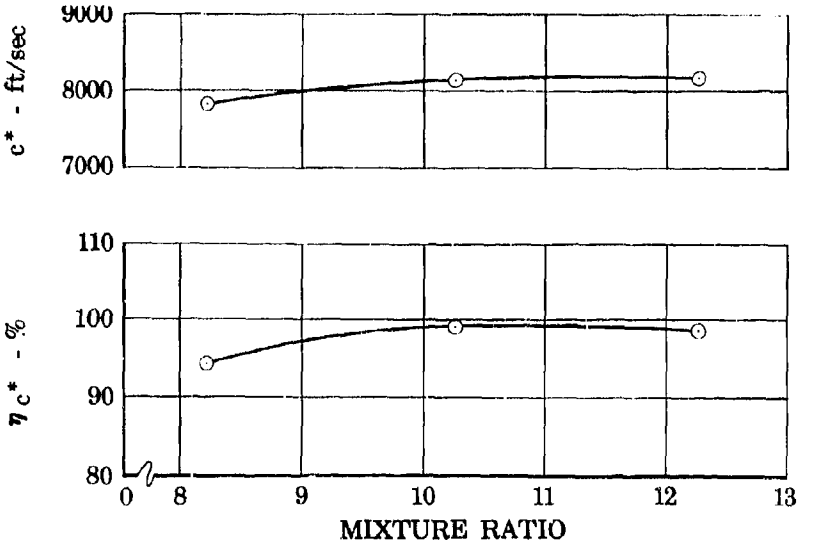

Figure 11. Performance - P_c = 450 psia FD 20936

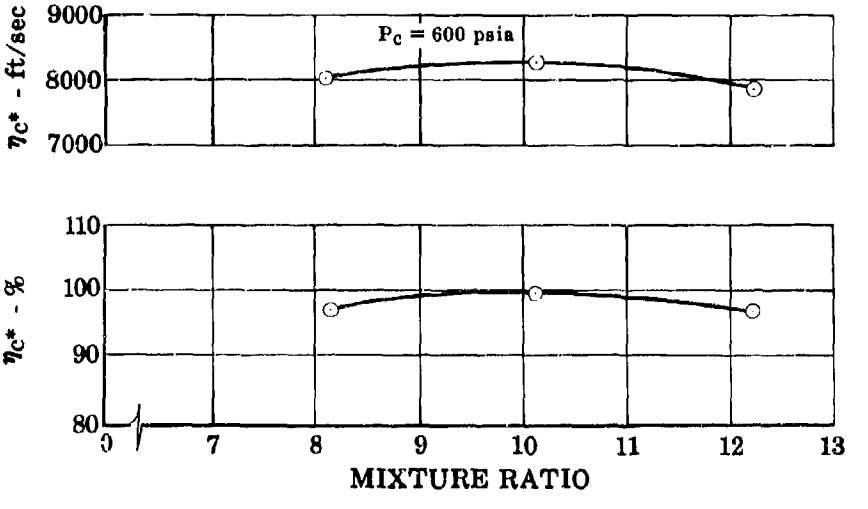

Figure 12. Performance - P_c = 600 psia FD 20991

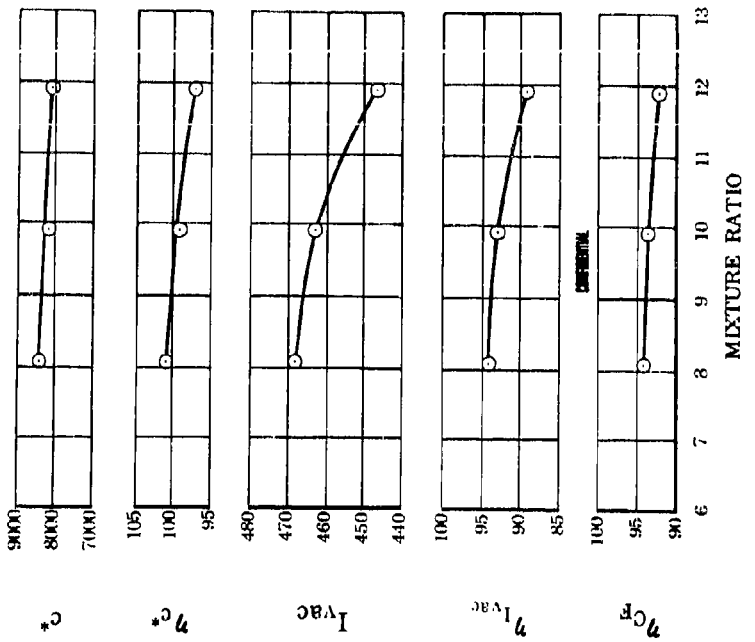

Figure 14. Performance - P_c = 750 psia FD 20939

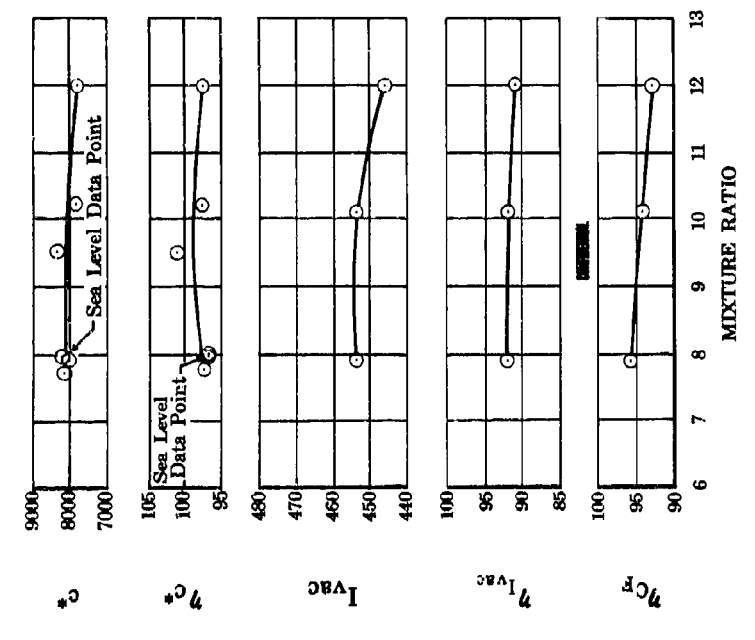

Figure 13. Performance - P_c = 300 psia FD 20941

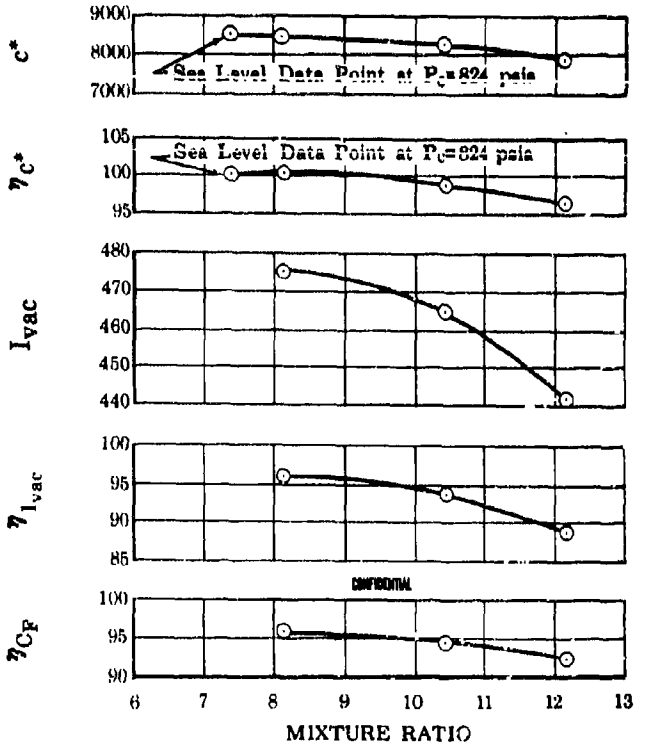

Figure 15. Performance - P_c = 850 psia FD 20940

calibration and checkout tests were accomplished to ensure that the thrust system was providing reliable and repeatable data. The thrust system repairs and calibration data are discussed in Appendix III.

(C) Extremely high performance was obtained in all tests. All c* efficiency data showed η_c* above 96% except for one data point (η_c* = 94.3% at r = 8 and P_c = 450 psia). Measured I_{vac} range was 441-475 sec; the upper limit (475 sec) is the highest ever recorded in chemical bipropellant rocket combustion tests (the range represents some of the highest I_{vac} data ever measured). The c* and I_{vac} data are discussed separately in the following paragraphs.

b. Characteristic Exhaust Velocity Performance

(C) Good agreement between the altitude and sea level c* data was obtained. The available sea level test data are included in figures 11 and 15 for the 300- and 850-psia chamber pressure tests. At 300 psia only the sea level data point obtained at the same flow split as that used in the altitude tests at 300 psia was plotted. The good agreement between the sea level and altitude test data indicates that increasing the faceplate permeability from 40 to 120 scfm did not adversely affect performance. When the more permeable faceplate was selected to increase the transpiration coolant flow through the faceplate (see Section V, paragraph B) a drop in c* performance was anticipated because the fuel-to-oxidizer injection

momentum ratio would decrease. This supposition was based on correlations of c* efficiency with injection momentum ratio that were obtained with the 1K F_2/H_2 dual orifice injector and in RL10 injector tests with F_2/H_2 propellants.

(C) The 8.5K injector c* performance data are plotted against injection momentum ratio in figure 16. Also included in this figure are the η_c*-momentum ratio curves obtained for the 1K dual-orifice injector and for the RL10 injector. At low momentum ratios the 8.5K injector provided consistently higher performance than either the 1K or RL10 injectors. This has important implications for the pump-fed F_2/H_2 engine being proposed for the Air Force Space Maneuvering Propulsion System applications. In these engines, which are being designed for approximately the same chamber pressure range as that evaluated in the 8.5K tests, it will be possible to obtain high c* performance using lower injection momentum ratios than previously believed. Thus the fuel injector pressure drop can be reduced to reduce fuel pump power requirements if turbine power restricts engine operation.

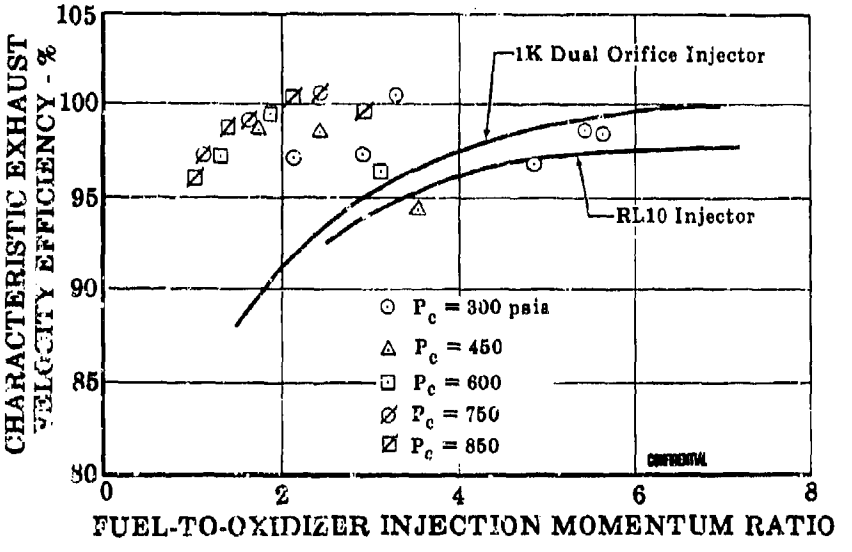

Figure 16. Characteristic Exhaust Velocity Efficiency vs Momentum Ratio ED 21501

(U) It should be noted in comparing the 8.5K injector to the 1K injector (table V) that the 8.5K injector has a 15-degree conical face, whereas the 1K injector has a flat face. A conical-face injector produces a large recirculation pattern that should enhance propellant mixing and improve performance over that obtained from a flat-face injector. Furthermore in contrast to the RL10 injector, the 8.5K injector (as well as the 1K injector) was tested with chambers with higher L* than that of the RL10 chamber (55 versus 30 inches). In addition (and probably most important) the secondary flow at injection has a radial velocity component with the dual-orifice injector (figure 17) that enhances mixing of the fluorine with the coaxial hydrogen stream and therefore increases performance.

(U) Table V. Injector Characteristics

	Face Shape	Chamber L*, in.	Fluorine Injection
8.5K Dual-Orifice Injector	15-deg Conical	55	Dual Orifice
1K Dual-Orifice Injector	Flat	55	Dual Orifice
RL10 Injector	15-deg Conical	30	Single Orifice

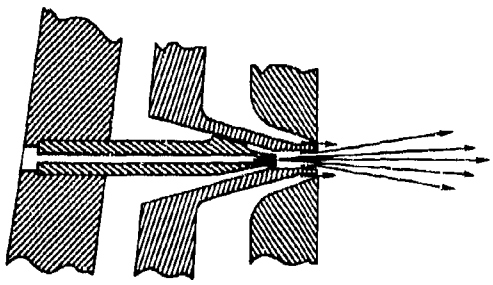

CONFIDENTIAL

Figure 17. Flow Pattern of Dual-Orifice Concentric Element FD 20951

(C) The variation of c* efficiency with momentum ratio appears to be a function of chamber pressure. Note in figure 16, for a chamber pressure range of 750 to 850 psia, that c* efficiency increases with increasing momentum ratio. This trend is therefore like the 1K and RL10 injector performance curves, however the curve is further to the left. That is, at the 750- to 850-psia chamber pressure levels, the 8.5K injector provided the same level of performance as that provided with the 1K and RL10 injector but at a much lower momentum ratio. (For example, the 8.5K injector provided a c* efficiency of 97.5% at a momentum ratio of 1.25, whereas in the 1K and RL10 injectors the required momentum ratios for this performance level were between 4 and 5.)

(U) There are several factors associated with the increased chamber pressures that could contribute to higher performance. First, as the chamber pressure is increased the densities of the injected hydrogen gas and the reacted propellant gases, as well as the combustion temperature, increase. All of these effects increase the chemical reaction rate. In addition, propellant mixing should improve as chamber pressure increases because the chamber Reynolds number and the total injector momentum increase linearly with propellant flow and therefore chamber pressure.

(C) At 600 and 450 psia chamber pressures, the c* efficiencies are also higher than the 1K curve at momentum ratios below 2.3. Above this value performance drops. The curve peaks at a momentum ratio of approximately 2. This performance trend results because c* efficiency, at these two chamber pressures, was higher at r = 10 than at r = 8.

(C) Although there is more data scatter, the c* performance curve also apparently peaks for 300 psia chamber pressure (like the 450-600 psia data); however, in this case the peak occurs at a momentum ratio of approximately 3.5 The apparent peaks in the c* efficiency versus momentum ratio curves for 300, 450, and 600 psia appear to occur because at these chamber pressures the c* efficiencies are higher at r = 10 than at r = 8. Although this may be true it does not agree with the data trend obtained at 750 and 850 psia chamber pressures and the 1K and RL10 data. It is possible that the data obtained at r = 8 in these tests are erroneously low. These were the first data points taken in the respective tests and consequently if thermal equilibrium had not been achieved in the fluorine supply line between the flow nozzle and the injector (and thus if the fluorine temperature was still decreasing when the r = 8 data were taken) the measured fluorine flow through the flow nozzle would be higher than the fluorine flow being injected into the chamber, this causing the performance data (specific impulse data as well as c* data) to be erroneously low. In subparagraph 5c this supply line storage effect is discussed in more detail, and it is shown that the mixture ratio of 8 data could be as much as 2.3% too low at chamber pressure of 300 psia.

(C) In the 450 psia test, the magnetic tape of the digital recording system broke 7 seconds after the start of the test and thus it was necessary to compute data from the oscillograph traces. Because of this, the accuracy of the data at 450 psia is not as good as that at the other chamber pressures. To evaluate the accuracy of the 450 psia data, the test data obtained in test No. 9, (the first 300 psia chamber pressure test) was also computed from oscillograph data and compared with the data computed by the digital system (table VI).

(C) Table VI. Performance Data for Test No. 9

Scan Time, sec	Digital-Computed Data P_c, psia	r	c*, ft/sec	Oscillograph-Computed Data P_c, psia	r	c*, ft/sec	Difference in c*, %
319	303	7.73	8081	298	7.97	7950	-1.6
328	303	9.64	8250	303	9.99	7950	-3.7

From this comparison, it appears that the oscillograph-based data could be erroneously low.

(C) Based on the foregoing considerations, it is believed that the c* and I_{vac} data obtained at r = 8 in the 300-, 450-, and 600-psia chamber pressure tests are actually too low. If these data could be corrected, the peaked curves of c* efficiency versus momentum ratio would change to reflect an increasing c* with increasing momentum ratio, which is the trend obtained at 750 and 850 psia chamber pressure with the 8.5K injector and in previous 1K dual orifice and RL10 injector tests.

(C) In summary, the 8.5K injector has demonstrated extremely high performance capabilities. Based on the test data obtained and the foregoing discussion of potential performance errors, the 8.5K injector can provide nearly 100% c* efficiency at mixture ratios of 8 and 10; c* efficiency will decrease to approximately 97% at a mixture ratio of 12.

c. Specific Impulse Performance

(C) The specific impulse performance data obtained in the tests are the first data reported for F_2/H_2 propellants at chamber pressures up to 850 psia. The data are therefore very valuable in assessing the performance potential of the F_2/H_2 propellants. The specific impulse data obtained in the 300, 750, and 850 psia tests are presented in figures 11, 14, and 15. Note from these figures that the specific impulse, I_{vac}, specific impulse efficiency, $\eta_{I_{vac}}$, and the thrust coefficient efficiency, η_{CF}, all decrease with increasing mixture ratio. Some of the drop-off in the specific impulse and the specific impulse efficiency is caused by variations in c* efficiency, which also generally decreased with increasing mixture ratio. However, since the thrust coefficient efficiency (η_{CF}) is computed by dividing the specific impulse efficiency by c* efficiency a drop-off in η_{CF} indicates that expansion efficiency is also decreasing with increasing mixture ratio.

(C) The aerodynamic nozzle efficiency, which accounts for the losses due to friction and divergence, is approximately constant over the 300- to 850-psia chamber pressure range and the 8-to-12 mixture ratio range, as can be seen in table VII. These aerodynamic nozzle efficiences (C_s), were computed by the P&WA-developed methods described in Reference 2 and are approximately constant. For $r = 8$ and $r = 10$ the C_s can be rounded off to three digits to be equal to 96.5%. For $r = 12$ and $r = 14$ the three-digit value would be 96.6%. Figure 18 compares the thrust coefficient efficiency with the nozzle aerodynamic efficiency. The thrust coefficient efficiency is lower than C_s; the difference is due at least in part to chemical recombination or kinetic losses.

(C) The kinetic performance of the 8.5K test engine has been computed using the Bray sudden freezing analysis (Reference 3), modified by United Aircraft Corporation Research Laboratories. The results of these calculations are shown in figure 19. The kinetic performance data presented in this figure are for complete combustion (i.e., 100% c* efficiency). These values are also calculated for no heat loss to the chamber. When the values are adjusted for measured c* efficiency and heat loss they compare as shown in figures 20 through 22 with the measured specific impulse values. At 750- and 850-psia chamber pressures, there is good agreement between the measured and the calculated performance values. At 300 psia the calculated performance is lower than measured performance by about 3%. This could indicate that either the calculated values are too conservative or that the measured performance and therefore thrust is too high in this test. Since the thrust system error is estimated at ± 100 lb the thrust could be in error by this amount since the thrust is only approximately 3300 lb_f at 300 psia chamber pressure.

(C) Table VII. Nozzle Aerodynamic Efficiency

P_c, psia	r	C_s
15	8	0.96522
	10	0.96632
	12	0.96686
	14	0.96715
60	8	0.96551
	10	0.96635
	12	0.96632
	14	0.96672
150	8	0.96492
	10	0.96559
	12	0.96601
	14	
300	8	0.96499
	10	0.96535
	12	0.96582
	14	0.96621
750	8	0.96463
	10	0.96521
	12	0.96553
	14	0.96581

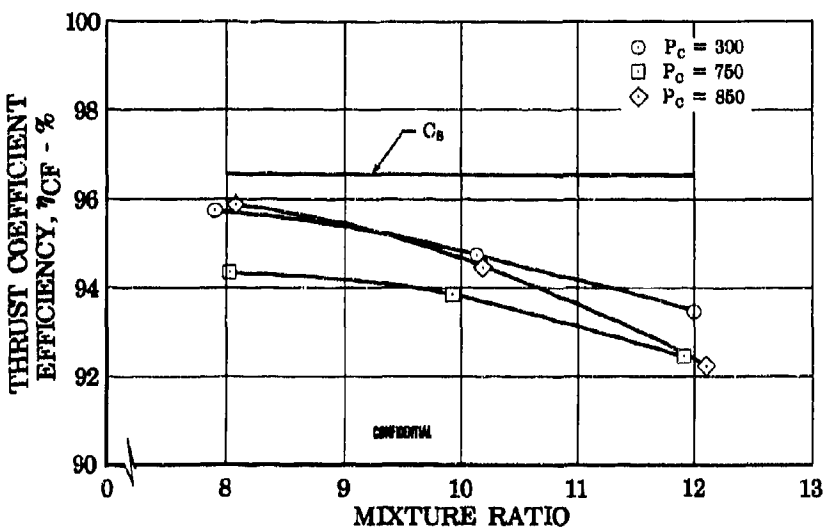

Figure 18. Comparison of η_{C_F} and C_s FD 20943

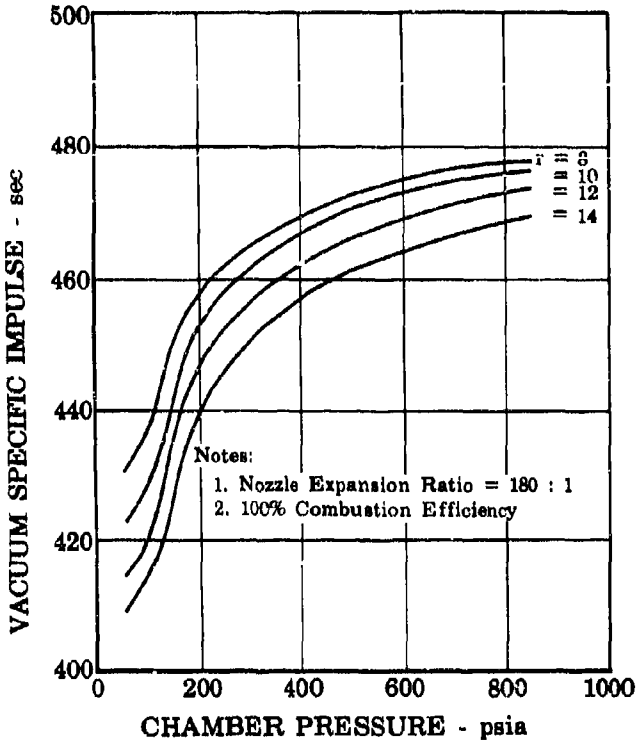

Figure 19. Calculated Kinetic Performance for 8.5K Injector FD 20948

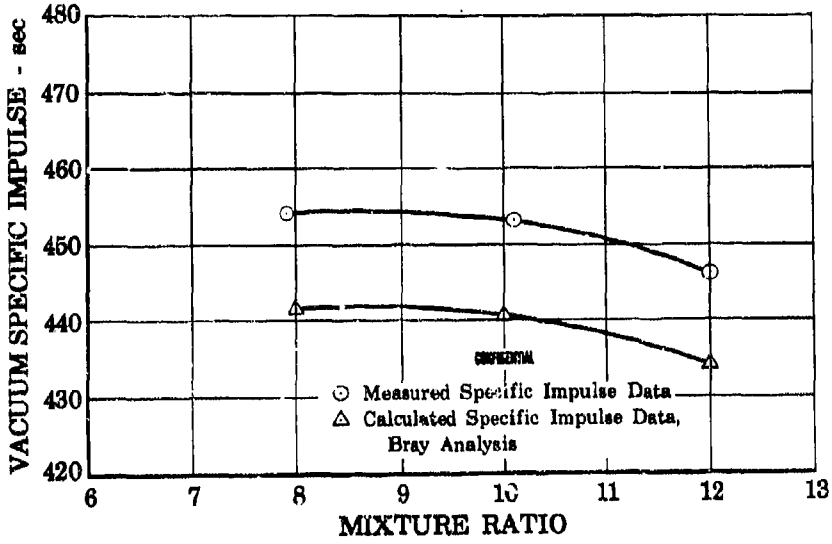

Figure 20. Comparison of Measured and Calculated I_{vac} Performance - P_c = 300 psia FD 20946

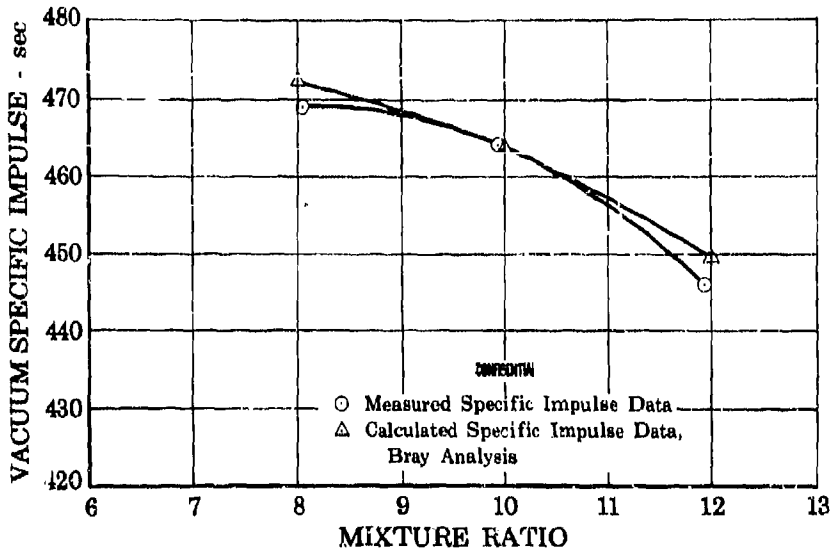

Figure 21. Comparison of Measured and Calculated I_{vac} Performance - P_c = 750 psia FD 20947

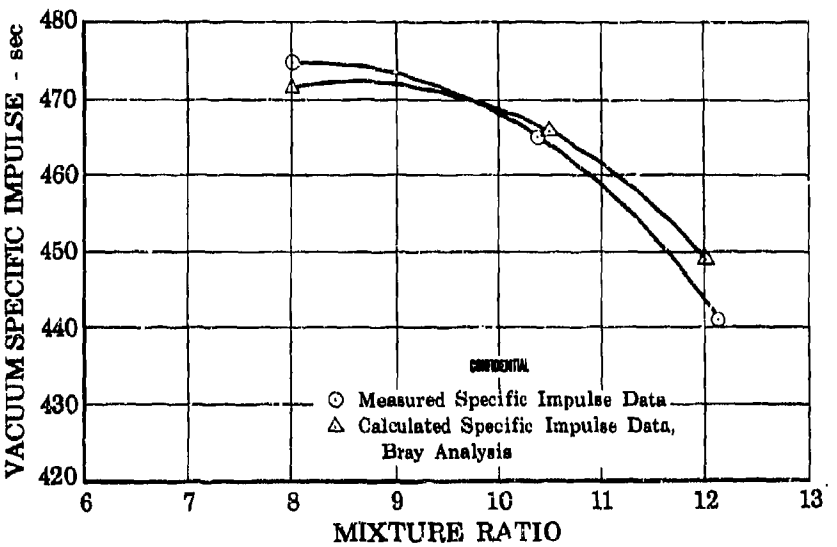

Figure 22. Comparison of Measured and Calculated I_{vac} Performance - P_c = 850 psia FD 20945

(C) Figures 23 through 25 illustrate the magnitude of the various losses for the three chamber pressure levels. By comparing the data in these figures, note that the measured kinetic losses were generally lower at 300 psia than at 750 psia and 850 psia. Since this is not in agreement with theory, the supposition that the thrust measurements in the 300-psia chamber pressure tests are too high is therefore supported. The kinetic losses are tabulated in table VIII along with all of the other performance parameters that were used in computing the data for figures 23 through 25.

(C) Table VIII. Performance Parameters

P_c, psia	r	$(I'_{vac})_{uc}$, sec	I'_{vac}, sec	η_c*, %	C_s, %	$\eta_c * I'_{vac}$, sec	$C_s \eta_c * I'_{vac}$	$\frac{I'_{vac}}{(I'_{vac})_{uc}}$	$\eta_K (I'_{vac})_{uc}$, sec	$\eta_K I'_{vac}$, sec	$\eta_K C_s \eta_c * I'_{vac}$, sec	I_{vac}, sec	I_{KL}, sec
303	7.92	500.7	489.7	96.8	96.5	474.0	457.4	0.9780	466.5	456.2	441.6	454	3.4
303	10.13	502.2	491.1	97.4	96.5	478.3	461.6	0.9779	462.5	452.3	440.5	453	8.6
303	12.01	502.4	490.9	97.2	96.6	477.2	461.0	0.9771	457	446.5	434.0	446	15
749	8.05	501.5	494.2	100.6	6.5	497.2	479.8	0.9854	476.5	469.5	472.3	469	10.8
750	9.95	503.1	495.8	99.7	96.5	494.3	477.0	0.9855	472.1	465.3	463.9	464	13
750	11.92	503.9	496.7	97.3	96.6	483.3	466.9	0.9857	468.7	462.0	449.5	446	20.9
850	8.10	501.6	494.9	100.1	96.5	495.4	478.1	0.9866	477.2	470.6	471.3	475	3.1
847	10.41	503.3	496.4	99.2	96.5	492.4	475.2	0.9863	475.9	469.4	465.6	465	10.2
849	12.11	503.9	497.1	96.1	96.6	477.7	461.5	0.9865	473.2	466.8	448.6	441	20.5

P_c = chamber pressure

r = mixture ratio

$(I'_{vac})_{uc}$ = theoretical vacuum specific impulse uncorrected for heat loss

I'_{vac} = theoretical vacuum specific impulse corrected for heat loss

$\eta_K (I'_{vac})_{uc}$ = calculated kinetic performance

I_{vac} = measured specific impulse

I_{KL} = kinetic loss

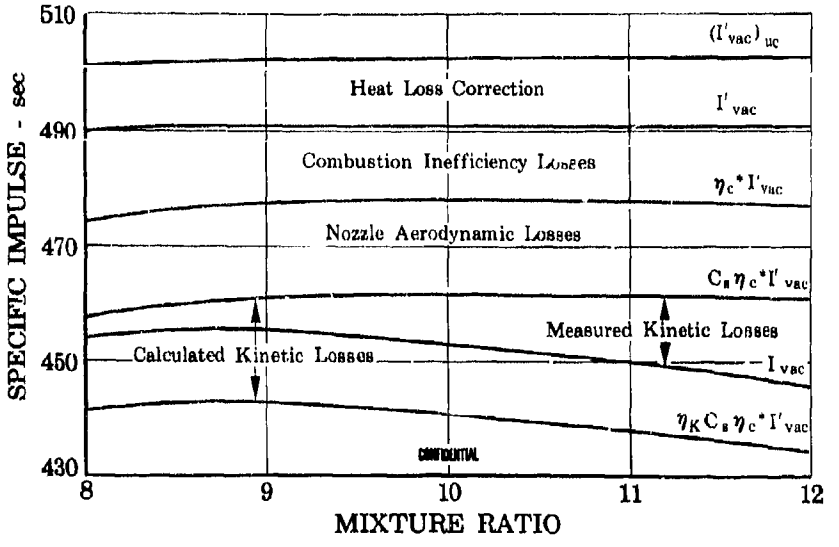

Figure 23. Specific Impulse Losses - P_c = 300 psia FD 20972

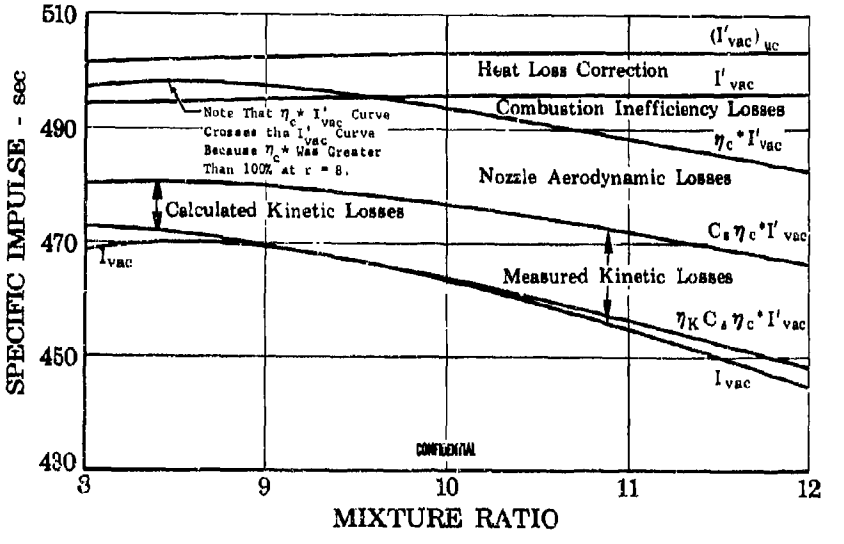

Figure 24. Specific Impulse Losses - P_c = 750 psia FD 20971

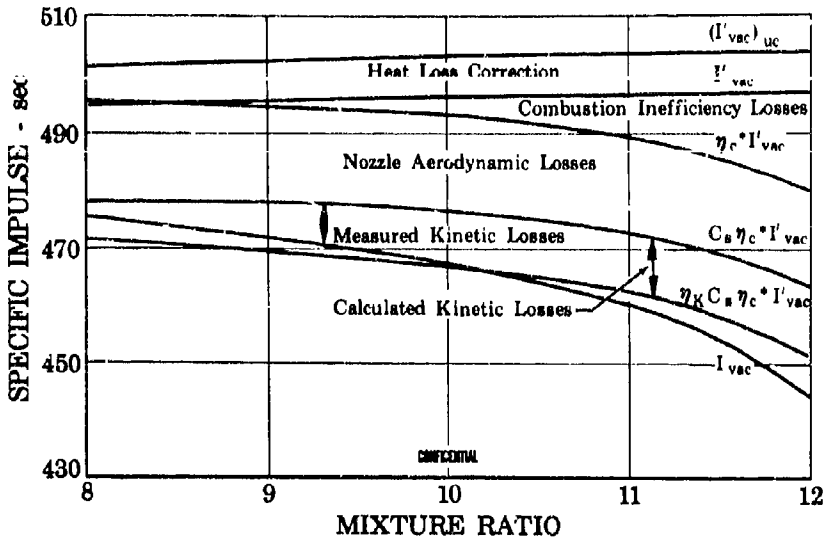

Figure 25. Specific Impulse Losses - P_c = 850 psia FD 20970

3. Low Chamber Pressure Performance

a. General

(C) The low chamber pressure tests evaluated combustion performance at chamber pressures of 30, 25, 20, 15, 10, and 5 psia. During these tests, a total test time of 827 seconds was accumulated. In the low chamber pressure tests flow split and mixture ratio excursions were made. With the exception of the 30 psia test, flow splits (the ratio of primary-to-total fluorine flow) of 50, 75, and 100% were evaluated at mixture ratios of 6, 8, 10, and 12. During the 30 psia chamber pressure test, a flow split excursion of 50, 75 and 100% was made at a mixture ratio of 14. The combustion stability and performance obtained during the tests are discussed below.

b. Combustion Stability

(C) No high frequency instability was noted. The only instability noted was of extremely low frequency (2.5 cps maximum) and in almost all cases had no definite frequency pattern. Figures 26 through 28 show typical chamber pressure vs time traces that were traced directly from the test oscillographs for chamber pressures of 25, 15, and 5 psia. As can be seen from the traces, the oscillations are mostly of a random nature. An examination of the data reveals that the amplitude and frequency of the chamber pressure oscillations were unaffected by mixture ratio, whereas the chamber pressure level and oxidizer primary-to-total flow split had a decided effect. Figure 29 shows chamber pressure fluctuations (the peak-to-peak amplitude of the pressure oscillations as a percentage of the operating chamber pressure) plotted against the operating chamber pressure. The flow splits of 50, 75, and 100% are indicated by different symbols.

(C) As shown in figure 29, the chamber pressure fluctuations increase as the chamber pressure decreases. At a chamber pressure of 30 psia the maximum and minimum fluctuations encountered were only 3.3% and 1.0%, whereas at 5 psia they were 36.2 and 13.9%. It should be noted that even though the peak-to-peak percentage amplitude is high, the amplitude expressed in pressure units is low because the chamber pressure is low. At a given chamber pressure and at flow splits of 50 and 75%, the magnitudes of the chamber pressure fluctuations are, for all practical purposes, the same. At a flow split of 100% a noticeable effect is seen in the fluctuations. At all but the 5 psia chamber pressure level the fluctuations are much lower than those at 50 and 75%. At 5 psia this tendency is completely reversed and a 100% flow split yields the highest fluctuations. At chamber pressures down to 5 psia, chamber pressure fluctuations of less than 10% were obtained with a 100% flow split. At 5 psia chamber pressure the fluctuations increased to the 30% level. These large fluctuations are probably due to fluorine vaporization in the primary injector as discussed in the following paragraphs.

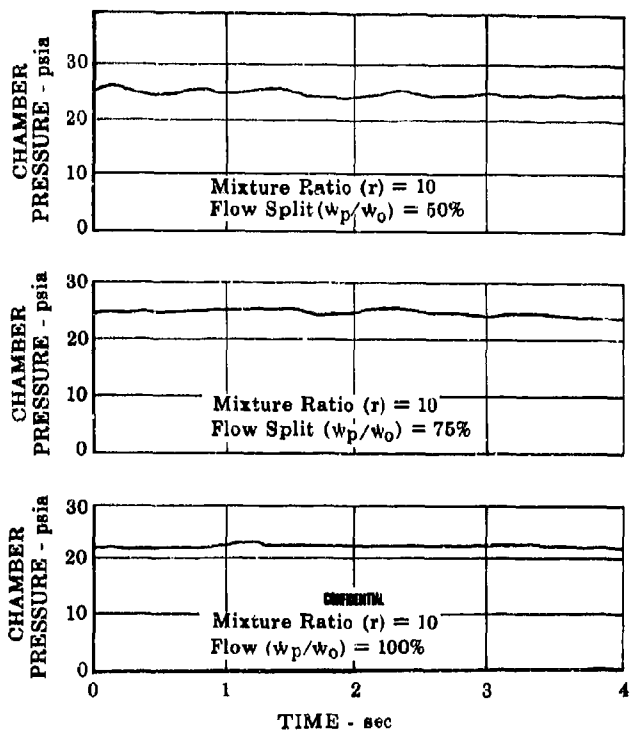

Figure 26. Chamber Pressure vs Time - Test No. 2, FD 20652A
P_c = 25 psia

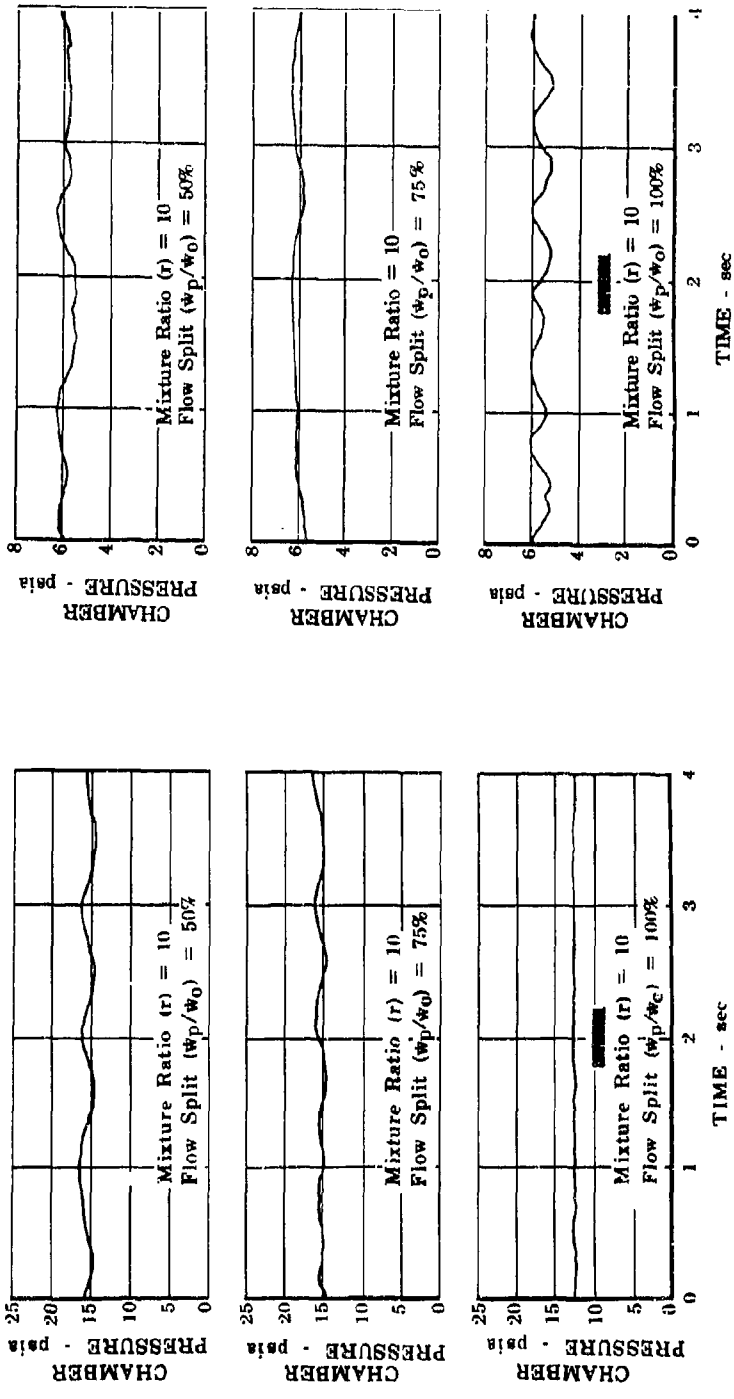

Figure 27. Chamber Pressure vs Time - FD 20654A
Test No. 4, P_c = 15 psia

Figure 28. Chamber Pressure vs Time - FD 20653A
Test No. 6, P_c = 5 psia

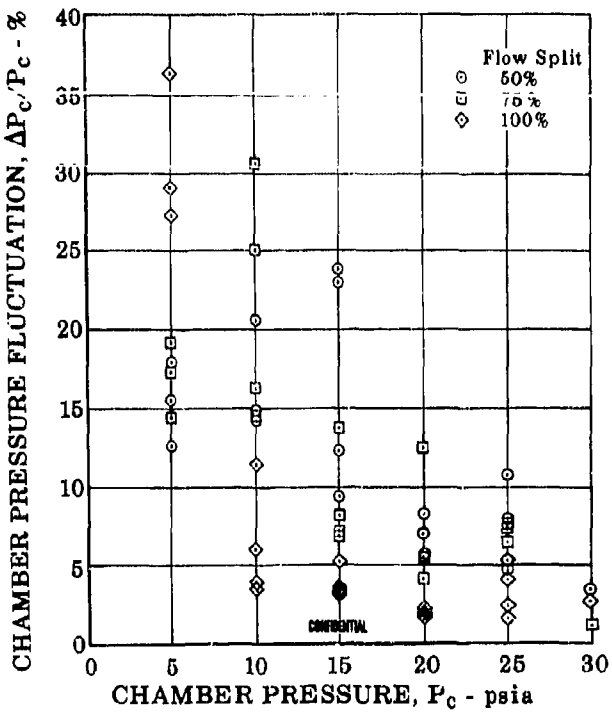

Figure 29. Chamber Pressure Fluctuations vs Chamber Pressure at Various Flow Splits FD 20989

(U) The chamber pressure oscillations and the chamber pressure fluctuations as described above are attributed to one or more of the following: (1) fluorine vaporization in the injector manifolds, (2) large injector and feed line volumes in combination with the low propellant flow rates, and (3) control valve movement coupled with the low propellant flow rates. These are discussed further in the following paragraphs.

(C) First, with the low chamber pressures and associated low injector pressure drops (especially across the secondary) vaporization occurs in the injector manifolds. An examination of the manifold pressures and the manifold temperatures (approximately 170°R in all tests) showed that in all cases the secondary manifold pressure was below the fluorine vapor pressure (see figure 30) and in some cases the primary manifold pressure was below the vapor pressure. The primary manifold pressure is above the fluorine vapor pressure at a flow split of 100% for all but the 5 psia chamber pressure test and even at this pressure level it is above the vapor pressure at all but the 10 and 12 mixture ratio points. At a flow split of 75%, vaporization occurs in the primary at chamber pressures of 20 psia and below and at 50% flow split at 25 psia and below. With vaporization, two-phase flow exists. If the vapor were equally dispersed in very small bubbles the only effect would be to decrease the overall fluid density thereby increasing the injection velocity. This increased velocity would improve the performance by improving the propellant mixing and improve stability by increasing injector pressure drops. On the other hand, if the bubbles

were to conglomerate into large bubbles, nonuniformly dispersed injection slugging would occur as these bubbles were injected. This type instability was noted during the tests where vaporization did occur.

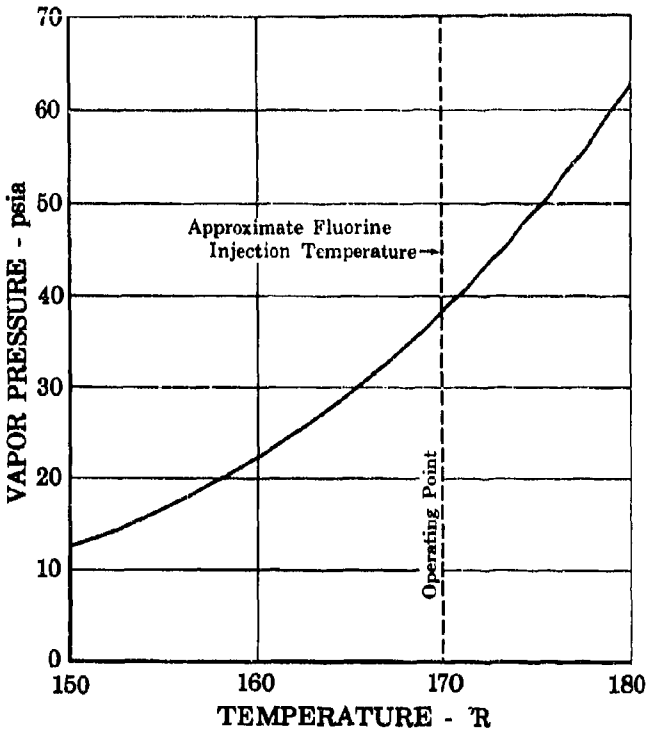

Figure 30. Fluorine Vapor Pressure FD 20961

(U) Secondly, the design of the injector manifolds and the propellant feed lines immediately adjacent to the injector were sized for the high flow rates at the maximum chamber pressure (850 psia). As a result, the large manifold and system volumes together with the low flow rates at low chamber pressures could contribute to system instabilities, especially at flow splits of less than 100% where some flow is being injected through the large-volume secondary injector.

(U) Finally, at the low flow rates any movements (regardless of how small) of the control valves could have a measurable effect on flow and chamber pressure. Therefore if the control valve system electrical gain and reset are not precisely set and thus valve position oscillations are caused, flow and chamber pressure will also oscillate. In the tests, no valve oscillations were noted; however, the tests were recorded on an oscillograph and slight movements enough to affect flow oscillations could have occurred without being detected.

(U) Of the foregoing factors that could affect stability, it is believed that vaporization was the major contributor to any random chamber pressure instability, whereas cyclic instability is attributed to valve oscillations.

(C) Figures 31 and 32 show the oscillograph trace for 25 psia (100% flow split) and 5 psia (50% flow split) chamber pressure levels. Also shown in the figures are the other system parameters.

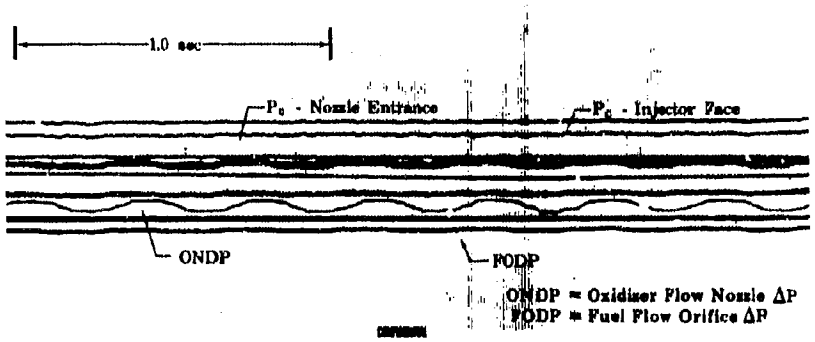

Figure 31. 8.5K Oscillograph Trace for P_c = 25 psia, r = 12, and $\dot{w}_p/\dot{w}_o$ = 100%

FD 20648A

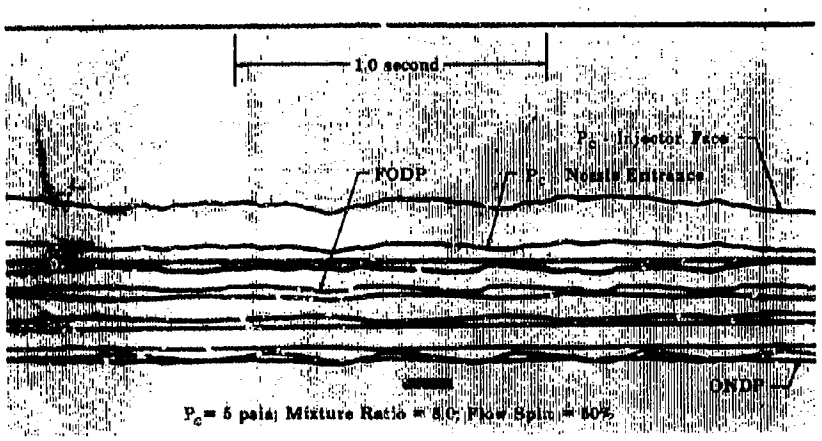

Figure 32. 8.5K Oscillograph Trace for P_c = 5 psia, r = 8, and $\dot{w}_p/\dot{w}_o$ = 50%

FD 20650A

c. Performance

(C) The c* performance data obtained in the low chamber pressure tests are plotted in figures 33 through 38. The individual figures present characteristic exhaust velocity (c*) and characteristic exhaust velocity efficiency (η_c*) plotted at given chamber pressures as functions of flow split at the various mixture ratios. The c* data were computed from chamber-tap chamber pressure measurements. The oxidizer primary-to-total flow split and momentum ratio referred to in this section were calculated for liquid fluorine flow through both the primary and secondary injectors. As discussed earlier, vaporization does occur; however, the flow splits based on liquid flow will be used for comparison purposes. The c* performance is a definite function of both mixture ratio and flow split. The effect of these parameters on performance is discussed in subsequent paragraphs.

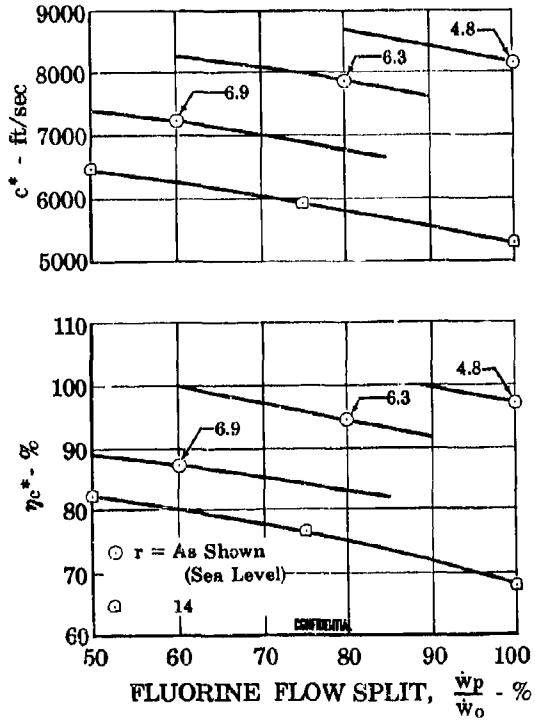

Figure 33. c* and η_c* Performance vs Flow Split at a Chamber Pressure of 30 psia

FD 20994

(C) Of the data obtained in the low chamber pressure tests, only three points have definitely been proved erroneous and therefore omitted from the data comparisons. All three of these data points were taken in test No. 8 at a chamber pressure of 5 psia and a mixture ratio of 6. The data points were the initial points taken during the test. During this data-taking period, large fluctuations in oxidizer flow rate (75% peak-to-peak amplitude) occurred and consequently the data are not considered valid.

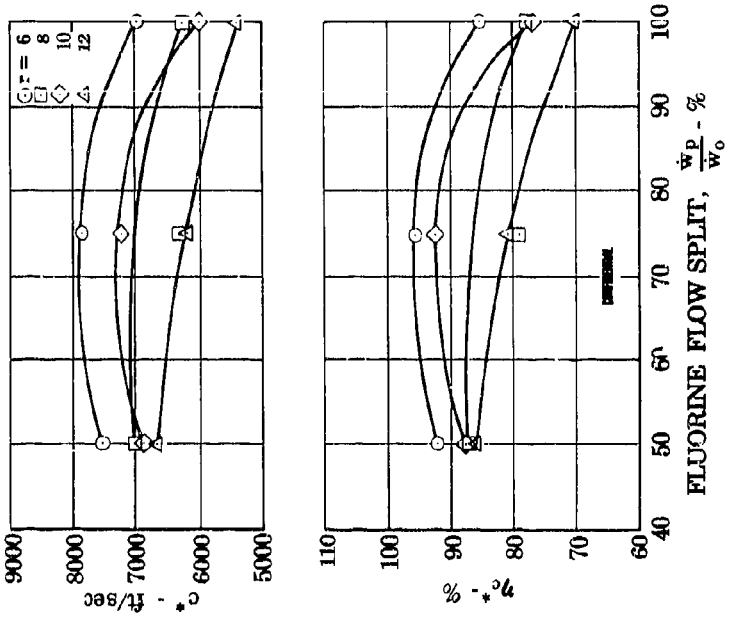

Figure 35. c* and ηc* Performance vs Flow Split at a Chamber Pressure of 20 psia FD 20937

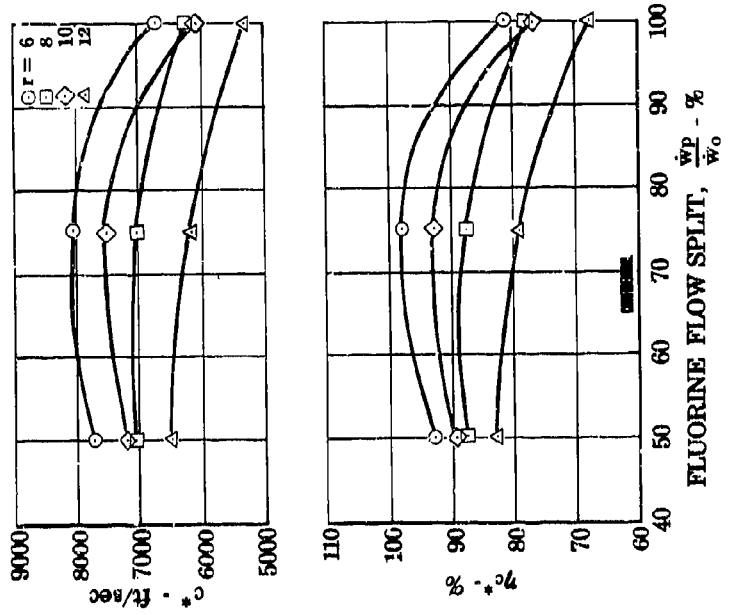

Figure 34. c* and ηc* Performance vs Flow Split at a Chamber Pressure of 25 psia FD 20996

CONFIDENTIAL

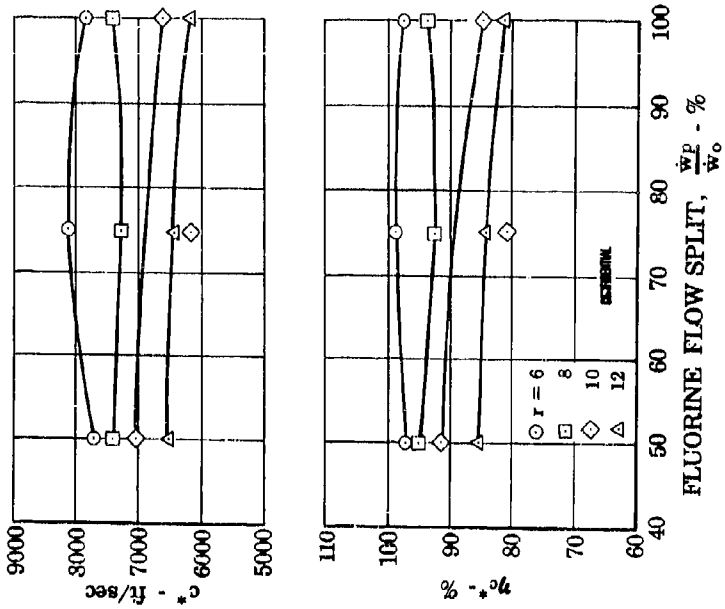

Figure 36. c^* and ηc^* Performance vs Flow Split at a Chamber Pressure of 15 psia FD 20986

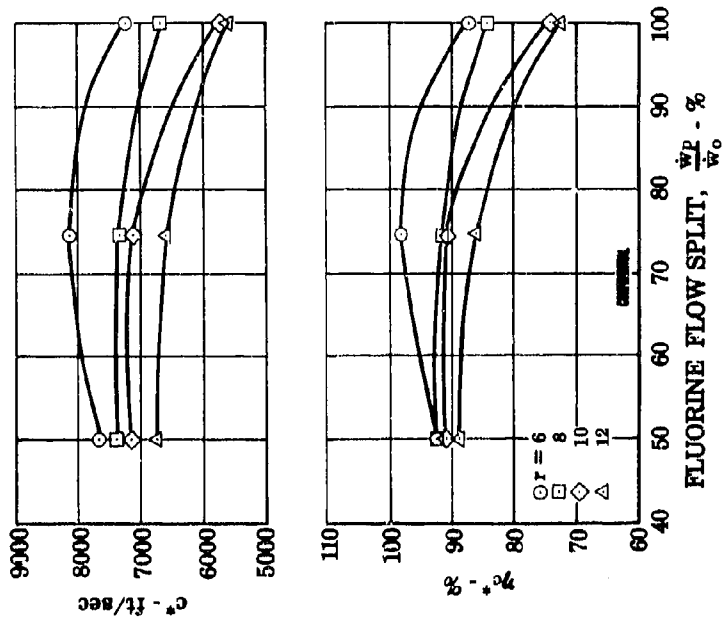

Figure 37. c^* and ηc^* Performance vs Flow Split at a Chamber Pressure of 10 psia FD 20932

CONFIDENTIAL

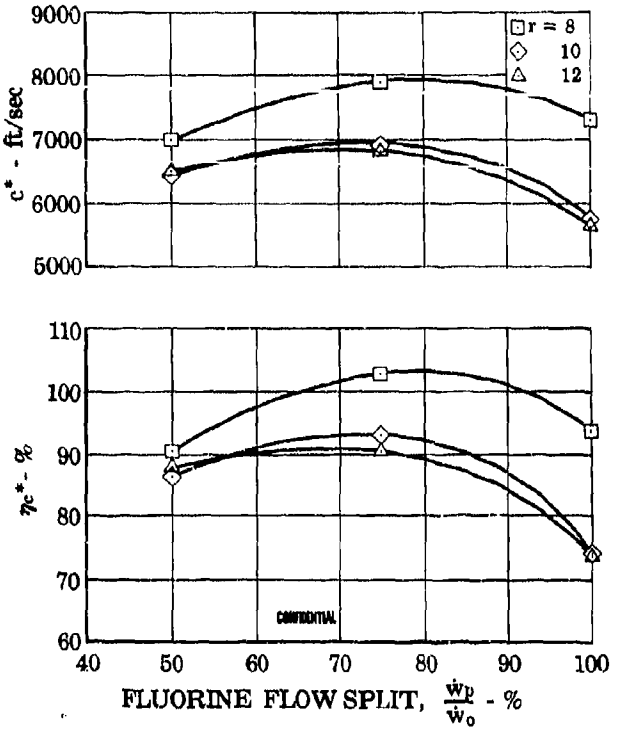

Figure 38. c^* and η_{c^*} Performance vs Flow Split at a Chamber Pressure of 5 psia

FD 20931

The flow fluctuations are attributed to the fact that the injector was still being cooled down and the fluorine was boiling in the injector, causing fluctuations in flow. Unstable fluorine flow was observed in several of the tests during the start transient; however, the flow stabilized after a short period. In this test the flow was so low that a long time was required to cool down the injector. In the remainder of test No. 8, the flow was fairly stable with a peak-to-peak flow variation of less than 25%. Two other data points failed to follow the data trends. These points were obtained at 75% flow split, at chamber pressures of 10 and 20 psia and at mixture ratios of 10 and 8, respectively. Inadequate time was allowed at these conditions to obtain valid steady-state data.

(C) Figures 33 through 38 illustrate the importance of the fluorine flow split at the low chamber pressures. The flow split directly varies the injector fuel-to-oxidizer injection momentum ratio and hence, the propellant mixing. Note from these figures that for each mixture ratio and chamber pressure, an optimum flow split exists at which the performance will be highest. Figure 39 summarizes the optimum flow splits. The figure shows the optimum flow splits at which the highest performance would be obtained plotted as a function of chamber pressure at the various mixture ratios. The figure shows that with a decreasing mixture ratio and decreasing chamber pressure the optimum flow split increases. The increasing optimum

flow split with decreasing mixture ratio leads one to believe that for each chamber pressure an optimum momentum ratio might exist that would give the best propellant mixing.

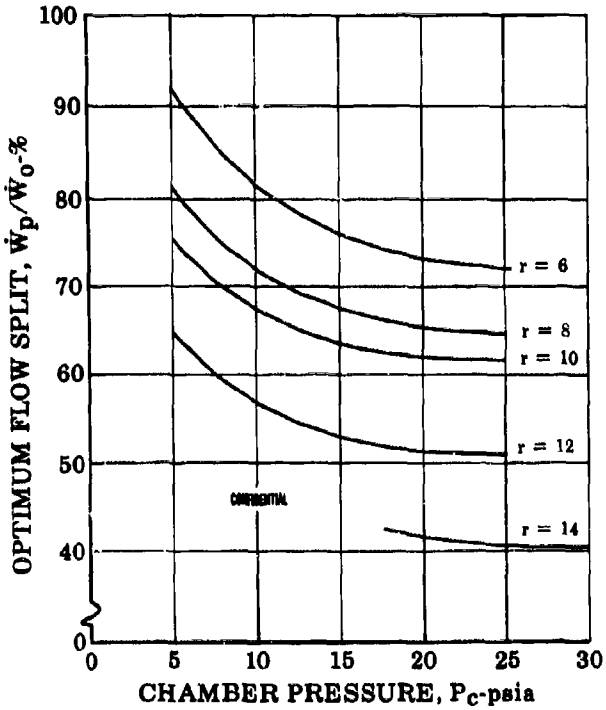

Figure 39. Oxidizer Optimum Flow Split FD 20953

(U) Table IX shows the momentum ratio determined from the test data for the optimum flow splits of figure 39. Note from table IX that a fair agreement exists in the momentum ratios for a given chamber pressure.

(C) Table IX. Momentum Ratios for Optimum Flow Splits

P_c, psia	r	Flow Split, %	MR
30	14	40.0	3.1
25	6	72.0	5.0
	8	64.5	4.0
	10	61.5	5.5
	12	51.0	5.5
20	6	73.0	8.4
	8	65.0	5.9
	10	62.0	7.2
	12	51.0	7.4
15	6	76.0	4.3
	8	67.0	4.6
	10	63.5	4.2
	12	53.0	3.7
10	6	81.5	2.2
	8	72.0	1.5
	10	67.5	1.8
	12	57.0	1.5
5	8	81.0	0.7
	10	75.5	0.9
	12	64.5	0.7

(C) By averaging the momentum ratios at each chamber pressure, an optimum momentum ratio for that chamber pressure was determined. Figure 40 shows this optimum momentum ratio as a function of chamber pressure. The peak in the curve is associated with fluorine vaporization. At chamber pressures below 20 psia vaporization is very prevalent. The data trends described previously now become clear. At a certain chamber pressure as mixture ratio decreases, and thus the fuel flow and fuel velocity increase, a higher oxidizer velocity is required to maintain the optimum momentum ratio, thus requiring an increase in flow split.

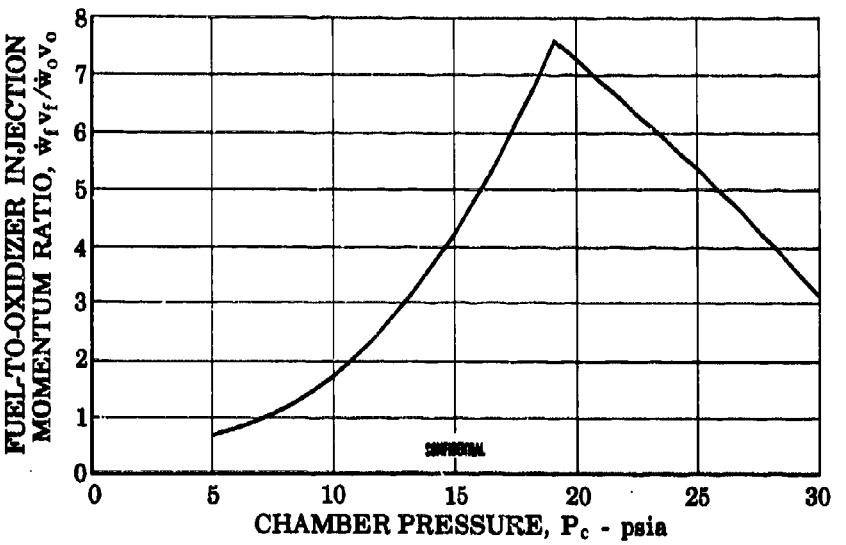

Figure 40. Optimum Momentum Ratio FD 20933

(C) Figure 41 shows the maximum c* performance obtained during the tests. In this figure, c* and η_{c^*} are plotted as functions of chamber pressure at the various mixture ratios. The general trend of the data in this figure is increasing performance with decreasing mixture ratio and increasing performance with decreasing chamber pressure. The only exception to the general trend is that at chamber pressures of 15 psia and below, higher performance was obtained at r = 10 than at r = 8. This can probably be attributed to vaporization effects.

(C) The trend of increasing performance with decreasing mixture ratio at a given chamber pressure also points out that for the same momentum ratio it is easier to obtain high performance at low mixture ratios, a result that has been observed at high pressures.

(C) The trend of increasing performance with decreasing chamber pressure is most likely the result of increased vaporization in the oxidizer manifolds at low chamber pressures. As pointed out in subparagraph b, the oxidizer manifold pressures are below the vapor pressure for most conditions and as chamber pressure decreases, so does the manifold pressure, causing an increase in vaporization.

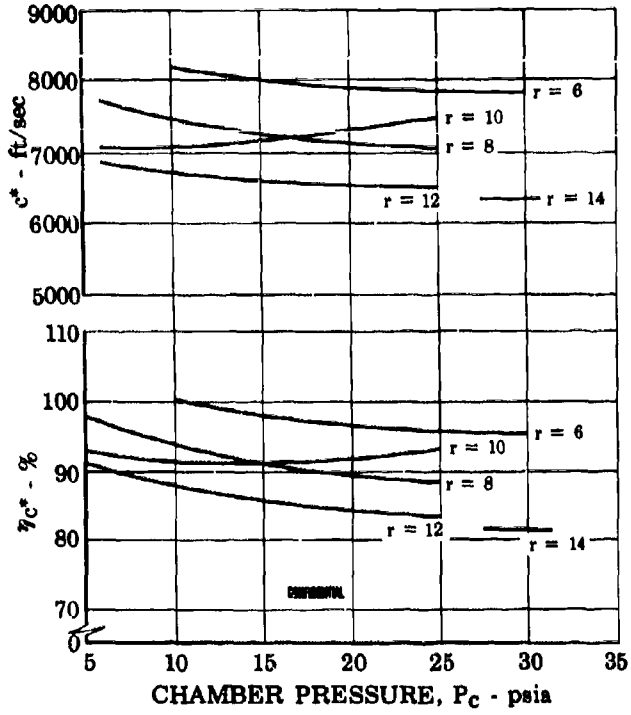

Figure 41. c* and η_{c^*} Performance for Optimum Flow Splits FD 20965

4. Throttling Performance

(C) With the flow divider valve set to provide the optimum flow split at each thrust level, good performance was obtained over a chamber pressure range of 850 to 5 psia (i.e., over a thrust range of approximately 170 to 1). The lowest chamber pressure obtained was 4.37 psia at a mixture ratio of 12 and a flow split of 100%. The performance data obtained with near optimum flow splits are presented in figure 42 as a function of thrust. The figure shows all the data obtained during both the altitude and sea level tests. The figure shows that for mixture ratios of from 4.9 to 15.2, performance above 82% was obtained over the entire thrust range.

(C) Figure 43 presents the performance data obtained with near optimum flow splits at mixture ratios of 10 and below as a function of thrust. Note that by operating in this mixture ratio range that high performance could be obtained over the entire thrust range.

(C) At the lower thrust levels (below 10%) mixture ratio has a more decided effect on performance. The difference in performance between r = 12 and r = 6 is as much as 15% at a chamber pressure of 25 psia, whereas at the higher thrust and chamber pressure levels (i.e., 300 to 850 psia) less than approximately 4% performance difference exists between r = 8 and r = 12.

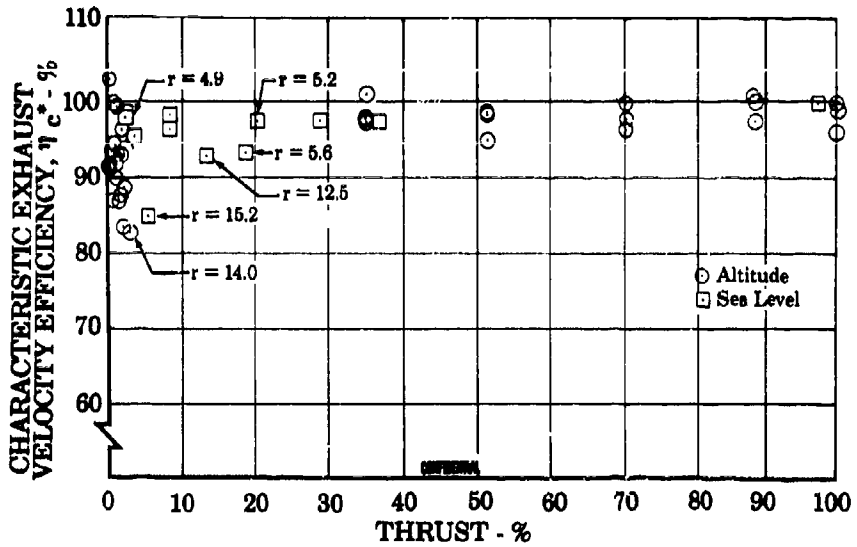

Figure 42. 8.5K Injector Throttling Performance for Optimum Injector Flow Splits FD 20949

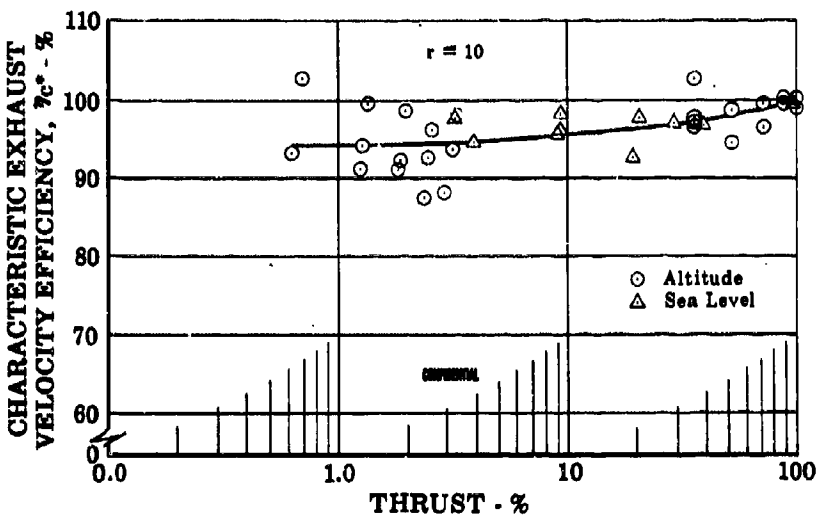

Figure 43. 8.5K Injector Throttling Performance for $r \leq 10$ and Optimum Injector Flow Splits FD 20988

(C) The effect of primary-to-total oxidizer flow split was extensively investigated at the lower thrust levels (below 4%) in the altitude tests. In the sea level testing the effect of flow split was investigated at the higher thrust levels. The results of these investigations are presented in figure 44. In the figure, the optimum flow split (the flow split that provides highest performance) is plotted as a function of thrust for mixture ratios of 6, 8, 10, 12, and 14. Note that the optimum flow split increases

with decreasing thrust from approximately 8% at 100% thrust to 87% at 0.6% thrust and at a mixture ratio of 6. Note also that mixture ratio becomes increasingly important to the optimum flow split as thrust decreases. At above approximately 40% thrust the mixture ratio effect is negligible. At 0.6% thrust the difference in optimum flow split between r = 6 and r = 14 is approximately 40%. Also shown as a reference in figure 44 is the curve presented following the sea level tests. The curves obtained during the altitude tests are considered to be more accurate at the lower thrust levels because they are based on more data.

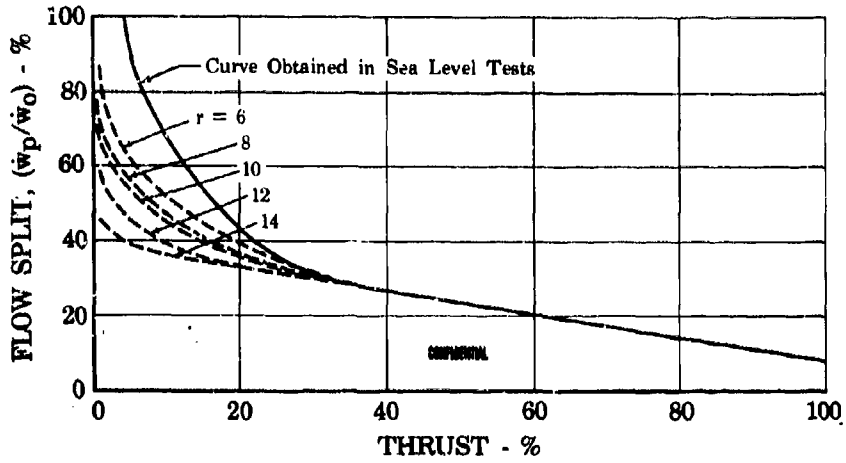

Figure 44. Variation of Optimum Injector Flow Split With Thrust and Mixture Ratio FD 20944

5. Data Computations and Performance Corrections

a. Data Computations

(U) The throat stagnation pressure was computed from chamber pressure measurements made at (1) the injector face and (2) the nozzle inlet. The face-tap chamber pressure was corrected for a momentum loss whereas the nozzle inlet-tap measurement was used directly. The c* calculation procedure is indicated in figure 45. As shown, the characteristic exhaust velocity was computed from measurements of propellant flow rates and nozzle throat flow area as well as chamber pressure. Characteristic exhaust velocity efficiency was computed by ratioing the measured c* to a theoretical c* based on shifting equilibrium that was corrected for the heat rejection to the chamber.

(C) In the high chamber pressure tests (300 - 850 psia), c* data as well as thrust and specific impulse data were obtained. As before, the c* data were computed by the procedure indicated in figure 45. From thrust measurements, specific impulse data and nozzle performance were

computed. The specific impulse data were computed as indicated in figure 46. Vacuum thrust was computed from measured thrust by subtracting pressure-area forces acting on the chamber and adding the thrust system tare. The term, A_a, used in figure 46, is the projected area subjected to ambient pressure (figure 47). The term $(A_e - A_b)$ is the projected area subjected to half-shell pressure. Specific impulse efficiency was computed by dividing the measured specific impulse value by the theoretical specific impulse for shifting equilibrium that is corrected for the heat loss to the chamber and the nozzle extension.

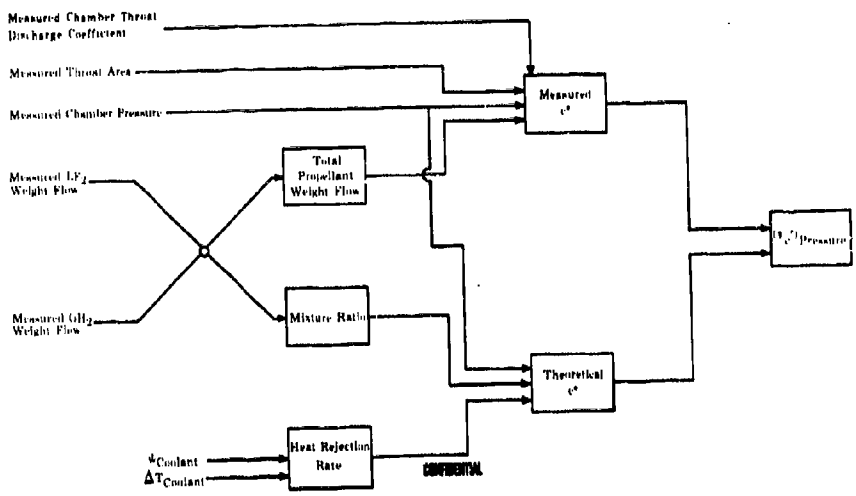

Figure 45. Block Diagram Illustrating Calculation of Chamber-Pressure-Based c* Efficiency Data

FD 14517A

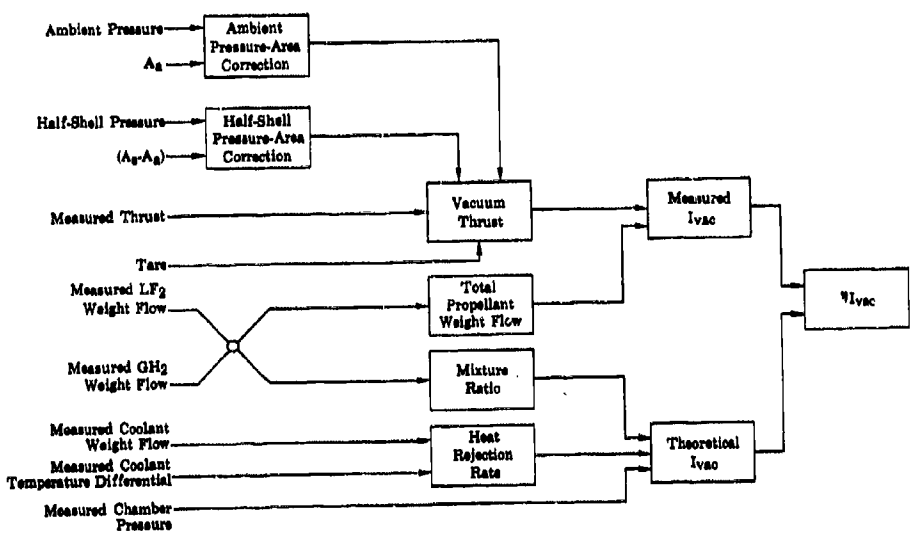

Figure 46. Block Diagram Illustrating Calculation of Specific Impulse Data

FD 14965

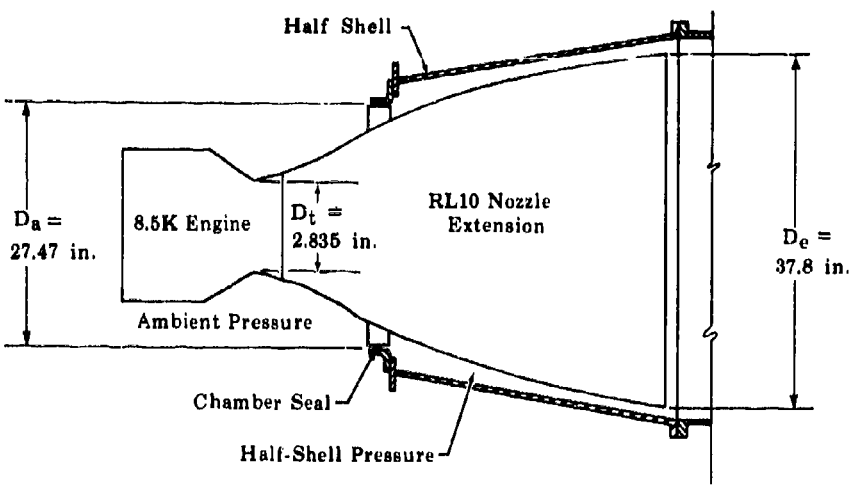

Figure 47. 8.5K Engine Installation in the Altitude System FD 14889A

b. Performance Corrections

(1) Momentum Loss

(U) The characteristic exhaust velocity efficiency data presented in this report were computed from two different chamber pressure taps. The face tap, which was located in the chamber wall near the injector face, was corrected for a 0.5% theoretical momentum loss, which was computed by the methods described in Reference 4. The chamber-tap measurements (taken just upstream of the point where the chamber begins to converge to the throat) were used directly, i.e., uncorrected for a momentum loss. The total pressure determined from the static pressure measurement at the chamber tap was assumed to be equal to the throat total pressure (thus the losses in the convergent part of the nozzle were neglected).

(U) By ratioing the measurements taken from the two chamber taps an experimental value for the momentum loss can be computed and compared with the theoretical value (figure 48). Note that the experimental values agree with the theoretical values within ± 2% over the entire thrust range. Experience at Pratt & Whitney Aircraft has shown that the level of chamber pressure measured at the injector face is greatly affected by the location of the pressure tap and that chamber pressure measurements made near the nozzle are more reliable, hence in the data comparison presented in previous paragraphs the chamber-tap based c* efficiency was used.

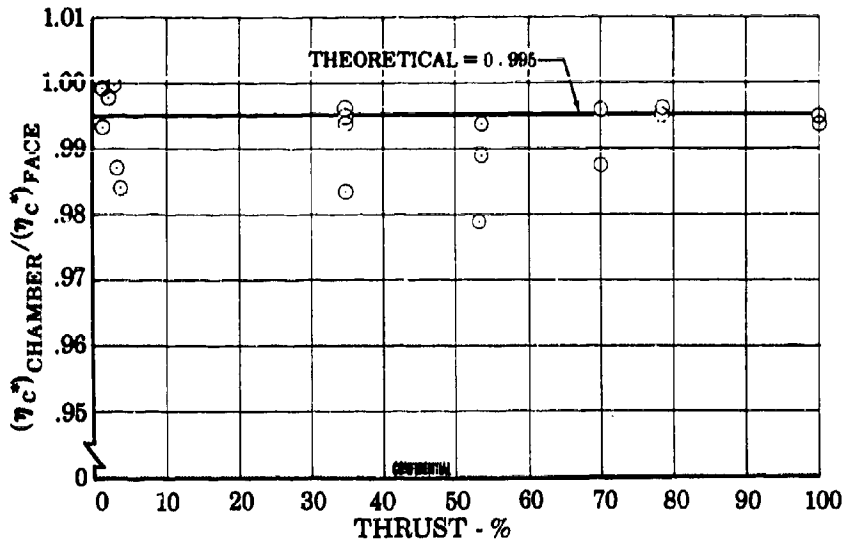

Figure 48. Comparison of Experimental and Theoretical Chamber Momentum Loss FD 20984

(2) Heat Loss

(U) The theoretical values of specific impulse and characteristic exhaust velocity used in computing $\eta_{I_{vac}}$ and η_{c^*} were adjusted to account for heat transferred to the hydrogen coolant. This heat loss and, therefore, performance loss, would not occur in a regeneratively cooled F_2/H_2 engine. In this type engine, the heat would be transferred to the hydrogen used to cool the thrust chamber, which would subsequently be injected into the combustion chamber and, thus, the heat transferred to the hydrogen would not be lost. Values of η_{c^*} and $\eta_{I_{vac}}$ indicative of those values that could be obtained in a regeneratively cooled F_2/H_2 engine were, therefore, computed from the 8.5K data by using theoretical values that were lowered to account for heat loss. Tables X and XI show the measured heat loss parameters and respective performance corrections for the high and low chamber pressure altitude tests, respectively.

(U) Since the coolant passages of the copper chamber extend out beyond the throat and into the nozzle section (figure 49), a small error in the theoretical c* calculation was introduced in using the heat transferred to the copper chamber for the heat loss correction. The area ratio of the sea level chamber is only 4.2 and thus the heat transferred in the supersonic region is estimated to be small enough to introduce negligible error.

(U) Figure 50 shows the measured heat rejection rate (obtained from measurements of the hydrogen coolant flow rate and its temperature rise thrcugh the chamber and nozzle extension) for both low and high chamber pressure tests as functions of thrust. The magnitude of the correction for heat loss to the thrust chamber is illustrated in figure 51, where the ratios of corrected to uncorrected efficiencies are presented. The The heat loss corrections for c* data are between 0.5% and 2.5% with the largest corrections being made at low thrust. The specific impulse corrections also decrease with increasing thrust and range from 1 to 2%.

(C) Table X. 8.5K Performance Corrections Due to Heat Loss - Low Chamber Pressure

Mixture Ratio	Chamber Pressure, psia	Flow Split, %	Coolant Weight Flow, lb/sec	Chamber Temperature Rise, °R	Nozzle Extension Temperature Rise, °R	Total Coolant Enthalpy Rise, Btu/sec	Total Coolant Enthalpy Rise Per Pound of Propellant Flow, Btu/lb	Theoretical c^* Uncorrected for Heat Loss, ft/sec	Theoretical c^* Corrected for Heat Loss, ft/sec
6	25	50	0.506	52.7	12.9	117.8	173.6	8325	8270
		75	0.495	62.5	12.5	131.3	194.6	8340	8271
		100	0.488	70.8	19.4	155.9	230.8	8325	8244
8	25	100	0.473	78.4	30.0	181.1	265.1	8110	8029
		75	0.469	75.5	24.5	165.8	241.6	8135	8048
		50	0.478	88.0	12.8	170.6	247.6	8120	8029
10	25	50	0.473	99.4	12.1	189.5	264.9	7980	7887
		75	0.477	104.8	15.5	206.2	292.5	7985	7885
		100	0.473	95.9	33.6	219.7	311.8	7960	7875
12	25	100	0.468	102.0	61.8	271.4	383.4	7855	7759
		75	0.470	90.6	30.3	201.3	283.9	7870	7784
		50	0.469	101.6	16.0	195.0	275.5	7880	7781
6	20	50	0.593	59.0	5.9	135.9	248.4	8305	8198
		75	0.579	64.1	9.2	149.6	274.2	8305	8204
		100	0.583	63.9	25.4	184.4	337.3	8300	8191
8	20	100	0.471	66.0	41.2	222.7	402.4	8090	7979
		75	0.575	62.6	23.6	175.6	314.4	8095	7990
		50	0.578	72.4	13.1	175.8	314.5	8090	7984
10	20	50	0.583	75.7	13.2	183.1	323.0	7965	7839
		75	0.593	76.4	17.4	193.8	343.2	7955	7841
		100	0.568	67.9	46.3	227.6	403.1	7925	7836
12	20	100	0.568	66.7	75.2	280.7	493.6	7830	7733
		75	0.573	73.4	22.5	228.0	339.1	7845	7740
		50	0.578	75.8	17.8	224.6	333.8	7850	7740
6	15	50	0.432	62.9	6.9	120.1	293.7	8305	8178
		75	0.443	48.9	7.6	119.5	292.8	8310	8184
		100	0.478	64.8	35.4	169.9	417.3	8305	8177
8	15	100	0.486	69.6	54.8	202.3	486.4	8085	7955
		75	0.436	71.4	12.0	128.8	307.4	8320	7968
		50	0.444	83.3	11.1	147.9	352.1	8325	7454
10	15	50	0.438	86.2	11.3	151.2	356.6	7925	7802
		75	0.464	85.9	13.5	156.2	368.4	7925	7804
		100	0.440	82.3	52.1	208.0	490.5	7905	7738
12	15	100	0.431	85.0	54.3	212.9	500.9	7805	7684
		75	0.445	81.1	25.9	167.9	391.5	7825	7703
		50	0.460	91.4	19.2	179.9	418.4	7815	7674
6	10	50	0.501	47.9	13.8	109.8	388.0	8215	8101
		75	0.438	53.2	16.4	107.8	387.6	8220	8102
		100	0.463	55.8	42.6	161.4	578.5	8225	8095
8	10	100	0.468	60.7	64.3	207.2	724.7	8015	7876
		75	0.480	56.5	26.3	140.4	490.8	8010	7882
		50	0.460	58.9	12.2	135.6	404.1	8015	7879
10	10	50	0.445	60.0	12.5	114.0	390.4	7865	7748
		75	0.443	57.3	16.6	116.2	398.0	7850	7736
		100	0.460	57.7	36.8	134.7	531.6	7865	7739
12	10	100	0.455	58.3	36.0	131.8	516.2	7760	7638
		75	0.441	59.0	13.4	116.4	394.8	7780	7640
		50	0.481	59.8	15.4	127.8	433.4	7770	7632
6	5	50	0.486	46.2	11.7	95.6	645.8	8165	7937
		75	0.462	36.4	29.2	107.2	739.5	8140	7966
		100	0.444	38.0	53.7	231.0	998.8	8155	7990
8	5	100	0.444	42.2	48.5	142.4	968.7	7925	7752
		75	0.478	43.4	12.9	94.8	644.6	7940	7746
		50	0.485	41.3	11.5	90.2	609.5	7920	7734
10	5	50	0.451	42.4	14.0	89.6	597.4	7760	7597
		75	0.478	37.8	31.7	118.8	796.8	7785	7614
		100	0.483	37.7	49.8	149.1	1000.2	7755	7590
12	5	100	0.487	38.4	35.0	126.1	843.3	7660	7482
		50	0.486	40.2	39.7	136.2	908.3	7680	7493
		75	0.448	44.1	48.4	145.5	970.3	7680	7491

(C) Table XI. 8.5K Performance Corrections Due to Heat Loss - High Chamber Pressure

Test No.	Chamber Pressure, psia	Mixture Ratio	Coolant Weight Flow, lb/sec	Chamber Temperature Rise, °R	Nozzle Extension Temperature Rise, °R	Total Coolant Enthalpy Rise, Btu/sec	Total Coolant Enthalpy Rise Per Pound of Propellant Flow, Btu/lb	Theoretical c* Uncorrected for Heat Loss, ft/sec	Theoretical c* Corrected for Heat Loss, ft/sec	Theoretical I_{vac} Uncorrected for Heat Loss, ft/sec	Theoretical I_{vac} Corrected for Heat Loss, ft/sec
9	303	7.73	1.876	161.0	99.3	1729.0	234.9	8387	8311	500.5	490.2
	303	9.64	1.943	163.2	99.2	1804.3	250.2	8271	8196	502.0	491.8
11	601.0	8.17	2.533	198.6	133.6	2979.5	203.2	8422	8356	501.2	493.0
	603.0	10.26	2.421	223.4	145.6	3162.0	219.8	8288	8239	503.0	496.3
	603.0	12.25	2.297	236.7	149.3	3138.3	210.7	8207	8151	503.4	495.1
12	303.4	7.92	2.306	134.2	78.7	1739.5	235.9	8370	8179	500.7	489.7
	303.5	10.12	2.315	140.2	85.2	1838.9	246.9	8235	8044	502.2	491.1
	303.6	12.01	2.301	145.0	89.0	1906.6	252.5	8145	7943	502.4	490.9
14	749	8.05	2.435	242.49	126.0	3181.8	182.8	8440	8383	501.5	494.2
	750	9.95	2.258	283.36	136.9	3419.9	192.0	8328	8278	503.1	495.8
	750	11.92	2.130	306.39	146.2	3412.7	185.1	8246	8190	503.9	496.7
15	850	8.10	2.453	265.33	130.05	3434.3	172.9	8445	8392	501.6	494.9
	847	10.40	2.467	293.99	147.33	2854.0	190.2	8320	8270	503.3	496.4
	849	12.11	2.473	304.79	148.77	3971.5	188.1	8255	8199	503.9	497.1

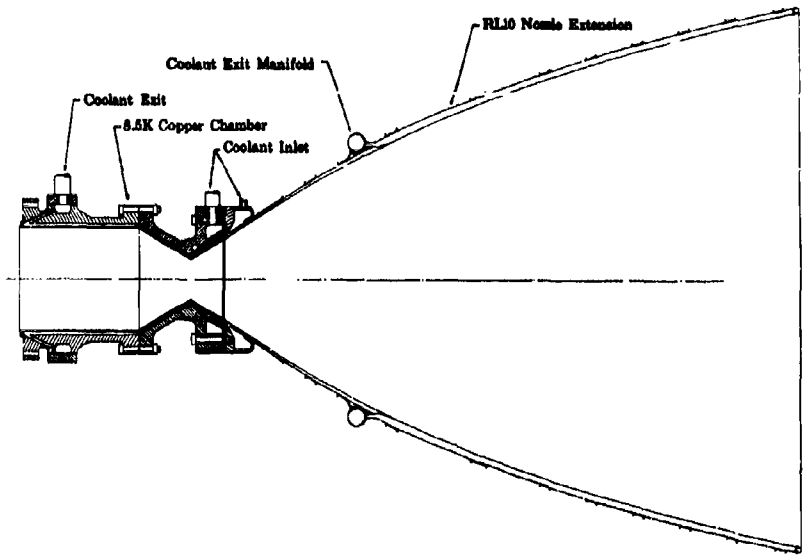

Figure 49. 8.5K Sea Level Chamber With RL10 Nozzle Extension FD 13324

(3) Nozzle Discharge Coefficient

(U) During the test program it was suspected that the combustion chamber throat area discharge coefficient was large enough to contribute a major correction to combustion performance. Consequently cold flow tests were made with the nozzle using nitrogen gas to determine the actual discharge coefficient.

(U) The nozzle was calibrated in position in the LPRF test stand where the hot firings were made. The altitude steam exhauster system was used so that the chamber throat area would be choked at chamber pressures of 10, 15, and 20 psia. The test results are shown in table XII. The nozzle effective area was calculated from the following compressible flow relationship.

$$\frac{\dot{w}\sqrt{T_T}}{AC_d P_c} = K$$

where K is a constant for choked flow; P_c is the nozzle stagnation pressure; $\dot{w}$ is the gaseous nitrogen flow rate and AC_d is the effective throat flow area of the sea level chamber.

(U) An average value of 0.965 was determined from the test results for the nozzle throat discharge coefficient. This value is compared with similar nozzle calibrations (Reference 5) and is shown in figure 52.

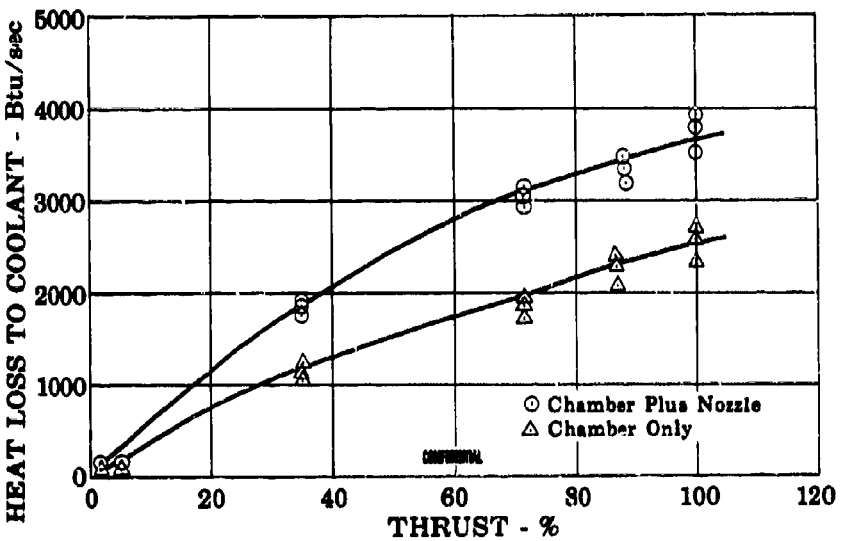

Figure 50. Thrust Chamber Heat Loss FD 20985

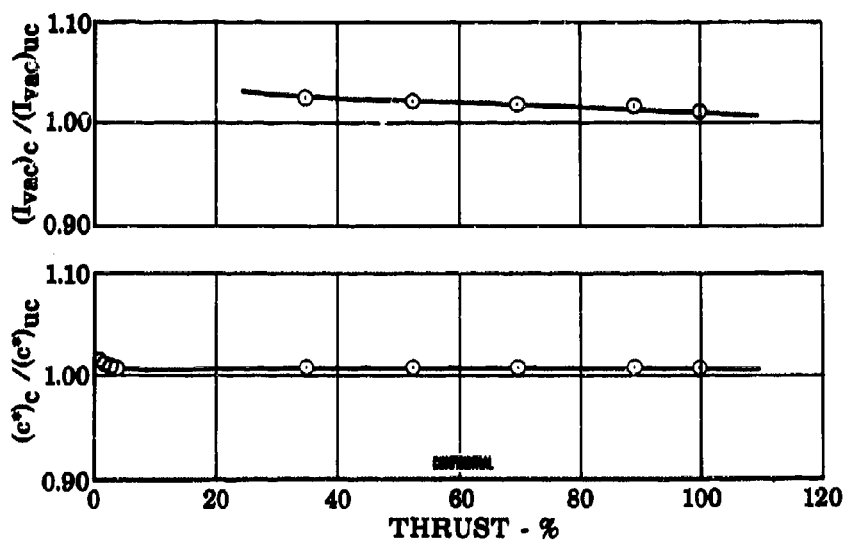

Figure 51. Magnitude of Heat Loss Correction FD 20950

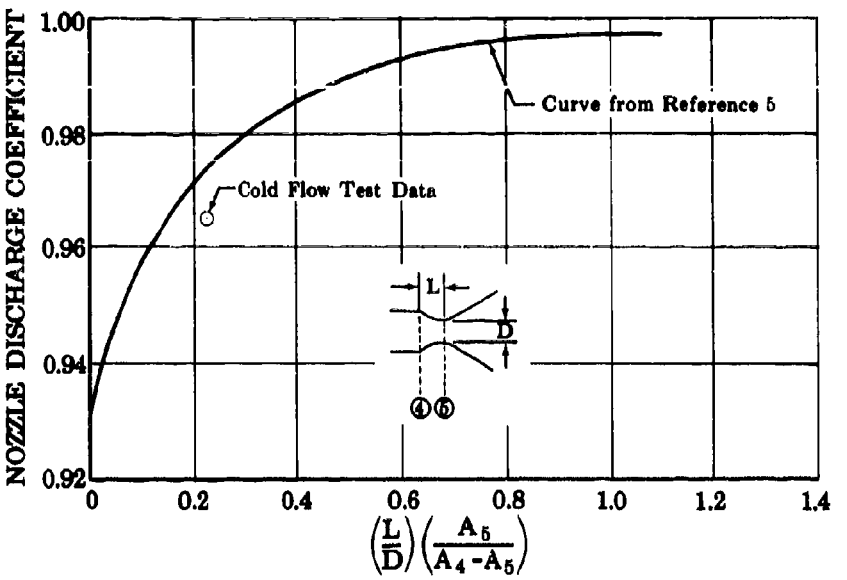

Figure 52. Nozzle Discharge Coefficient as a Function of the Nozzle Dimensions FD 20974

(U) Table XII. 8.5K Nozzle Calibration

Nitrogen Gas Flow Rate, lb/sec	Chamber Pressure, P_c, psia	Temperature, °R	AC_d	C_d
2.779	20.04	532.1	6.088	0.964
2.109	15.14	531.9	6.124	0.970
1.387	10.04	530.2	6.072	0.962

(C) The Reynolds number of the nitrogen flow during the tests was approximately 2.5×10^5 at 15 psia chamber pressure. A check of this Reynolds number with established ASME curves (Reference 6) showed that at this value and above, the discharge coefficient remains fairly constant. It also showed that below this value the discharge coefficient begins to decrease. Figure 53 was constructed based on the ASME curves and the test data and shows the decrease in discharge coefficient with Reynolds number. The Reynolds number for the hot firings is shown in figure 54 as a function of percent thrust. Figure 54 shows, that for chamber pressures of 15 psia and above, a constant discharge coefficient of 0.965 can be used. For the 5- and 10-psia chamber pressure tests, discharge coefficients of 0.955 and 0.963, respectively, were used. The discharge coefficients were used directly in the calculation of c* and thus reduce the c* efficiency values. The 8.5K sea level test results obtained in Contract AF 04(611)-9965 and presented again in this report were also corrected to reflect this adjustment.

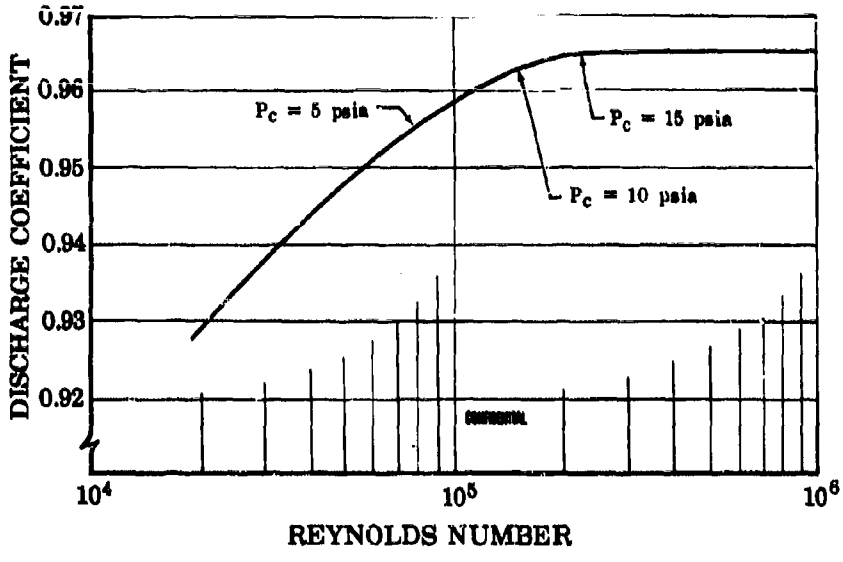

Figure 53. Variation of 8.5K Nozzle Discharge Coefficient

FD 20993

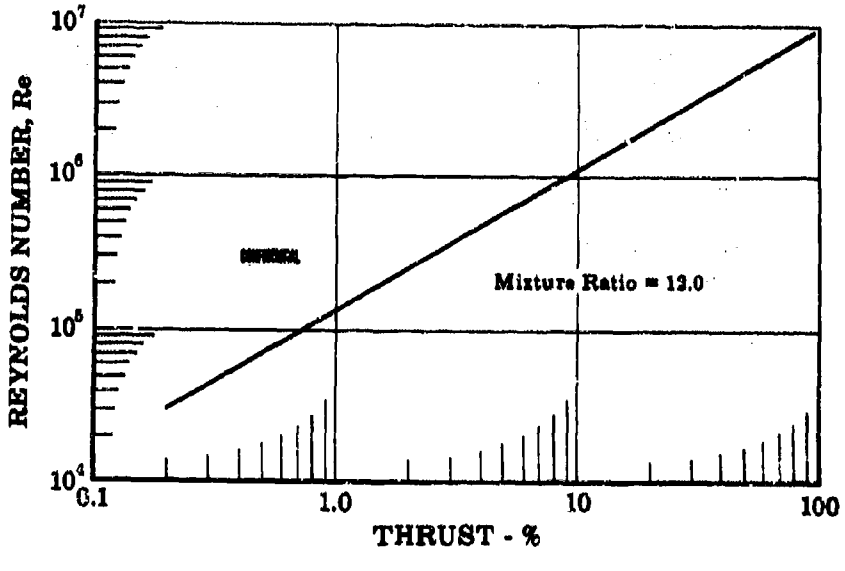

Figure 54. 8.5K Nozzle Reynolds Number vs Percent Thrust

FD 20995

c. Data Errors Due to Supply Line Storage Effects

(U) If the fluorine density in the supply line is changing during a data-taking period, then the measured fluorine flow will not be equal to the flow that is being injected into the chamber. In the test stand, the fluorine supply line between the fluorine flow nozzle and the injector is a 3-in. diameter line that is approximately 25 feet long; the line volume is 1.142 ft^3. The mass change in this volume is related by the following equation to changes in the average fluorine-mass temperature

$$\frac{dw}{d\theta} = \frac{d\rho}{d\theta} V = \frac{d\rho}{dT}\frac{dT}{d\theta} V = \dot{w}_N - \dot{w}_I$$

where:

$\frac{dw}{d\theta}$ = the change of the fluorine mass in the supply line with respect to time

$\frac{d\rho}{d\theta}$ = change of the fluorine density in the supply line with respect to time

V = volume of the supply line (1.142 ft^3)

$\frac{d\rho}{dT}$ = change of fluorine density with respect to temperature, which for the temperature range from 170°R to 120°R is 0.222 lb_m/ft^3-°R.

$\frac{dT}{d\theta}$ = fluorine density temperature change with respect to time

$\dot{w}_N$ = fluorine flow through the flow nozzle

$\dot{w}_I$ = fluorine flow through the injector.

(C) If the average fluorine-mass temperature in the supply line is changing with time (i.e., if $dT/d\theta$ is different from zero), the mass in the line will not be constant ($dw/d\theta$ will not be zero) and the injector fluorine flow ($\dot{w}_I$) will not be equal to the nozzle flow ($\dot{w}_N$). Figure 55 was prepared to indicate potential magnitudes of errors due to changes in average fluorine-mass temperature. The upper graph in figure 55 shows the storage effect of the supply line (i.e., the change in the fluorine mass in the line) as a function of changes in the average fluorine-mass temperature ($dT/d\theta$). The lower graph shows the error in measured fluorine flow (computed by dividing the term $dw/d\theta$ by the propellant flow rate) for chamber pressures from 300 to 850 psia. The magnitude of the error decreases with increasing chamber pressure and therefore fluorine flow. Although a very accurate determination of $dT/d\theta$ would require many thermocouples located along the supply line, an estimate of $dT/d\theta$ can be made from the temperature measurements made at the flow nozzle and injector. Figures 56 through 60 show the time variations of the fluorine temperatures in the supply line at the upstream (ONT) and downstream (ONET) nozzle locations and at the injector. The temperature OPIT and OSMT are the fluorine primary and secondary injector temperatures, respectively. Note in the figures that the nozzle temperatures are low during the entire test. Also, the primary injector temperature is low throughout the test because the primary injector has a liquid nitrogen cooldown jacket. The fluorine flow through the secondary injector gets colder throughout the first half of the tests

(i.e., the first 15 seconds) as indicated in the figures by the fact that OSMT decreases. If OSMT is used to assess the storage effect of the line, it can be concluded that the r = 8 data in all tests could be low because OSMT was still decreasing when it was taken. For example, it appears that OSMT is decreasing at the rate of about 0.5 to 1.0 degree/sec in all tests during the r = 8 data point period. Using an average value of 0.75 degree/sec for $dT/d\theta$ in figure 55, the measured flow could be as much as 1 to 2.6% too high and therefore the c* and I_{vac} could be as much as 0.9 to 2.3% too low. As indicated in figure 55, the error introduced would be largest at the lowest chamber pressures (i.e., 300 and 450 psia).

(U) To minimize this storage effect, it is desirable to locate the flow nozzle as close as possible to the injector so that the volume will be minimized, as was done in the low chamber pressure tests. Also the test time could be increased to ensure that temperature equilibrium is established before data for each test are obtained or the r = 8 data point could be repeated later in the test.

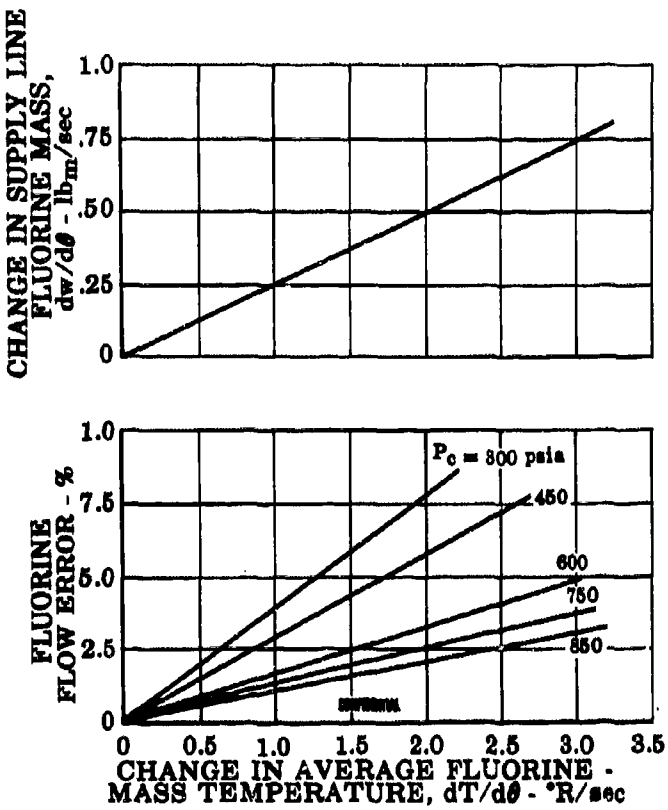

Figure 55. Fluorine Supply Line Storage Effects FD 20968

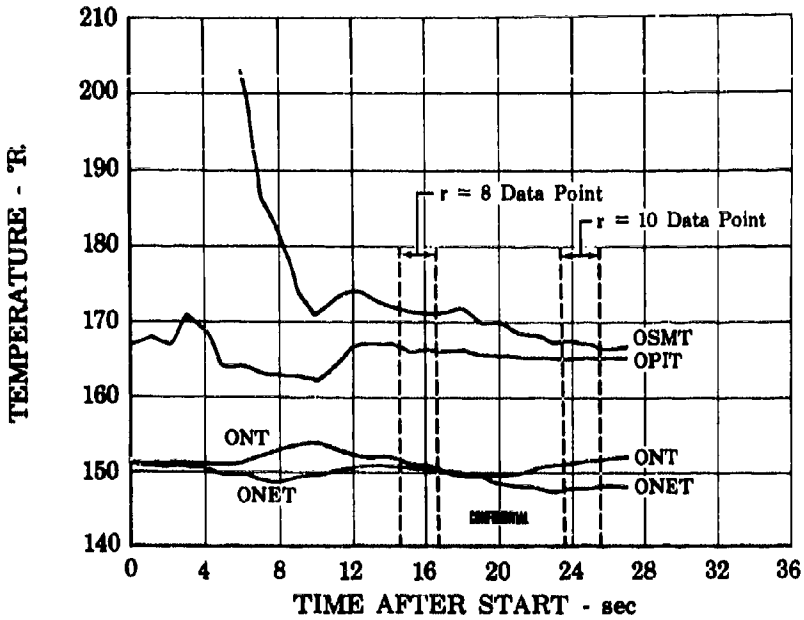

Figure 56. Fluorine Temperatures - Test No. 9, P_c = 300 psia FD 20997

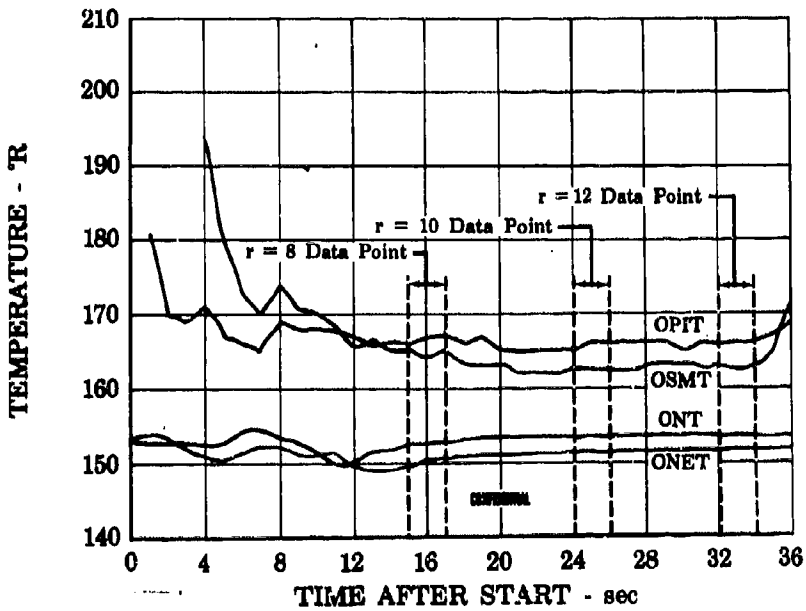

Figure 57. Fluorine Temperatures - Test No. 11, P_c = 600 psia FD 21000

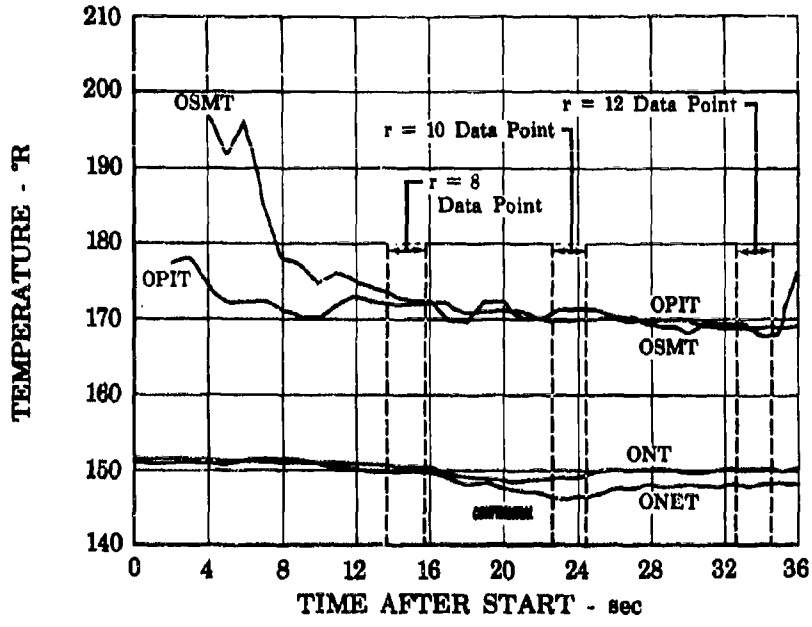

Figure 58. Fluorine Temperatures - Test No. 12, P_c = 300 psia FD 20999

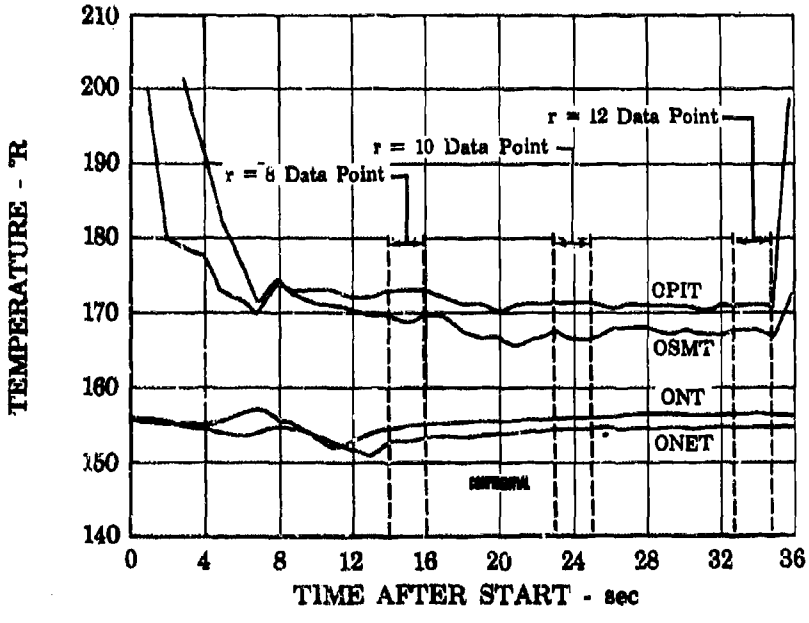

Figure 59. Fluorine Temperatures - Test No. 14, P_c = 750 psia FD 20998

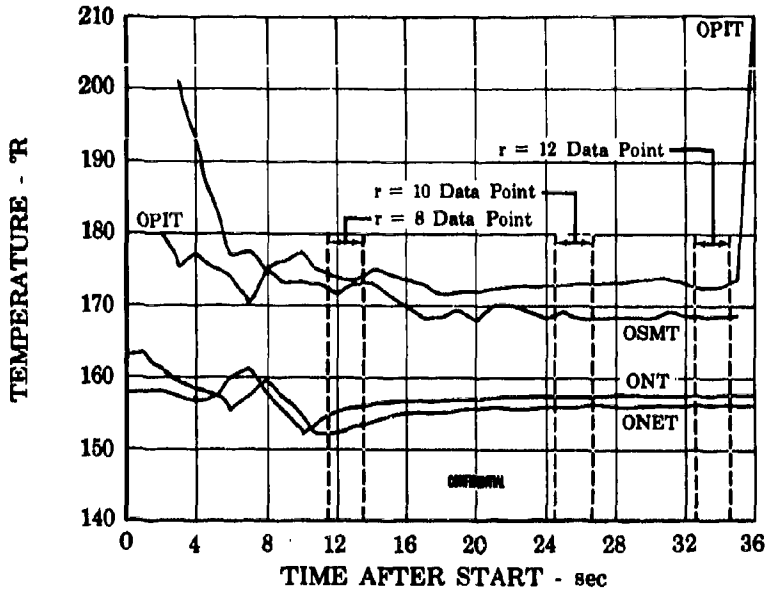

Figure 60. Fluorine Temperatures - Test No. 15, P_c = 850 psia FD 20954

SECTION V
TEST HARDWARE

A. GENERAL

(U) The hardware residual from the sea level 8.5K test program conducted under Contract AF 04(611)-9965 was used in the altitude tests under this contract. This residual hardware included (1) one 8.5K dual-orifice injector and (2) two mating copper workhorse sea level chambers. To supplement this hardware, the following was fabricated under this follow-on contract:

1. An 8.5K dual-orifice injector with a more permeable Rigimesh injector faceplate (120-scfm rating compared with the 40-scfm Rigimesh used in the sea level tests)

2. A 120-scfm Rigimesh faceplate for the residual 8.5K injector

3. A backup 200-scfm Rigimesh faceplate

4. Two nozzle extensions made from RL10 rocket engine thrust chambers.

(U) The test engine assembly (figure 61) consisted of an 8.5K injector, a sea level chamber and a nozzle extension. The design and construction of these component parts are discussed separately in the paragraph B following. Paragraph C presents photographs of the hardware after test and discusses durability.

B. HARDWARE DESCRIPTIONS

1. Injectors

a. Description

(U) The 8500-lb thrust injector assembly is illustrated in figures 62 and 63. The injector consists of five major parts, which are shown in figure 64 arranged as they would be assembled together. These parts include:

1. Fuel manifold
2. Injector faceplate
3. Oxidizer secondary spudplate
4. Oxidizer primary spudplate
5. Backplate.

The fuel manifold holds the injector faceplate in position and distributes the fuel to the cavity between the faceplate and the oxidizer secondary injector spudplate.

(U) The injector has a 15-degree conical Rigimesh faceplate. The fuel injection orifices are drilled in the Rigimesh to form elements concentric with the fluorine injector spuds. The orifice holes were finished to their final dimensions by electrical discharge machining, which restores porosity and thus ensures cooling in the machined areas. The faceplate is transpiration-cooled by gaseous hydrogen.

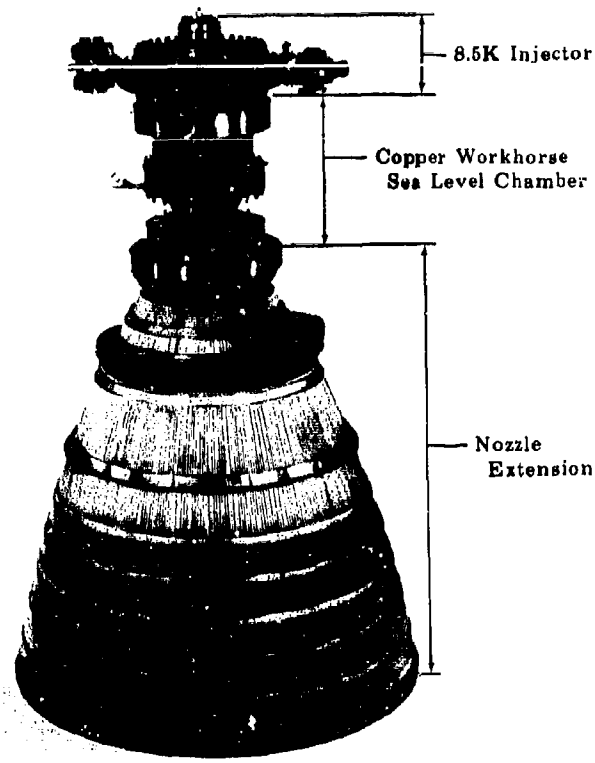

Figure 61. 8.5K Engine Assembly FD 21502

(U) The last three parts that form the fluorine injector were fabricated from either Inconel or nickel; these materials are resistant to both liquid and gaseous fluorine (Reference 7). The secondary injector spudplate was constructed from nickel. The secondary injector spuds are an integral part of the plate (machined from the same nickel stock). The primary spuds were also fabricated from nickel and were brazed into the primary injector (Inconel) spudplate using a gold-nickel braze alloy.

(U) The oxidizer secondary supply manifold is a part of the primary spudplate, as shown in figure 62. Thirty-four holes supply fluorine to the secondary injector cavity between the primary and secondary injector spudplate. Fluorine to the primary injector was supplied from an inlet in the backplate. The backplate also has a liquid nitrogen coolant jacket, which keeps the injector cool and therefore ensures (1) a minimum injector cooldown time and (2) that liquid (rather than gaseous) fluorine is supplied to the primary injector. In the tests, LN_2 at approximately 35 psia and 150°R was supplied to this jacket. The exit jacket nitrogen temperature was approximately 300°R.

FD 12164A

Figure 62. 8.5K, F_2/H_2 - Dual-Orifice Injector

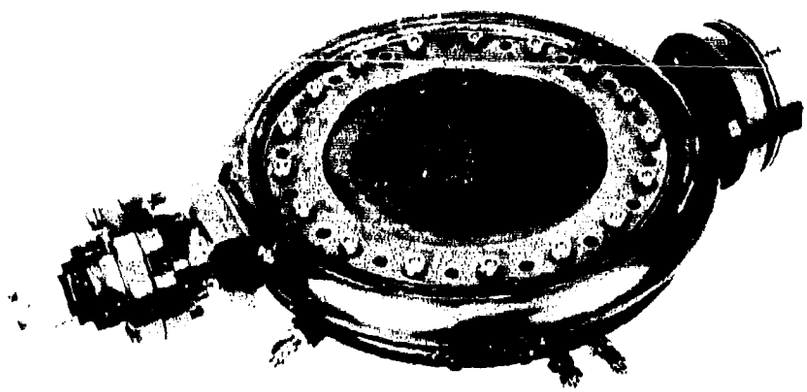

Figure 63. 8.5K Injector Assembly FE 54125

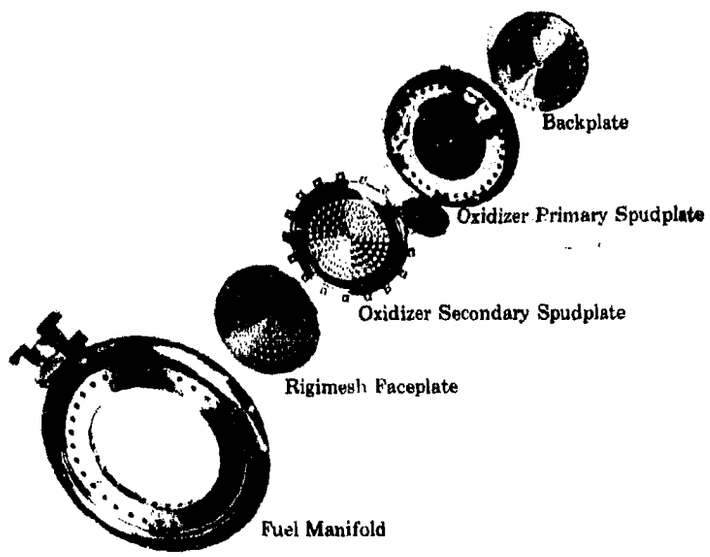

Figure 64. 8.5K Injector Parts FD 14994

(U) Injector parts in contact with fluorine were cleaned and passivated in detail and then the fluorine injector (consisting of the backplate, the primary injector spudplate, and the secondary injector spudplate) was assembled and passivated as an assembly before installing the Rigimesh faceplate and fuel manifold.

(U) The fluorine injector inlet flanges have serrated seal surfaces for use with aluminum crush gaskets. Delta-ring type seals are used on the hydrogen inlet flange.

b. Seals

(U) As shown in figure 62 double seals were used in the injector between (1) the backplate and the fluorine primary injector spudplate and (2) the fluorine secondary and primary spudplates. In the sea level tests, K-seals plated with a silver-lead alloy were used at these seal locations. The K-seals were not completely satisfactory; the silver-lead plating flaked off when subjected to fluorine and leaks occurred past the first seal. These leaks were detected by monitoring the pressure in the interseal bleed cavity.

(U) In the altitude tests, two types of seals were used. In the first three tests, Teflon TFE-coated stainless steel O-rings were used and leaks occurred by the inner seal. A post-test examination revealed that the Teflon coating had been eroded away at several locations thus causing the leaks. This was somewhat surprising because the Teflon-coated seals were passivated with gaseous fluorine before installing them in the injector. Based on this experience, it has been concluded that the Teflon-coated seals, although adequate for gaseous fluorine service are not necessarily adequate for liquid fluorine service.

(U) In the subsequent tests (the last 12 tests) aluminum-plated, stainless steel V-seals were used at the inner seal location for the liquid fluorine seals, and Teflon-coated O-rings were used at the outer seal location. Although the V-seals did not provide a gas-tight seal, they did not deteriorate in liquid fluorine service. To prevent liquid fluorine from contacting the Teflon-coated O-rings, the interseal cavity was pressurized with gaseous nitrogen at a slightly higher pressure than the fluorine injector manifold pressures. Furthermore because any leakage of nitrogen into the injector could result in erroneous performance data, an instrumented 0.060-inch diameter flow orifice was used to monitor the gaseous nitrogen flow into the seal cavity. No leakage occurred during any of the low-pressure tests. Furthermore, the highest leakage rate in the high-pressure tests occurred in test No. 12 at 300 psia chamber pressure where it was 0.009 lb_m/sec, which corresponds to only 0.117% of the total injector propellant flow at this thrust level; this has negligible effect on performance

(U) Teflon-coated O-rings were also used at both the inner and outer hydrogen injector seal locations for the injector-to-chamber seal, and between the sea level chamber and the nozzle extension. The Teflon-coated seals at these locations proved to be very satisfactory.

c. Injector Element Geometry

(C) The 8500-lb thrust injector has 114 concentric-type injection elements; the dimensions are shown in figure 65. Hydrogen is injected from an annular orifice surrounding the fluorine injector spuds; fluorine is injected by the concentric primary and secondary injector spuds that form the dual-orifice injector and provide the throttling capability. The injector orifices were originally designed to provide good performance over a 50 to 1 thrust range (i.e., for the 750- to 15-psia chamber pressure range) with mixture ratios of from 8 to 12. The results of this program show that the injector provides good performance over a 170 to 1 thrust range (i.e., for the 850- to 5-psia range) with mixture ratios from 6 to 12.

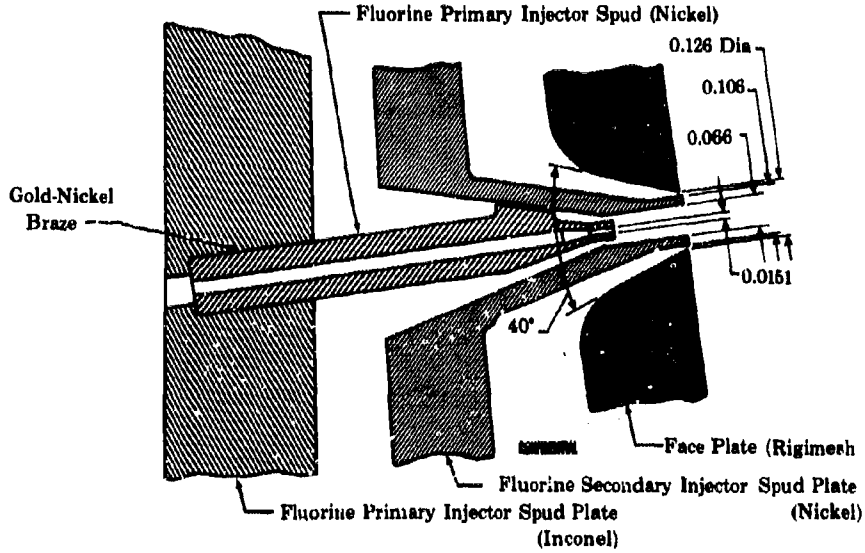

Figure 65. 8.5K, F_2/H_2 - Dual-Orifice Injector Element FD 12265A

(U) The primary injector spuds extend into the secondary injection orifices. As a result, the flow restriction in the secondary injector is the annular area around the primary spud. The fluorine injector was sized so that the primary injector pressure drop at maximum thrust and at a mixture ratio of 12 would be 150 psid. Although arbitrarily selected, this injector pressure drop was representative of that which could be used in a pump-fed engine. The variation of the injector pressure drops, the fluorine flow rate, and the injection velocity with mixture ratio is given in figure 66 for maximum thrust. The fluorine injection velocities given in this figure were computed for the circular orifice area (not the annular area) because fluorine velocity should decrease in the spud downstream of the annular restriction and thus be injected uniformly from the circular (0.066-in. diameter) orifice into the combustion chamber.

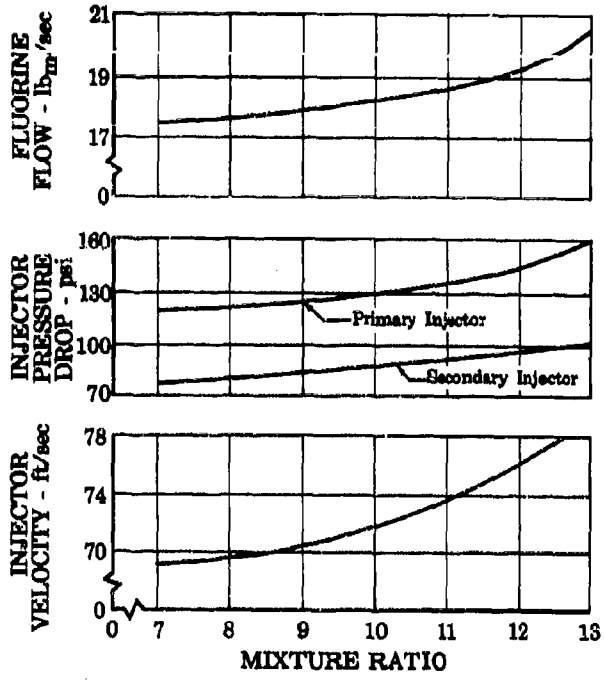

Figure 66. Variation of Fluorine Flow Rate, Injector Pressure Drop, and Injection Velocity With Mixture Ratio for the 8.5K Injector (Maximum Thrust) FD 20957

(U) Selection of the primary injector orifice diameter of 0.015 inch was based on the results of the 1000-lb thrust injector tests. In the 1000-lb thrust program, orifice diameters of 0.010 and 0.015 inch were evaluated with the 0.015-in. orifice injector providing higher performance.

(U) With the fluorine injection orifices sized, the fuel injector was originally sized so that the minimum fuel-to-oxidizer injection momentum ratio over the 8 to 12 mixture ratio range would be over 2.0. The resulting fuel annular injector orifices were 0.010-in. wide. Because of face burning that occurred during the sea level tests, a more permeable faceplate of 120 scfm was selected in this program, which reduced the fuel-to-oxidizer injection momentum ratio to 1.0 at a mixture ratio of 12 as shown in figure 67. The momentum ratio increases with decreasing mixture ratio so that at a mixture ratio of 8, the momentum ratio was approximately 2.15. It was not considered practical to reduce the fuel annular orifices appreciably to offset this decrease in fuel-to-oxidizer momentum ratio. The hole diameter in the Rigimesh was decreased, however, from 0.127 to 0.126 inch. With the new diameter, the nominal annular gap width is 0.0095 inch; however, because of the 0.007-in. tolerance on the spud-to-orifice location, the annular width could be as small as 0.0025 inch on one side of the spud and as large as 0.0165 inch on the other side. 0.0165 inch.

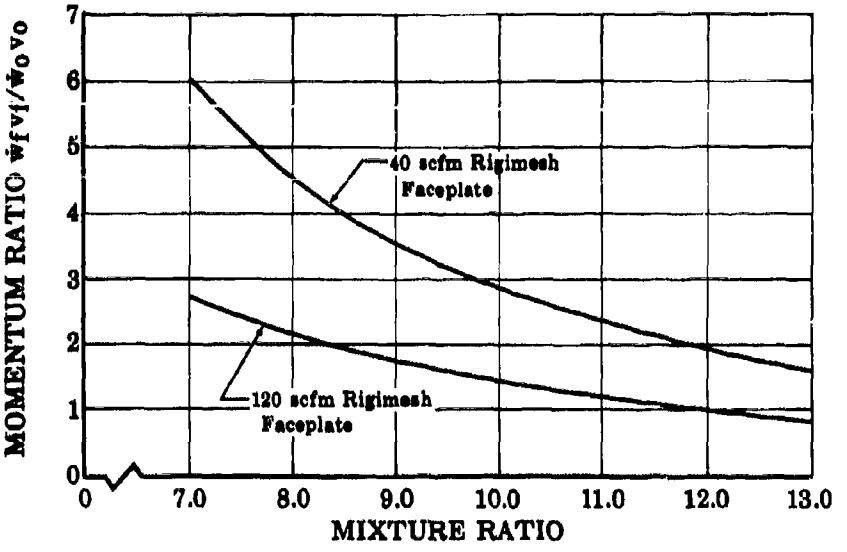

Figure 67. Variation of Momentum Ratio With Mixture Ratio for the 8.5K Injector (Maximum Thrust) FD 20928

(U) The hydrogen injection velocity and the injector pressure drop for the 120-scfm Rigimesh faceplate are shown in figure 68 for maximum thrust.

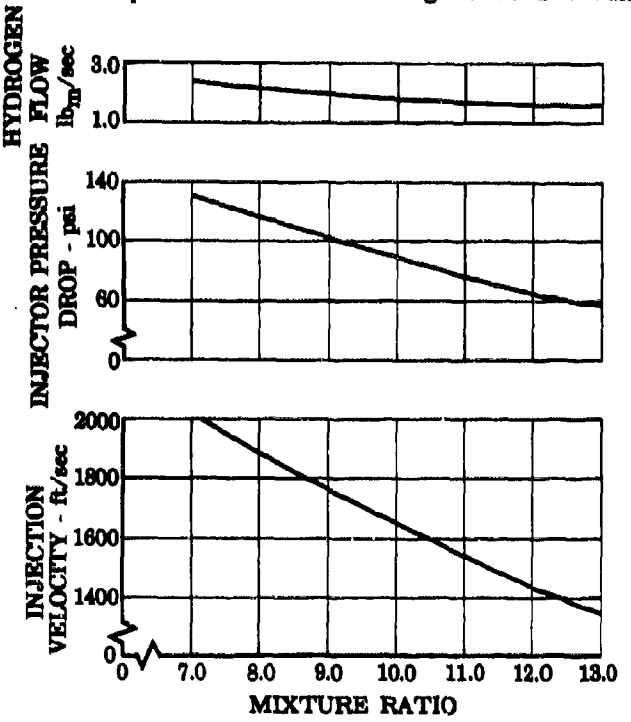

Figure 68. Variation of Hydrogen Flow Rate, Injector Pressure Drop, and Injection Velocity With Mixture Ratio for the 8.5K Injector (Maximum Thrust) FD 20930

d. Selection of Injector Faceplate Permeability

(C) The original 8.5K injector faceplate (like the subscale 1K injector faceplate evaluated under Contract AF 04(611)-9965) was made from Rigimesh with a 40-scfm permeability rating. The 40-scfm Rigimesh (flat) faceplate of the 1K injector was successfully tested at chamber pressures from 25 to 320 psia; the 8.5K injector (conical) faceplate was burned slightly at chamber pressures up to 300 psia and severely at 824 psia chamber pressure. Based on these test results it is apparent that (1) the heat fluxes to the conical faceplate of the 8.5K injector are higher than those to the flat faceplate of the 1K injector, and (2) the injector face heat flux increases more rapidly with chamber pressure than anticipated.

(U) As previously stated, the faceplates fabricated in this program were constructed from Rigimesh with permeability ratings of 120 and 200 scfm. Two 120-scfm faceplates were fabricated: one for the residual 8.5K injector and the other for the new 8.5K injector constructed in this program. The 200-scfm faceplate was constructed for backup to be used in the event that the 120-scfm faceplates were burned. Increasing the Rigimesh permeability increases the gaseous hydrogen transpiration coolant flow (figure 69), and the tolerable heat flux (figure 70).

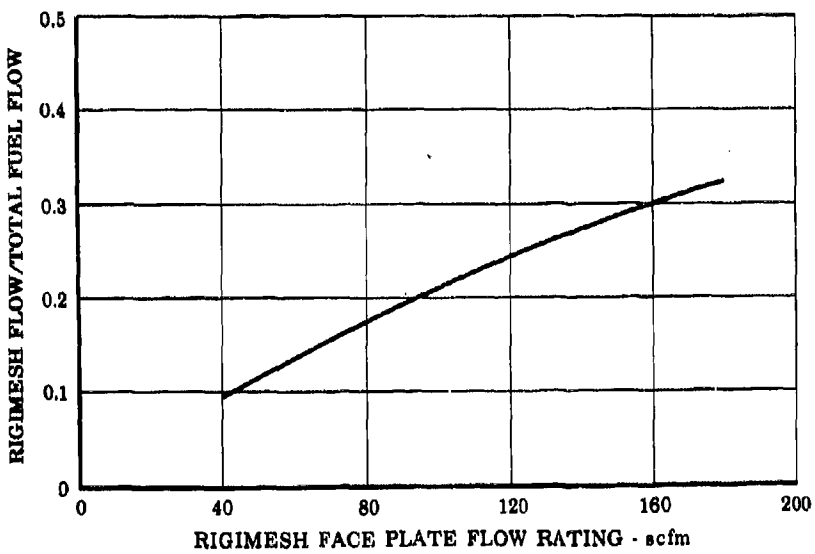

Figure 69. Effect of Rigimesh Face Temperature on Rigimesh Flow FD 14890

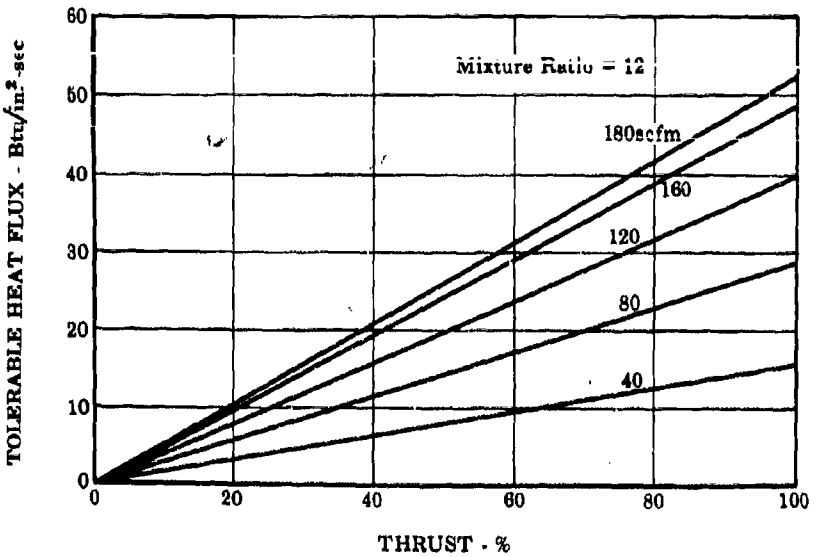

Figure 70. Injector Face Cooling Capacity at Various Rigimesh Permeabilities FD 14891

(C) For maximum thrust conditions, the injector face heat flux that can be tolerated by increasing the Rigimesh permeability is illustrated in figure 71. The tolerable heat flux diminishes with increasing mixture ratio because the total fuel flow (and thus the flow through the Rigimesh) decreases. In the test at 824 psia chamber pressure, the center of the 40-scfm faceplate was burned away at a mixture ratio of approximately 8. Therefore, the heat flux to the center of face must have been at least 22 Btu/in.²-sec and was probably higher. A 120-scfm permeability rating was selected for the 8.5K injector to provide adequate face cooling margin at mixture ratios to 12.

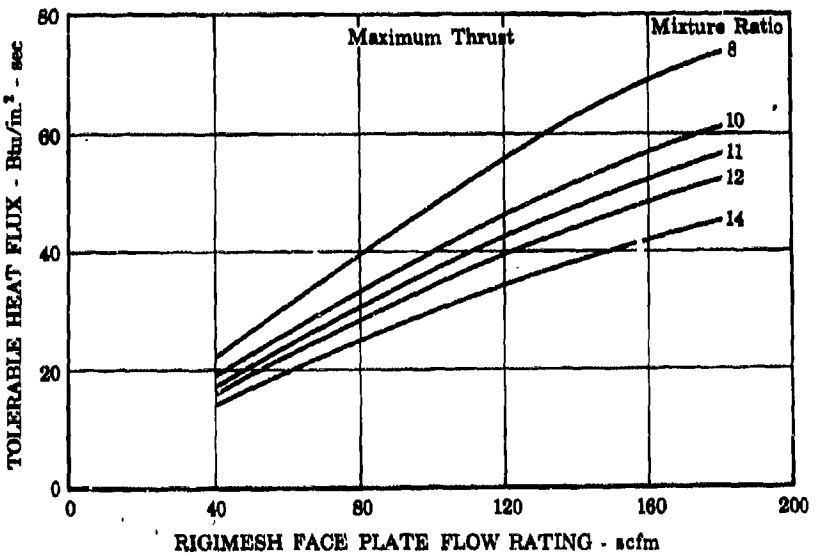

Figure 71. Tolerable Heat Flux vs Rigimesh Permeability for Maximum Thrust Conditions FD 14882

(U) The original 40-scfm faceplates as well as the new 120-scfm and 200-scfm Rigimesh faceplates were made from N-155 Multimet, an iron-cobalt-chromium-nickel alloy. This alloy was selected because it has been used successfully in RL10 injectors using both O_2/H_2 and F_2/H_2 propellants. TD nickel, which is pure nickel strengthened by 2% thorium oxide (ThO_2) is considered to be a superior material but because of price and delivery (26 weeks) it was not used in this program. TD nickel has three very desirable properties: (1) good fluorine resistance, (2) high thermal conductivity, and (3) good strength at elevated temperatures. Figure 72 compares the thermal conductivity and strength of TD nickel with that for the N-155 alloy.

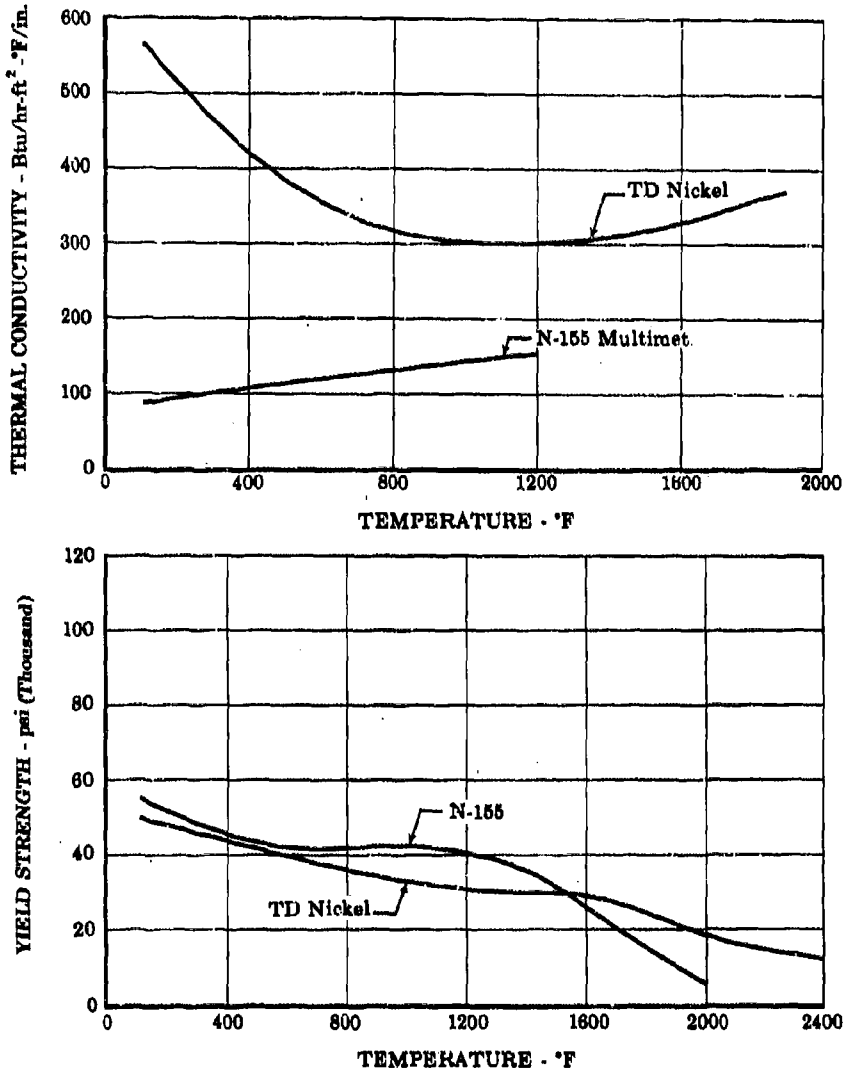

Figure 72. Comparison of Strength and Thermal Conductivity for Rigimesh Materials FD 14962

e. Injector Calibration

(U) The injector was calibrated to determine the effective flow areas of (1) the oxidizer primary injector, (2) the secondary injectors, (3) the fuel injector, and (4) the Rigimesh faceplate. The effective flow areas were used in the combustion tests to calculate injection velocities from measured values of injector pressure drop. Water was used to calibrate the oxidizer injectors, and gaseous nitrogen was used to calibrate the fuel injector and Rigimesh.

(U) The results of the calibrations are given in table XIII. These flow areas were obtained by use of measurements of flow rate and the injector pressure drops.

(C) Table XIII. Injector Flow Areas and Discharge Coefficients (AC_d and C_d)

	AC_d, $in.^2$	C_d
Oxidizer primary injector	0.01883 [0.0188]	0.924 [0.922]
Oxidizer secondary injector	0.2455 [0.244]	0.629 [0.626]
Fuel injector	0.651 [0.493]	- -
Fuel Rigimesh	0.240 [0.092]	- -
Rigimesh holes	0.411 [0.401]	0.939 [0.922]

Rigimesh calibration was accomplished by inserting O-rings around each secondary spud to prevent flow through the fuel annular orifices. The numbers in brackets are values determined in Contract AF 04(611)-9965 calibrations. There is excellent agreement between the two sets of values for the oxidizer primary and secondary injectors. The fuel Rigimesh effective area was increased by a factor of 2.7 because of the change in permeability from 40 to 120 scfm. The total fuel injector AC_d increased correspondingly. The Rigimesh holes AC_d increased because four coolant holes were added at the center of the injector.

2. Sea Level Chambers

(U) The sea level chambers designed, fabricated, and tested with the 8.5K injector under Contract AF 04(611)-9965 were used in the altitude tests. Two chambers were available from the previous contract. The chambers, illustrated in figure 73, have a 7.5-inch chamber diameter, a 2.835-inch throat diameter, a chamber L* of 55 inches, and an expansion ratio of 4.2. The chamber has a sharp corner throat; the radius of curvature is 0.070-in. which is equal to 0.0494 times the throat radius. A sharp-corner throat was selected to facilitate drilling the coolant passages.

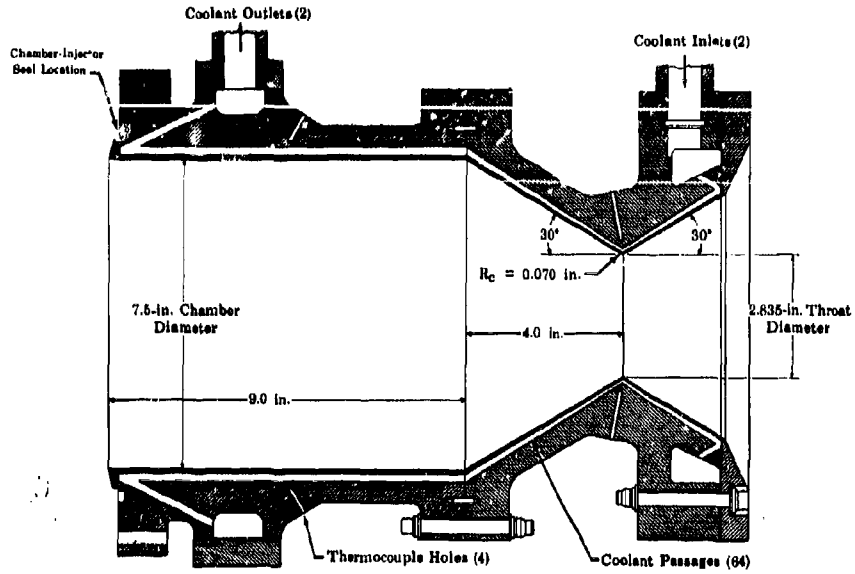

Figure 73. 8.5K Hydrogen Cooled Copper Chamber FD 12165B

(U) The chambers were constructed from copper. After the chamber and the nozzle sections were machined, they were silver-brazed together. During this operation, the stainless steel ring that forms the outer wall of the coolant discharge manifold and the copper end plate that forms part of the inlet manifold were also silver-brazed to the assembly. The braze prevented coolant leaks into the chamber or overboard. Bolts were used to resist the pressure force tending to separate the nozzle from the chamber and also to hold the nozzle end plate in position. The chamber assembly was hydrostatically tested to 2000 psia and helium leak-checked as the final fabrication step. No leaks were detected.

(U) The chamber was cooled by hydrogen gas flowing through 64 drilled holes in the chamber and nozzle sections. In the chamber, the holes had a constant 0.1925-inch diameter and were located so that there was a 0.100-inch wall thickness. The coolant holes were tapered from both ends of the nozzle section. At the nozzle throat, the passage diameter was 0.090 inch and had a 0.035-inch wall thickness.

(U) Because nickel is more resistant to fluorine than copper, the chamber inside surfaces were plated with nickel to approximately a 0.020-inch thickness.

(U) To attach the copper chamber to the nozzle extension, the chamber end plate was machined down so that it was flat and thin enough to be cooled by the gaseous hydrogen in the inlet chamber manifold.

3. Nozzle Extensions

(U) Two nozzle extensions like that shown in figure 74 were constructed for the altitude tests. The nozzle extensions were made from RL10 rocket

engine thrust chambers. The divergent part of the nozzle was cut from the RL10 thrust chamber and fitted with a coolant manifold and adapter section so that it could be attached to the 8.5K sea level chamber as shown in figure 75. The 30-degree conical divergent section of the sea level nozzle was mated to the nozzle extension to provide a smooth contour (figure 76) that approximated an ideal contour calculated for maximum shifting equilibrium performance and for an 180-to-1 expansion ratio.

(U) Not only did nozzle extensions constructed from RL10 thrust chambers provide a near-ideal contour but also, because of the tubular wall RL10 chamber construction, the nozzle extension could be convectively cooled with gaseous hydrogen, thus permitting extended duration tests. In addition, because the altitude system diffuser is designed for RL10 engine tests, the nozzle extension was mated easily to the diffuser using a proven seal.

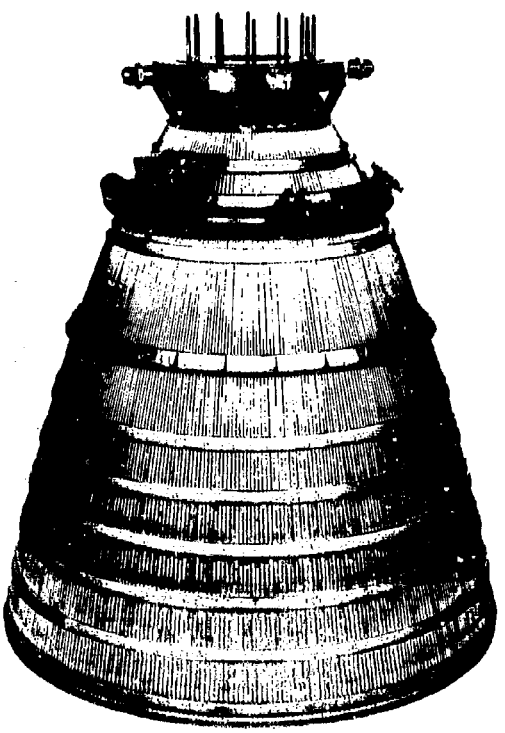

Figure 74. Nozzle Extension FE 63196

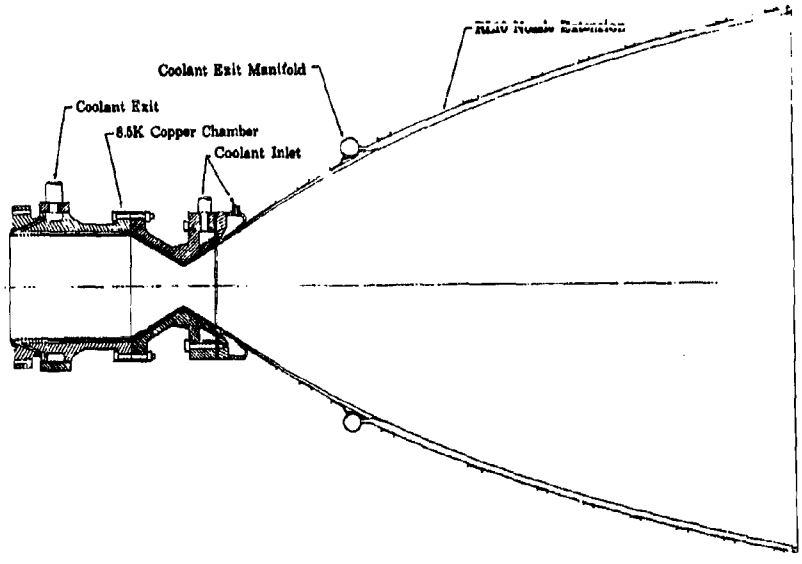

Figure 75. 8.5K Sea Level Chamber With RL10 Nozzle Extension FD 13324

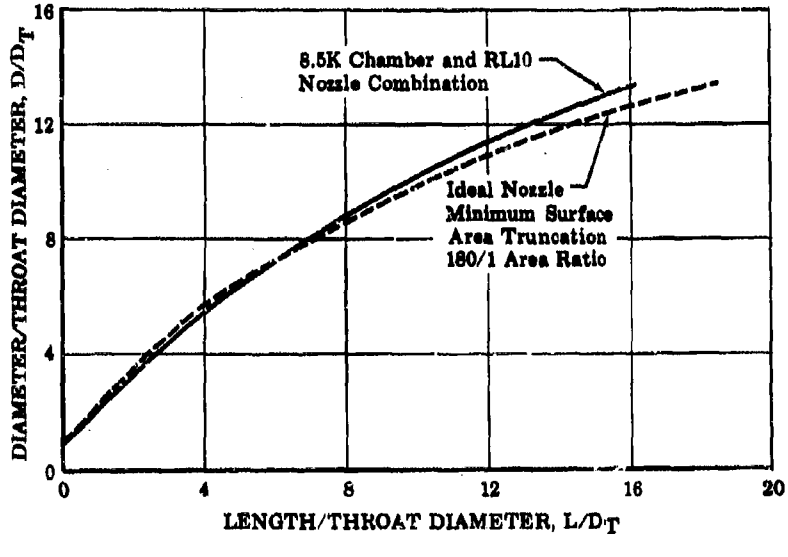

Figure 76. Comparison of Nozzle Contours (8.5K-RL10 Nozzle Combination With Ideal) FD 14892A

(U) After the chamber was severed, an inlet manifold for the GH_2 coolant and attachment plate was installed at the forward end of the nozzle extension. Manifold installation on the nozzle divergent section was accomplished by forming the tubes on the inside diameter of the nozzle at the cut to permit installation of the manifold while retaining a smooth nozzle contour. The manifold was then brazed to the nozzle by means of an attachment plate. Pressure forces were carried by straps from the manifold to the nozzle.

(U) During the design of the nozzle extension, a heat transfer analysis was made. It was found that the part of the extension most difficult to cool is the adapter (figure 77) that connects the RL10 coolant tubes to a new coolant manifold. This adapter was fabricated from nickel because of its high thermal conductivity. In addition, to enhance the cooling of the adapter, silver was cast and then machined to form the inner surface of the coolant flow channel (figure 77). This silver fillet provided low thermal resistance between the exposed tip of the adapter and the coolant and maintained the coolant heat transfer coefficient at a satisfactory level. Figure 77 presents the computed temperatures for various locations in the adapter and surrounding parts. These temperatures were computed for maximum chamber pressure (850 psia) and, hence, the maximum heat flux condition. The highest temperature (2500°R), which occurs at the tip of the exposed nickel adapter, is below the melting point of nickel, and the other nozzle extension temperatures are low enough to provide adequate strength.

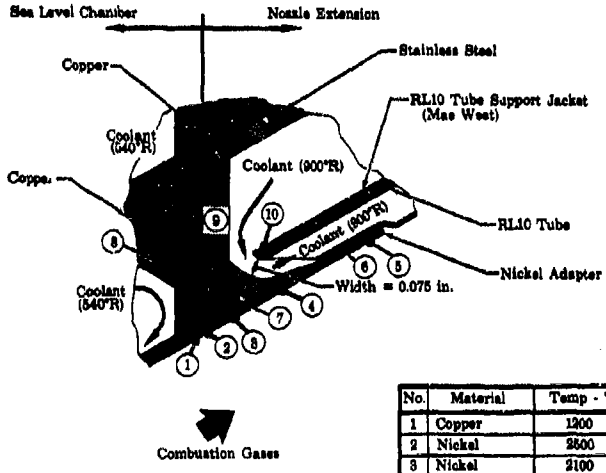

No.	Material	Temp - °R
1	Copper	1200
2	Nickel	2500
3	Nickel	2100
4	Nickel	1600
5	Nickel	1700
6	Silver Braze	1500
7	Silver	1550
8	Silver Braze	1500
9	347 SST	1000
10	347 SST	900

Figure 77. Nickel Adapter for 8.5K Nozzle Extension FD 20835

(U) Minor fabrication problems were encountered with the first nozzle extension. The first problem was encountered during the casting of the silver into the first two nickel adapters (figure 77). Voids occurred in the silver during casting, which would reduce the heat transfer through the silver and ultimately result in burnout of the adapter. Attempts to repair the adapters resulted in cracks in the nickel. During the initial attempt at making the silver fillet, pieces of silver were placed around a ring and then melted to form the fillet. For subsequent rings, molten silver was poured into the ring while it was in a hydrogen-atmosphere furnace. This procedure proved to be satisfactory, as indicated by X-rays that showed the silver to be void-free. The nickel ring was cleaned by the hydrogen environment prior to the introduction of the silver, thus avoiding the possibility of void-causing impurities.

(U) A second problem area developed when the nickel adapter was being brazed to the cut-off RL10 chamber. The tooling that was used initially to hold the ring in place was too massive and as a result it absorbed excessive heat from the RL10 tube support jacket during the brazing operation. The tooling was in direct contact with the RL10 tube support jacket and consequently to the tubes to which the adapter was being brazed. To bring the tubes to an adequate brazing temperature it would have been necessary to concentrate additional heat in the tube area, thereby endangering the existing braze between the chamber tubing and the cast silver in the adapter. The problem was solved by using smaller tooling. Some shrinking and distortion of the ring occurred when it was brazed to the chamber, which resulted in a smaller-than-anticipated coolant passage opening. The design passage width of 0.075 inch (figure 77) was reduced and the width was not uniform but varied from 0.048 to 0.056 inch. These smaller widths were considered acceptable because it increased the hydrogen coolant velocity and therefore cooling of the ring at the expense of a higher pressure drop. Both extensions were completed without further difficulty.

(U) The nozzle extension was cooled by the gaseous hydrogen that cooled the copper chamber. The coolant counterflowed through the copper chamber and then was routed to the nozzle extension.

C. HARDWARE DURABILITY

1. General

(C) Exceptionally good hardware durability was demonstrated in the test program. The durability is particularly impressive when the wide range of pressures and heat fluxes that were covered and the extended test durations accomplished are considered. It should be recalled that 35-second tests were made at 850, 750, 600, 450 and 300 psia. In each test mixture ratios of 8 to 12 were evaluated. In the 850-psia test the throat heat flux was approximately 30 Btu/in^2 sec. At the low chamber pressures the test time accumulated in 8 tests was 827.4 seconds and the longest test was just over 3 minutes. Photographs and a discussion of hardware durability by component follow.

2. Injectors

(U) With the exception of minor face burning, there was no damage to any injector part. Figures 78 through 83 show front and back views of the injector parts after testing. There was no evidence of even a small fluorine reaction, and no spud burning. The parts looked exactly as they did prior to the test.

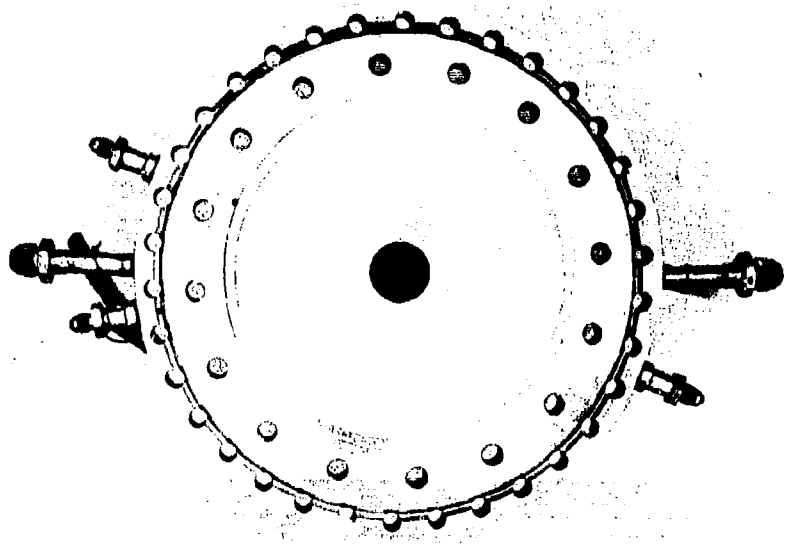

Figure 78. Front View of Injector Backplate After 15 Tests and 1032 Seconds Firing Time FE 68462

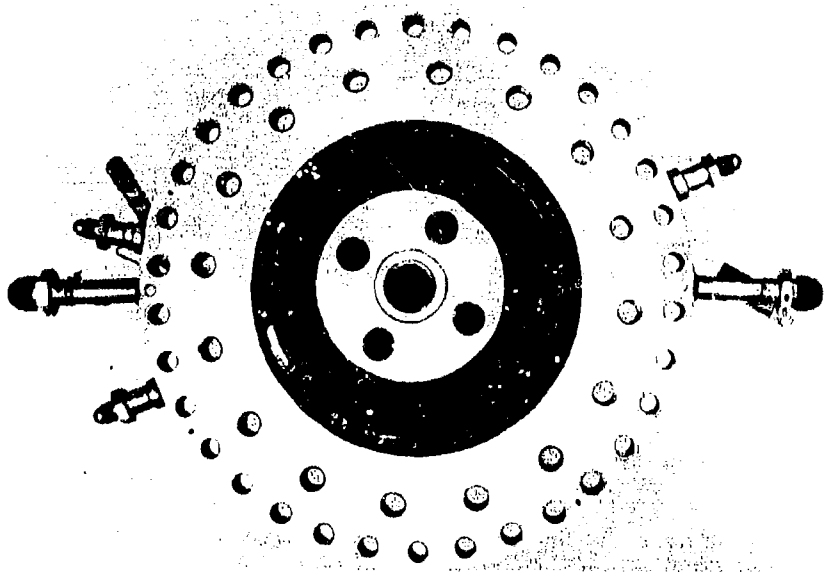

Figure 79. Back View of the Injector Backplate After 15 Tests and 1032 Seconds Firing Time FE 68461

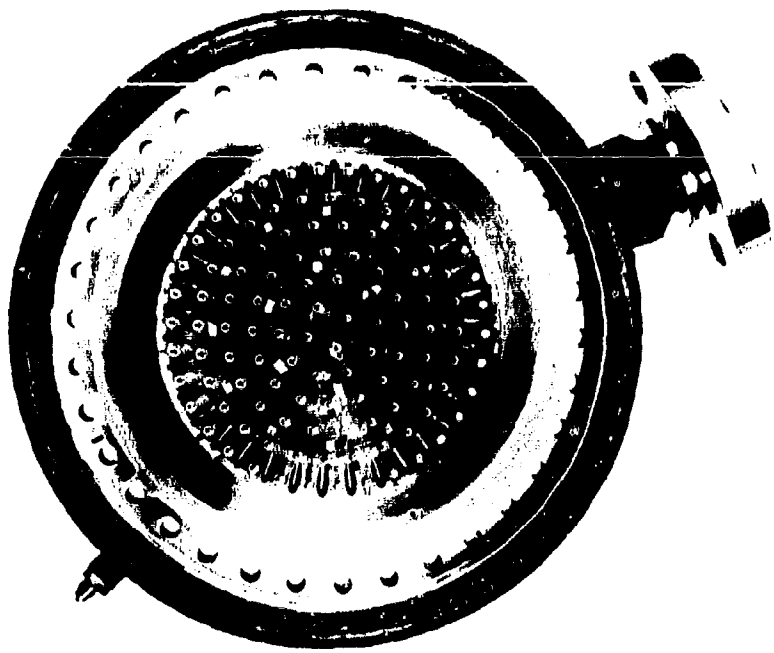

Figure 80. Front View of Fluorine Primary Injector FE 68464
Spudplate After 15 Tests and 1032 Seconds
Firing Time

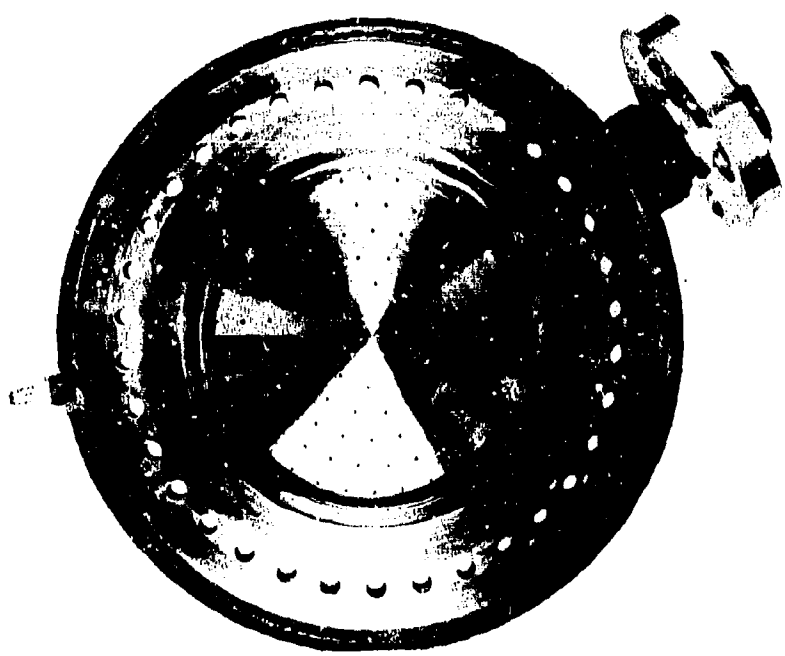

Figure 81. Back View of Fluorine Primary Injector FE 68463
Spudplate After 15 Tests and 1032 Seconds
Firing Time

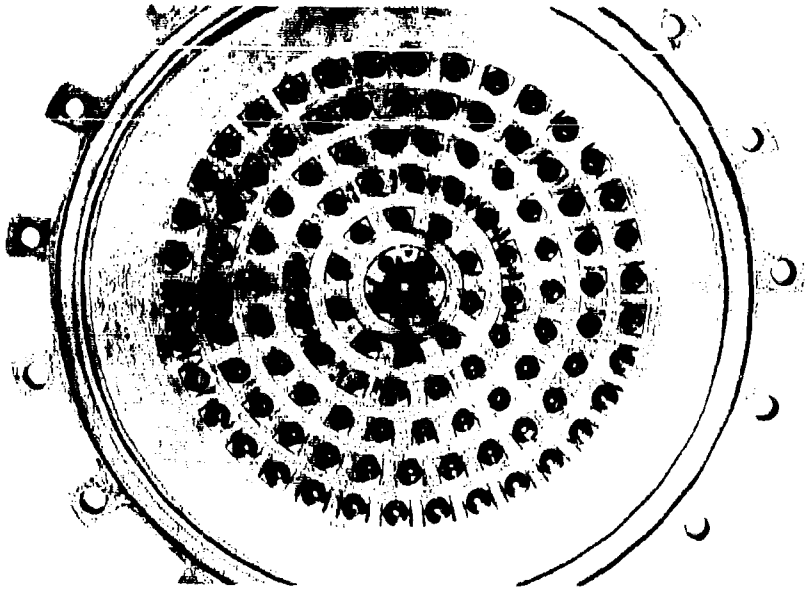

Figure 82. Front View of Fluorine Injector Spudplate After 15 Tests and 1032 Seconds Firing Time — FE 68466

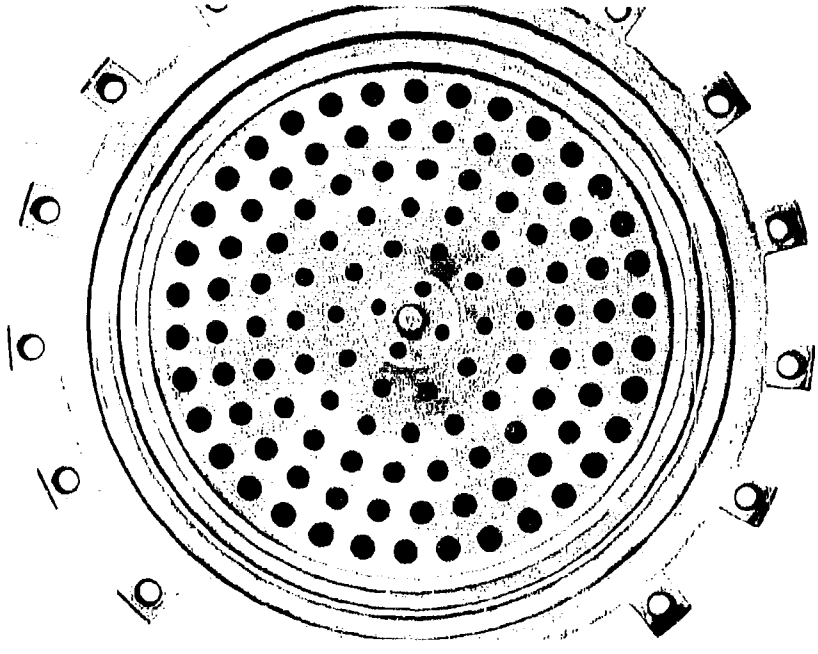

Figure 83. Back View of Fluorine Injector Spudplate After 15 Tests and 1032 Seconds Firing Time — FE 68465

(C) Some face burning occurred during the tests. The extent of this burning and steps taken to avoid it are discussed chronologically in this paragraph. One of the 120-scfm Rigimesh faceplates, which is designated faceplate No. 1, was used in the first three tests. Slight face burning occurred near the center of the injector. The burned area was repaired by chemical etching to restore permeability in the fused-over areas, and 78 0.020-inch diameter holes were added to both 120-scfm faceplates in the center portion of the injector to provide additional fuel injection in the region and thus to help break up recirculation of the combustion gases and to lower the mixture ratio. These holes can be seen in figure 84; because of their small size, fuel injection area is increased only 0.00245 in^2 or about 6%. The faceplate designated No. 2 was installed for the last 5 low-pressure tests. Additional burning at the center of the modified No. 2 injector faceplate occurred during shutdown of the 25-psia chamber pressure test. The shutdown sequence was therefore changed to provide for a longer hydrogen lag at shutdown since it appeared that the fluorine line was not completely purged when the hydrogen was shut off in test No. 4. No further burning was apparent for the remaining four low-pressure tests (No. 5 through 8). Figure 84 shows faceplate No. 2 after conclusion of low pressure tests.

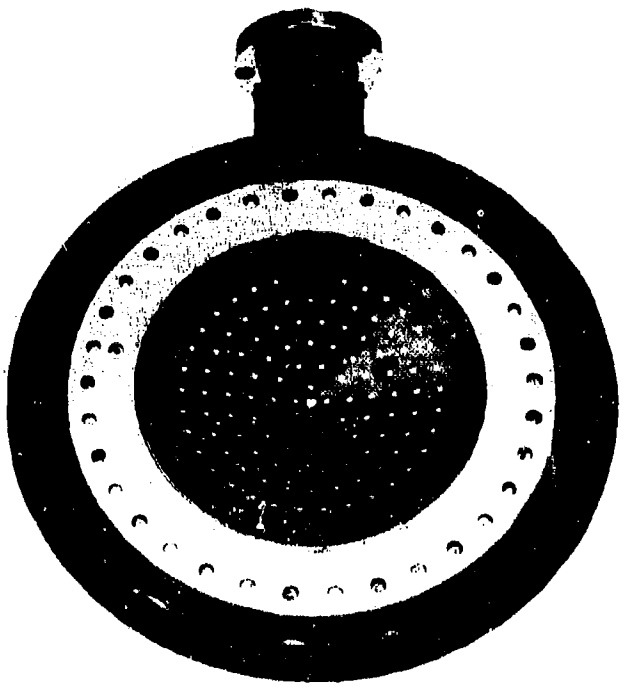

Figure 84. Injector Faceplate No. 2 After Test No. 8; Total Firing Time: 771 Seconds

FE 68624

(C) Faceplate No. 1, which was burned slightly in the first test at 30 psia, was used in the high-pressure tests. Slight additional face burning occurred during test No. 9 at a chamber pressure of 300 psia. Because this burning was believed to have occurred during startup, the initial valve set positions were changed to lower the starting mixture ratio. No additional burning occurred during the 450- and 600-psia chamber pressure tests. Faceplate No. 1 after the 600-psia chamber test is shown in figure 85. Because of the heat pattern between the third and fourth row of orifice holes, 44 additional 0.020-inch diameter holes were added between the rows. Also the orifice holes on the first two rows (the 14 center orifices) were enlarged from 0.126- to 0.136-inch diameter to reduce the mixture ratio in the center of the injector, thus supplementing injector face cooling. No additional face burning occurred during the final three tests at 300, 750, and 850 psia chamber pressures. Faceplate No. 1 after the high chamber pressure tests is shown in figure 86.

Figure 85. Injector Faceplate No. 1 After Test No. 11; Total Firing Time: 152 Seconds

FE 67526

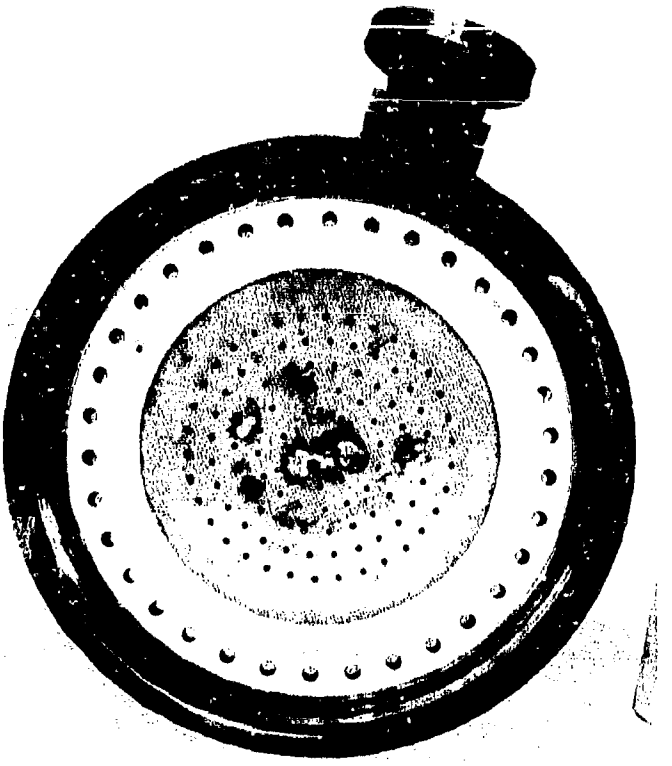

Figure 86. Injector Faceplate No. 1 After Test No. 15; Total Firing Time: 261 Seconds

FE 68467

3. Sea Level Chambers

(U) The copper workhorse sea level chamber demonstrated excellent durability. With the exception of the very minor heat marks at the injector end (shown in figure 87) the chamber showed no signs of damage. Figure 88 shows a view from the aft end of the chamber.

4. Nozzle Extensions

(C) One nozzle extension was successfully used for all low pressure tests and the first two high chamber pressure tests at 300 and 450 psia chamber pressures. During the next test, at 600 psia chamber pressure, some of the hydrogen coolant leaked behind the nozzle extension tubes and into a small gap between the tubular wall and the Mae West of the RL10 chamber. This leakage resulted in a pressure in this region sufficiently high to push several of the tubes away from the Mae West and destroy the smooth

nozzle contour (figure 89). The braze coverage between the tubes and the Mae West was insufficient to withstand the pressure forces. The nozzle extension was replaced with the backup extension and a vent was provided to prevent pressure buildup behind the tubular wall. Cold flow tests with the vent indicated that the leakage was small and therefore would not affect cooling of the nozzle extension.

(C) The second nozzle extension was used for the last three tests, which were made at chamber pressures of 300, 750, and 850 psia, respectively. The nozzle extension looked good after the 300-psia tests. However in the 750-psia test several of the coolant tubes were blown out in the nozzle extension, as shown in figures 90 and 91. The first figure is a view through the small diameter that mates to the copper chamber. These burnouts are attributed to the fact that the coolant fuel flow dropped off, apparently to an unacceptable value, in the 750-psia chamber pressure test. Because of insufficient coolant flow in these tubes they became overheated and the coolant pressure ruptured them.

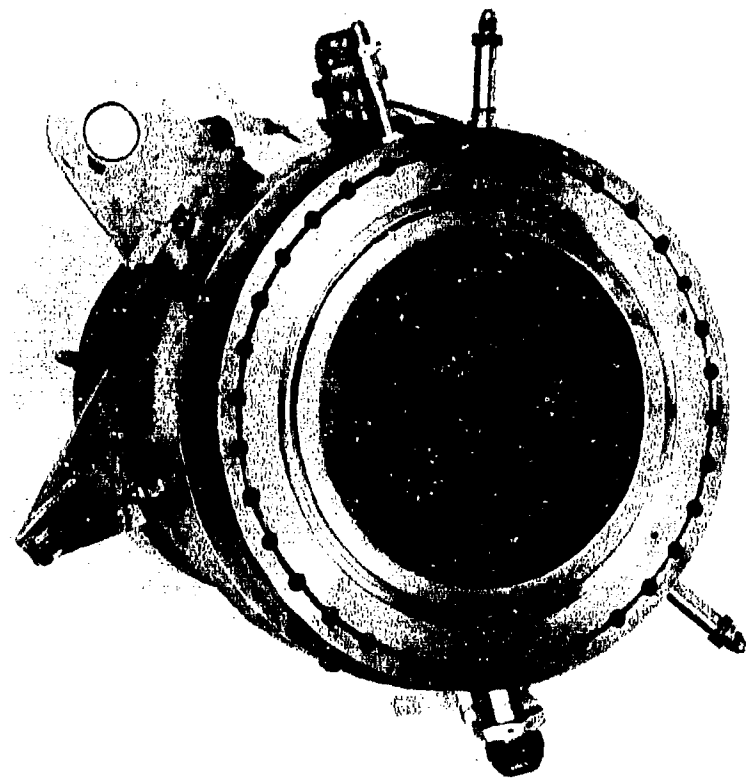

Figure 87. Chamber View of Sea Level Chamber After 15 Tests and 1032 Seconds Firing Time FE 68470

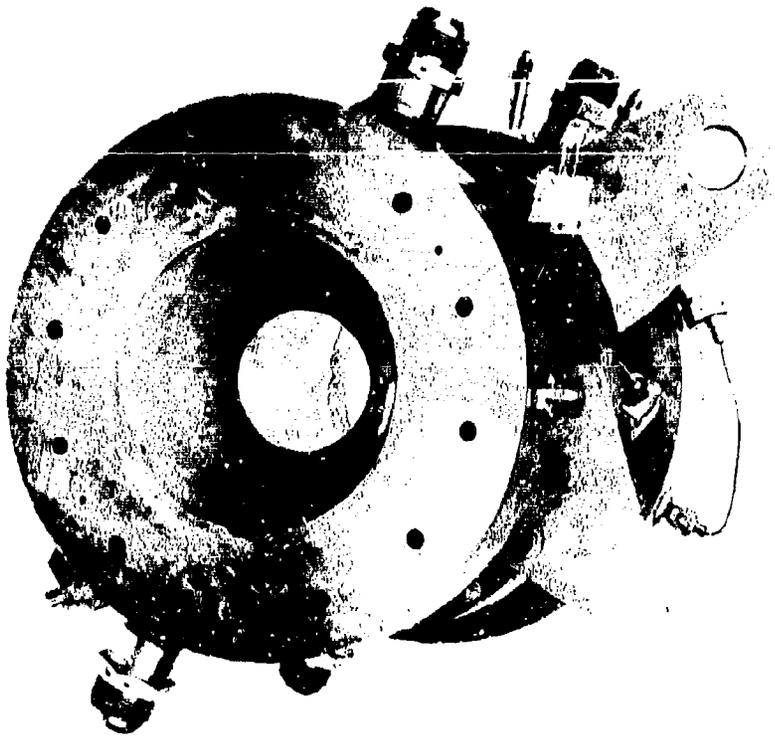

Figure 88. Nozzle View of Sea Level Chamber After 15 Tests and 1032 Seconds Firing Time

FE 68469

Figure 89. Nozzle Extension

FE 68554

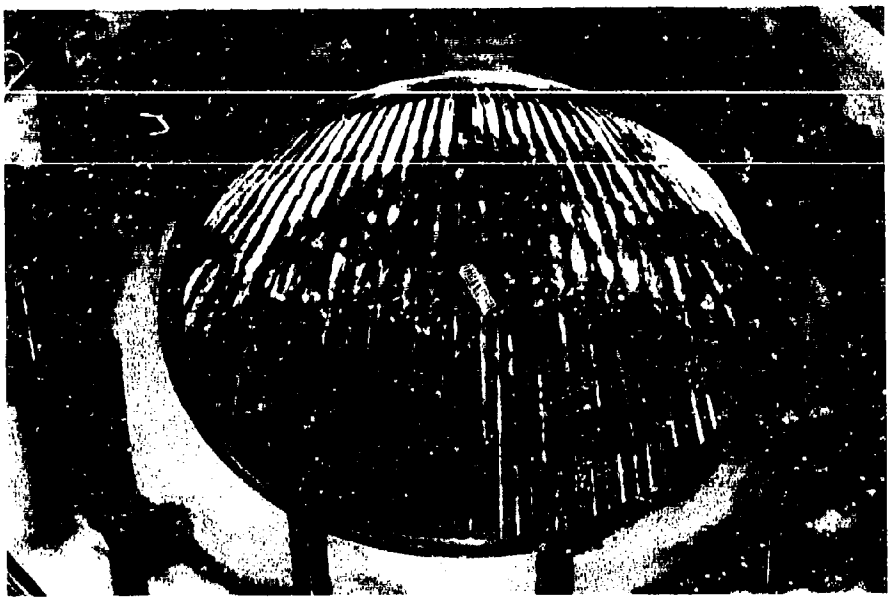

Figure 90. View From Chamber End of Nozzle Extension No. 2 After Test No. 15; Total Firing Time: 109 Seconds FE 68471

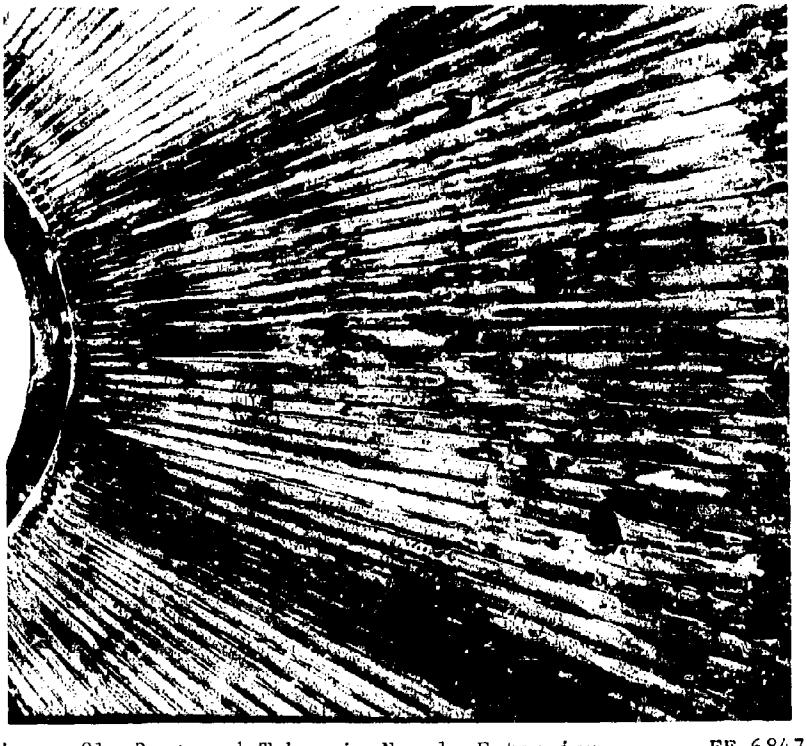

Figure 91. Ruptured Tubes in Nozzle Extension No. 2 After Test No. 15; Total Firing Time: 109 Seconds FE 68472

SECTION VI
TEST FACILITIES

A. GENERAL

(U) The 8.5K fluorine/hydrogen combustion firing tests made under this contract were accomplished on B-29 test stand, which is a part of the Liquid Propellant Research Facility (LPRF) at FRDC. Pressure-fed thrust chambers in the 500- to 50,000-lb thrust range can be test-fired in the LPRF with cryogenic or storable propellants. This facility was used in the 1K and 8.5K thrust fluorine/hydrogen dual-orifice injector tests under Contract AF 04(611)-9965. An overall view of the Liquid Propellant Research Facility, showing the ejector and scrubber of the altitude system, is shown in figure 92; a schematic diagram of the facility layout is given in figure 93.

(U) The FRDC continuous-exhausting steam-driven altitude simulation system is aerodynamically similar to the ejector systems that have been used successfully in the RL10 rocket engine test area at FRDC. In addition, however, the Liquid Propellant Research Facility is capable of handling fluorine combustion products. The LPRF system consists of diffusers, water-cooled ducting, a heat exchanger to reduce the temperature (and hence the volume of exhaust products before they enter the steam ejectors), two steam ejectors, a water scrubber for the effluent gases, and neutralization provisions for the liquid discharge from the scrubber. The diffuser dimensions are given in figure 94.

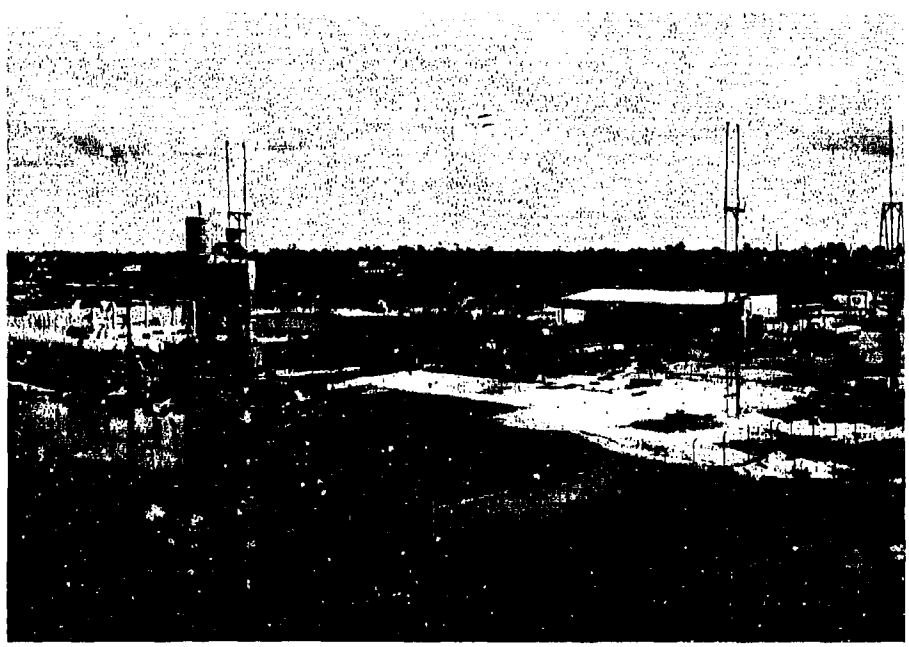

Figure 92. Overall View of the Liquid Propellant Test Facility FC 12397

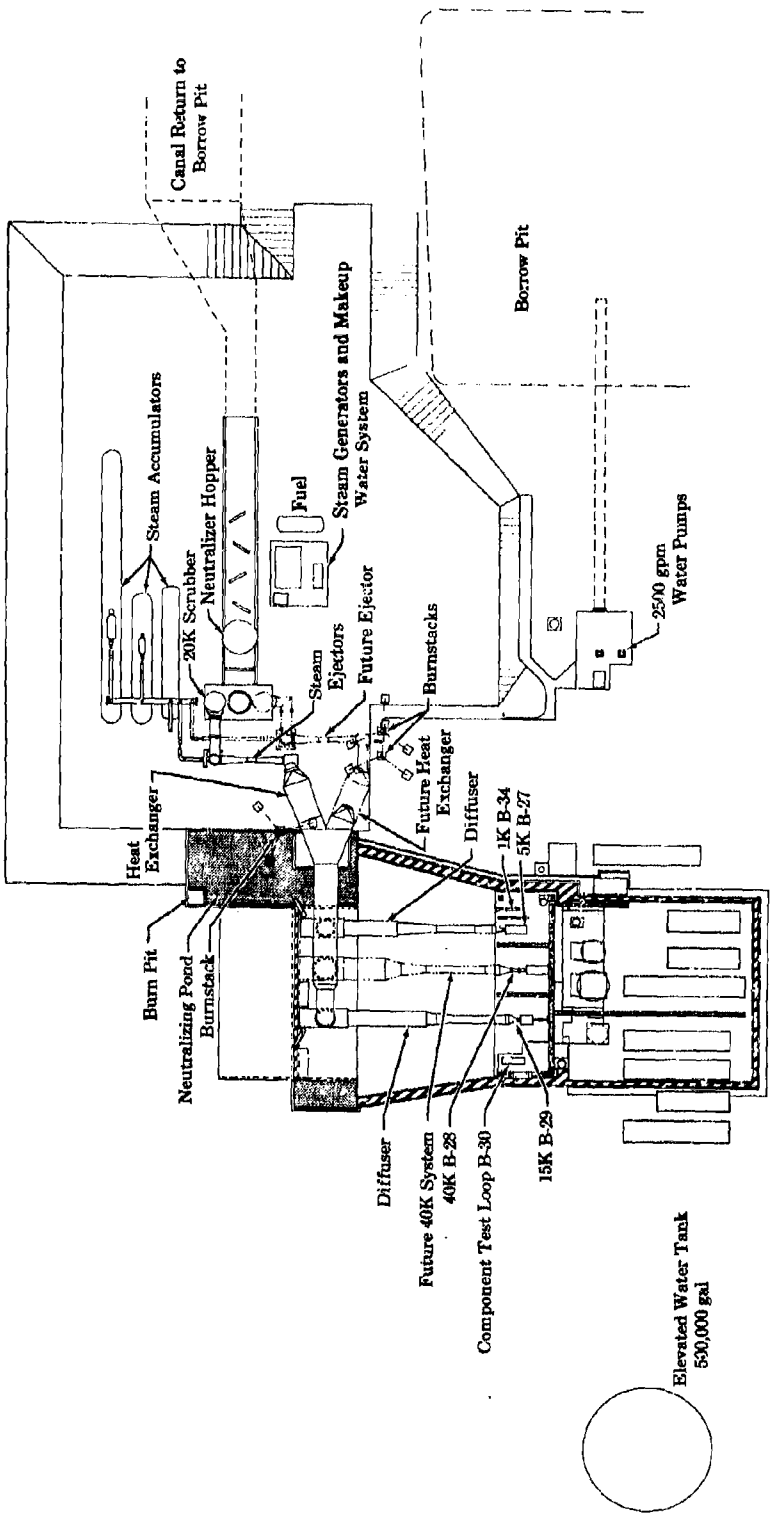

FD 12808

Figure 93. Liquid Propellant Test Facility Layout

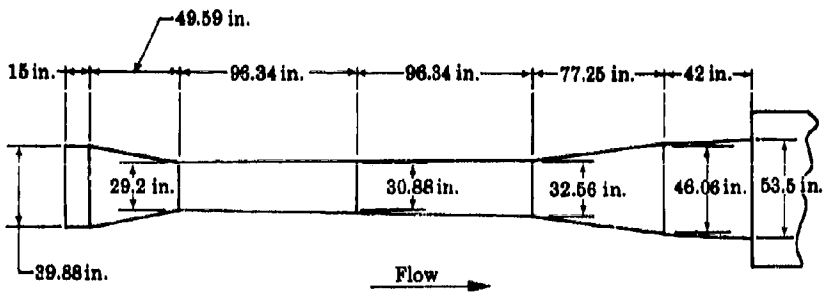

Figure 94. Diffuser Dimensions FD 20967

(U) The total steam accumulator capacity is 47,500 gallons. Prior to a test the accumulators are pressurized to approximately 250 psia. With this accumulator capacity, tests of approximately 200-sec duration can be made. This large capacity, in conjunction with the water-cooled ducting and the heat exchanger, permits continuous operation of the steam ejection system so that extended duration tests can be conducted at any desired chamber pressure.

(C) The capability of the LPRF altitude system is illustrated in figure 95. The lower curve represents, as a function of total engine propellant flow, the diffuser discharge pressure that was maintained by the ejector system in the 8.5K altitude tests. The unity area ratio curve in figure 95 represents the required capacity for choking the 8.5K sea level nozzle. The 180-to-1 area ratio curve is that for the 8.5K chamber, RL10 nozzle extension assembly. Figure 95 shows that the ejector has sufficient capacity (1) to choke the nozzle throughout the thrust range and (2) to flow-full the 180-to-1 area ratio nozzle down to approximately 30% thrust (250 psia chamber pressure). Consequently, although nozzle separation did occur in the low chamber pressure tests, the nozzle throat was still choked and thus c* efficiency could be determined accurately by chamber pressure measurements over the entire 5-to-850 psia chamber pressure range.

(C) A good indicator of nozzle separation is the nozzle exit pressure or the half-shell pressure measurements. Figure 96 presents the measured half-shell pressure measurements as a function of chamber pressure. Also shown in this figure is the estimated maximum exit pressure that can be tolerated with an unseparated, flowing-full nozzle that was calculated based on FRDC cold flow nozzle separation data (figure 97). At pressures above this limit, the nozzle will separate. The data of figure 96 show that the nozzle was flowing full in all of the high pressure tests at chamber pressures from 300 to 850 psia.

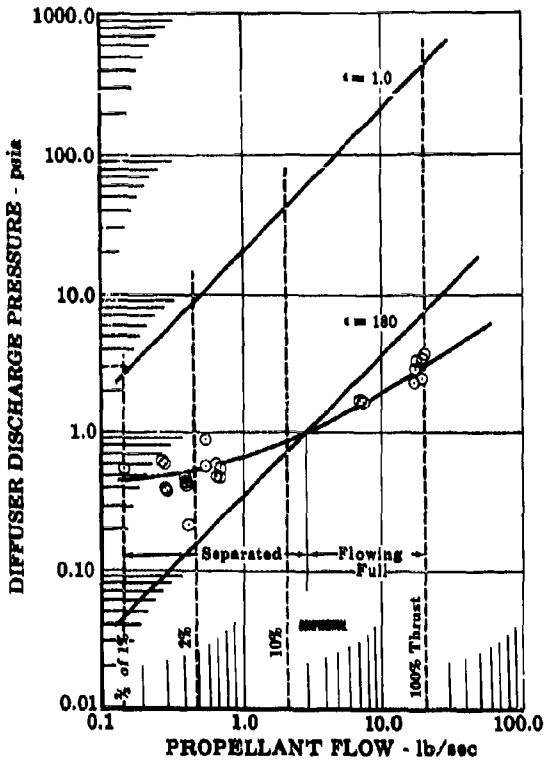

Figure 95. LPRF Altitude Simulating Exhaust System Capacity FD 20987

B. TEST SETUP

1. General

(U)In the 8.5K tests, fluorine was pressure-fed to the dual-orifice injector from a 300-gal liquid-nitrogen-jacketed supply tank using helium as the pressurant. Ambient temperature hydrogen gas for chamber cooling and the injector was supplied from a 1300-gal (173-ft^3) tank, wherein the pressure was controlled to approximately 2000 psia. Hydrogen was supplied to this tank from two 1496-gal (200-ft^3) tube trailers initally pressurized to 5000 psi. With these propellant supply systems, tests with durations to 35 seconds were accomplished in the high-chamber-pressure tests. In the low-pressure tests, test durations were increased to approximately the 200-sec limit imposed by the steam accumulators supplying the steam ejectors. The low-chamber-pressure tests were terminated when data were obtained at all programed mixture ratio and flow split set points. The duration of the longest low-chamber-pressure test was 184 seconds.

(U) Nitrogen gas was used for purging the stand and injector. To minimize contamination of the injector and lines, a constant 5-psig standby purge was maintained on the engine when it was inactive. Both the fuel and oxidizer, which were vented from the run lines, were disposed of through separate propane burnstacks.

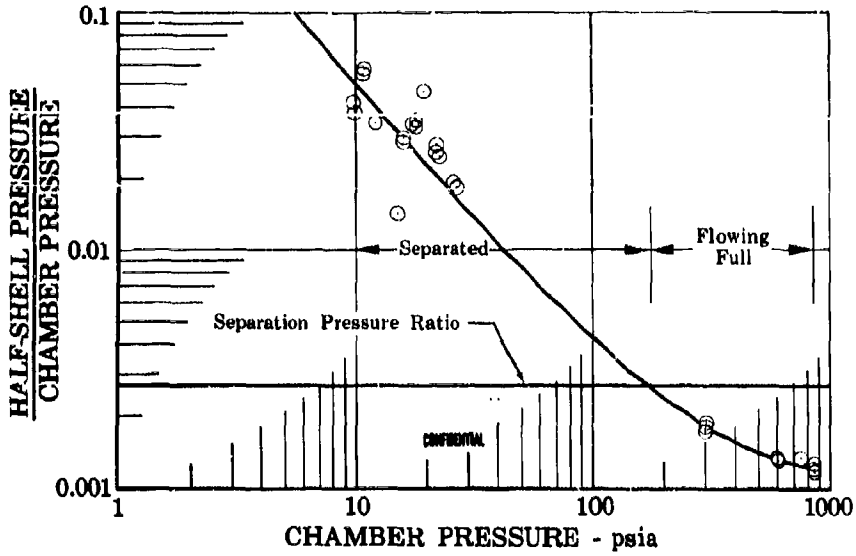

Figure 96. Ratio of Half-Shell Pressure to Chamber Pressure

FD 20964

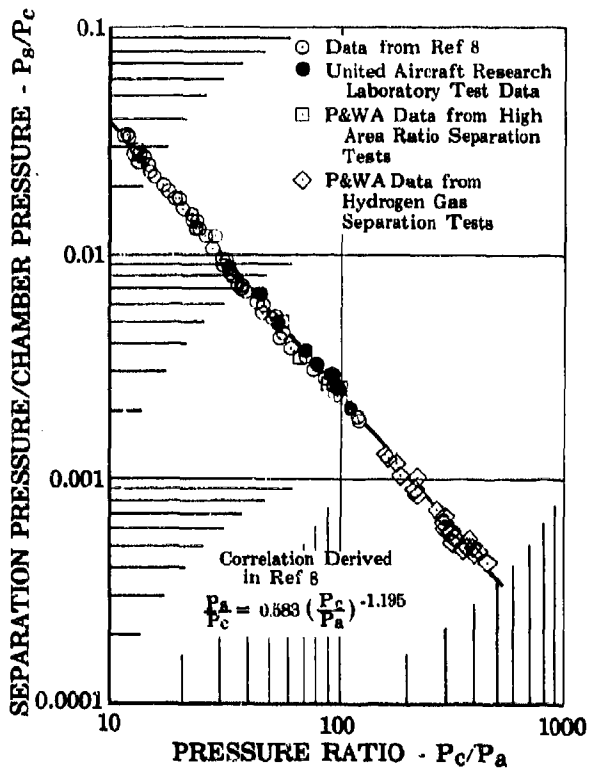

Figure 97. Separation Pressure Ratio of Short Contoured Nozzles

FD 20969

(U) Figures 98 and 99 show the engine installed in the test stand. Figure 98 was made from above the engine, looking down. The hydrogen inlet pipes are on the left. As indicated, the first pipe is the chamber coolant inlet supply line; the second pipe from the left is the injector hydrogen supply line; and the third pipe from the left is the coolant exit line. The hydrogen control valves are located behind the boiler plate wall. Figure 99 shows the south side of the installation. Shown are the fluorine control valve, CV 120; the fluorine flow divider valve, CV 130; and the nozzle extension coolant inlet control valve, CV 150.

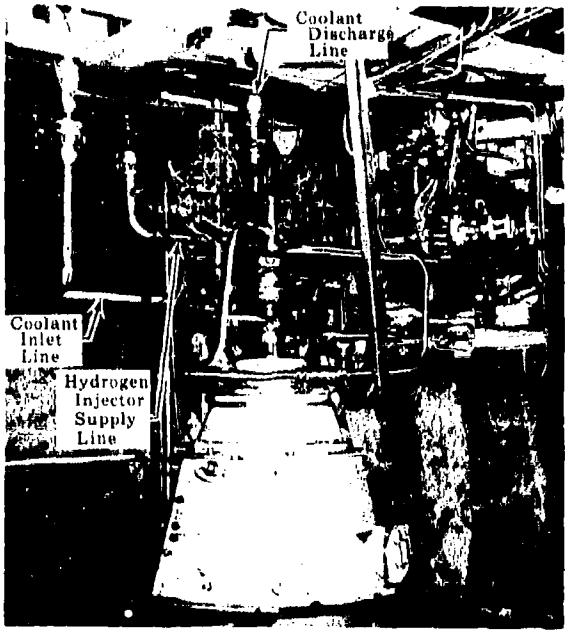

Figure 98. View Looking Down on 8.5K Altitude Engine Assembly FD 20990

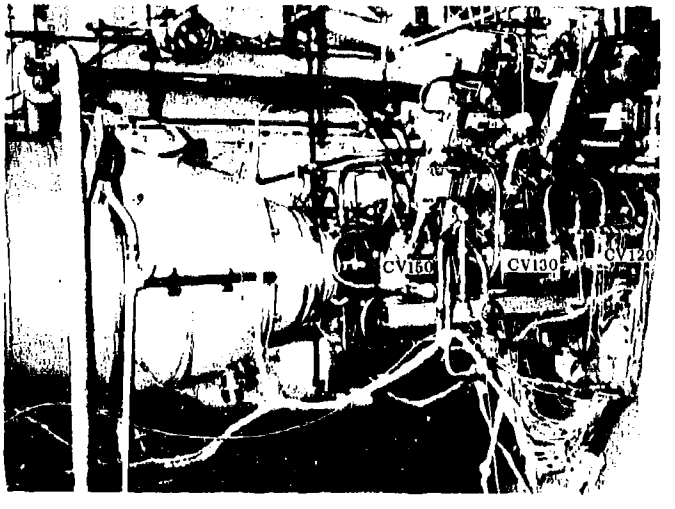

Figure 99. View of the West Side of 8.5K Altitude Engine Assembly FD 21503

2. Flow Control

(U) Propellant flow control was accomplished by electrohydraulically operated, plug-type valves. These valves were operated in a closed-loop control mode with both a 40-channel electronic event sequencer and a 48-amplifier analog computer providing the command signals. The sequencer supplied the step input commands; the analog computer supplied the transient ramp commands and the flow or pressure error signal commands. The electronic event sequencer, which is capable of timing any function to 1 millisecond, was also used to time-in (1) the automatic abort systems and (2) the start, shutdown, and purge sequences.

(U) The control valve setup is shown in figure 100. The valve CV 120 and its vernier valve, CV 320, are the fluorine flow control valves. Valve CV 100 and its vernier valve, CV 360, are the fuel flow control. Valve CV 130 is the fluorine flow divider valve. Valves CV 110 and CV 150 were used to control the sea-level-chamber-coolant-inlet pressure and nozzle-extension-inlet pressures, respectively. Valve CV 140 was used for coolant flow control.

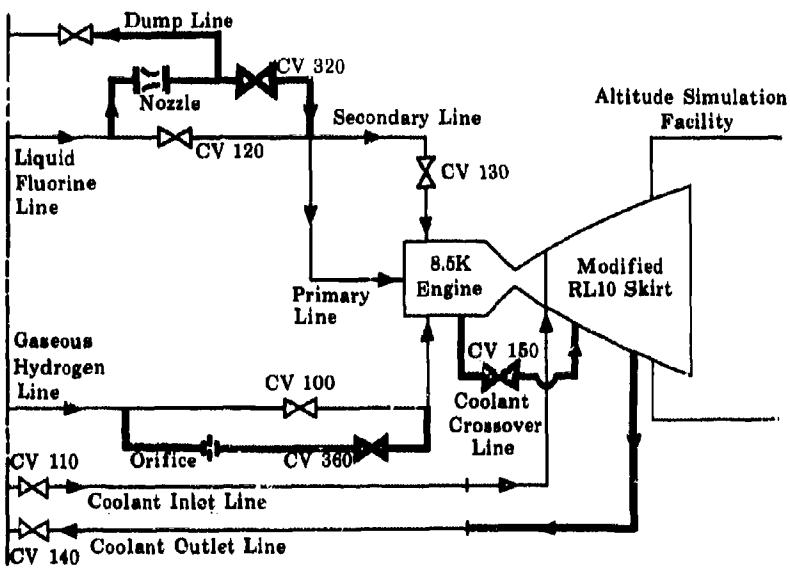

Figure 100. 8.5K Engine Piping Schematic for Altitude Tests FD 14885A

(C) The necessity of the vernier valves is illustrated in figures 101 and 102. Figure 101 presents the required control valve effective flow areas as a function of percentage thrust for fluorine flow control valve differential pressures of from 4 to 500 psid. Included in figure 101 are the operating ranges for valves CV 120 and CV 320. To ensure adequate flow control, a minimum pressure drop of approximately 100 psid should

be maintained across the fluorine control valve. Consequently, valve CV 120, although adequate for high thrust, would not be adequate below approximately 2% thrust (15 psia chamber pressure). Thus, valve CV 320 was used in the low chamber pressure tests (i.e., at chamber pressures from 5 to 30 psia) and CV 120 was used in the high chamber pressure tests.

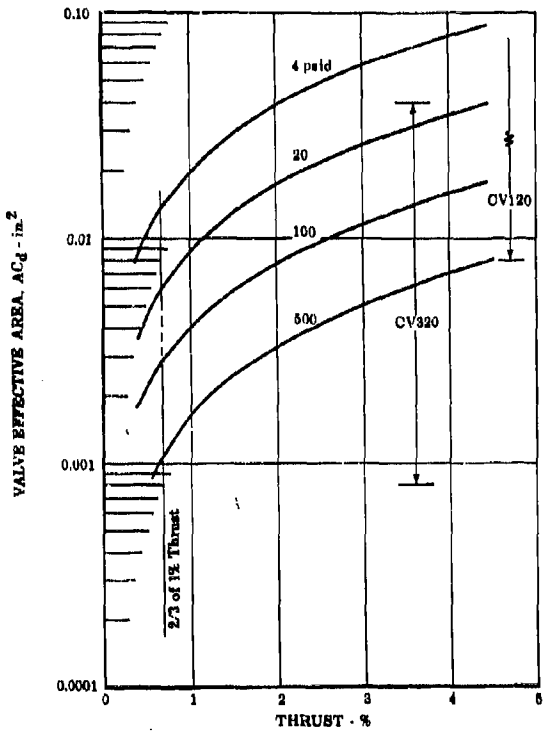

Figure 101. 8.5K Fluorine Flow Control Valve Requirements FD 14887

(C) Figure 102 presents similar information for the hydrogen flow control valves, CV 100 and CV 360. The required valve effective areas are given for several valve upstream pressures. The upstream pressure is equal to the hydrogen tank pressure, which is also the pressure that is supplied to the chamber coolant control valve. To keep the coolant flow rate at a sufficiently high level requires a tank pressure of at least 500 psia. Consequently, CV 100 is inadequate below approximately 1.7% thrust and therefore CV 360 was used at low chamber pressures.

(U) The control schematics for the high and low pressure tests are shown in figures 103 and 104, respectively. In the high-pressure tests the fluorine flow valve, CV 120, was operated in a closed-loop P_c control mode; the hydrogen flow control valve, CV 100, controlled mixture ratio; and the fluorine flow divider valve, CV 130, was in a position control mode. Mixture ratio excursions were made by changing the mixture ratio setpoints from 8 to 10 to 12 in steps.

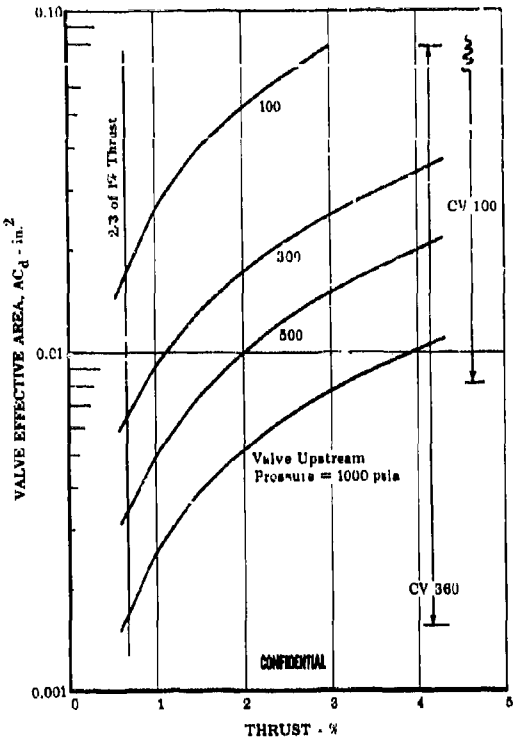

Figure 102. 8.5K Hydrogen Flow Control Valve Requirements FD 14888

(C) The chamber-pressure, mixture-ratio control modes were also initially used in the low-pressure tests. However, during test No. 3 at 30 psia it was found that because of the large line volumes downstream of the control valves, response was too slow and it took a long time to establish steady-state conditions at a given setpoint. Consequently, the control system was changed to a flow-mixture ratio control mode (figure 104) in all subsequent tests at chamber pressures of 25, 20, 15, 10, and 5 psia. In these tests valve CV 320 controlled fluorine flow and valve CV 360 controlled mixture ratio. As in the high-pressure tests, the fluorine flow divider valve was operated in a position control mode.

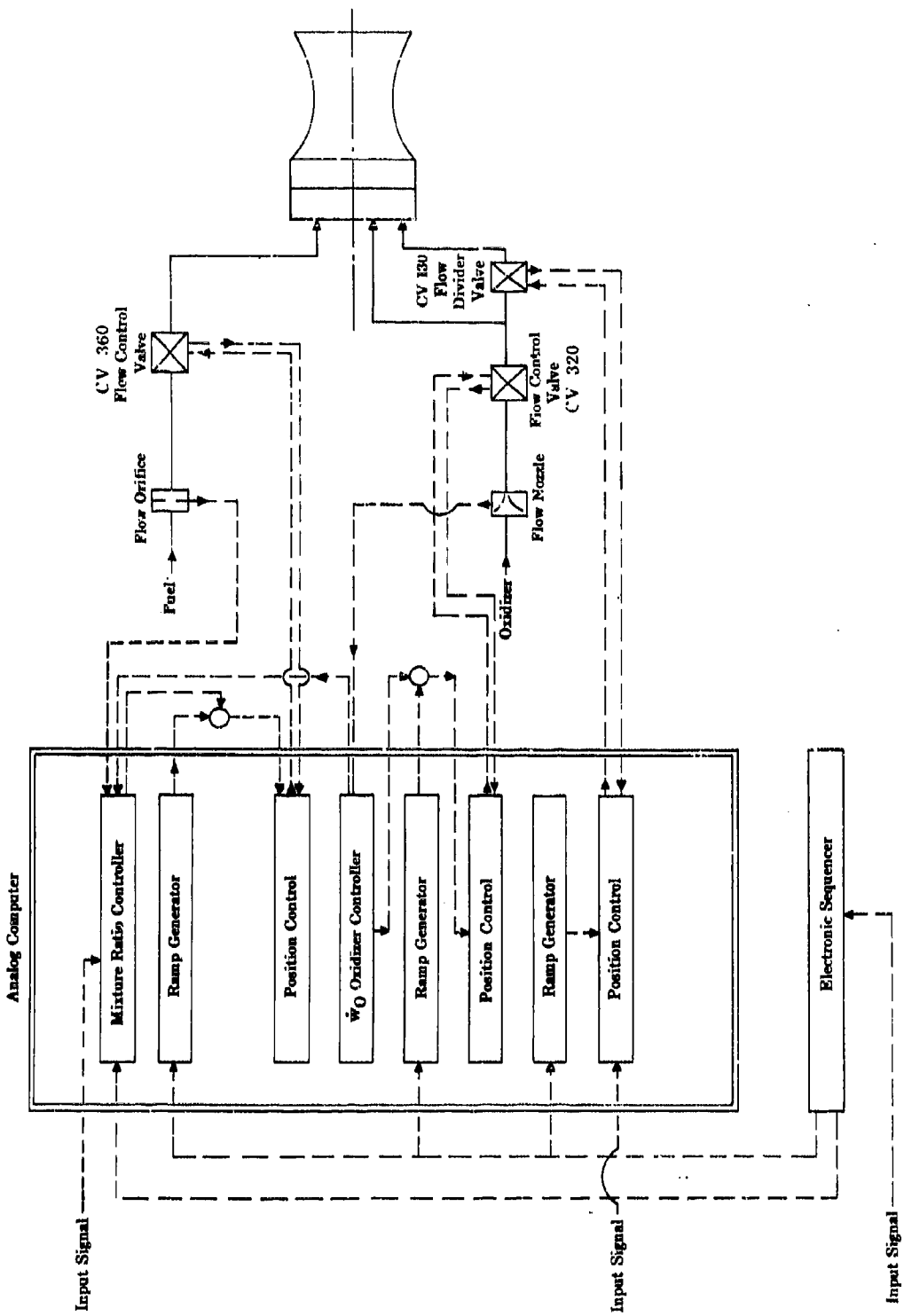

FD 13726A

Figure 103. 8.5K F_2/H_2 Control System Schematic - High Chamber Pressure Tests

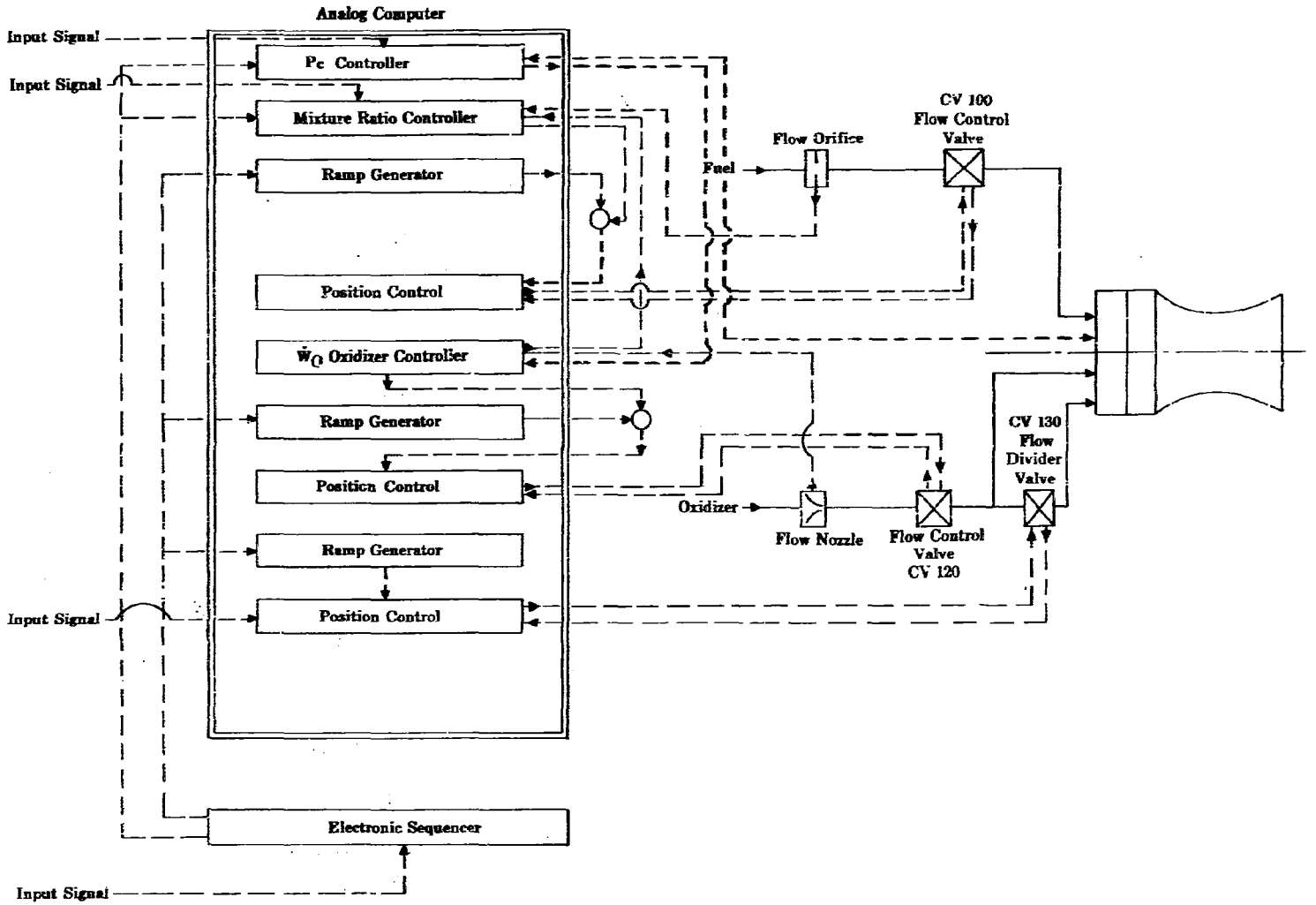

Figure 104. 8.5K F_2/H_2 Control System Schematic - Low Chamber Pressure Tests

FD 13726B

(U) Figure 105 illustrates the engine start sequence for the tests. Three ramp generators were used to control the rate at which the valves were opened. In the high-pressure tests, the fluorine and hydrogen flow control valves, CV 120 and CV 100, were stepped to open to predetermined low levels to provide a low mixture ratio start. Then after the lines and injector were filled as indicated by steady propellant flows, the control mode was changed and the valves were ramped open to follow a predetermined P_c ramp, during which the mixture ratio was controlled to 8. The ramp rate was constant for all tests and equal to 150 psi/sec.

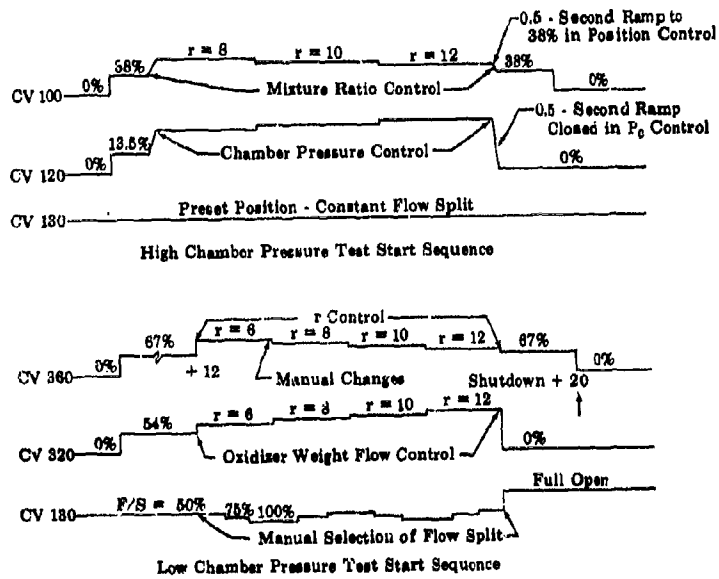

Figure 105. 8.5K Engine Start Sequence FD 20955

(U) In a similar manner in the low pressure tests, control valves CV 360 and CV 320 were stepped open to a predetermined low level. Then after the inlet lines and injector were filled, the control mode was changed to provide a constant-mixture ratio ramp to the setpoint pressure. The flow divider valve was on a position control mode; it was changed during the tests to achieve flow splits of 50, 75 and 100%. The mixture ratio setpoint was also changed stepwise during the tests to obtain data at four mixture ratios: 6, 8, 10 and 12.

3. Abort Systems

(U) Automatic abort systems were used to provide safeguards against hardware and test stand damage. An ignition detector burnwire, low- and high-chamber-pressure switches, high half-shell pressure switch, low chamber coolant weight flow, and fluorine leak-detector circuits were used in most tests. In addition, high oxidizer primary plate differential pressure, high fluorine secondary plate differential pressure, and high nozzle extension coolant inlet pressure were also used on the high-pressure tests to prevent overstressing hardware. A test was aborted unless the ignition burnwire parted and the chamber pressure rose above a preset value and remained above

that level after ignition. Other automatic abort systems were employed that protected against (1) a sequencer malfunction, (2) power failure, (3) loss of hydraulic pressure, and (4) GN_2 supply failure.

C. INSTRUMENTATION AND PERFORMANCE ERRORS

1. General

(U) Tables XIV and XV present the measurements taken for the high- and low-chamber-pressure tests. Test data were recorded by a 96-channel digital recording system, 36 oscillograph channels, and 12 strip charts. Measurements and errors of propellant flow rate, chamber pressure, and thrust are discussed in paragraphs 2, 3, and 4, respectively. Errors in characteristic exhaust velocity and specific impulse data are discussed in paragraphs 5 and 6.

(U) Table XIV. Instrumentation for High Chamber Pressure Tests

Pressures	Range, psia
Oxidizer Run Tank Supply Pressure	0-5000
Oxidizer Run Tank Pressure	0-2000
Oxidizer Nozzle Inlet Pressure	0-2000
Oxidizer Nozzle Differential Pressure	0-100
Oxidizer Nozzle Differential Pressure	0-100
Oxidizer Nozzle Differential Pressure	0-25
Oxidizer Nozzle Differential Pressure	0-25
Oxidizer Control Valve Pressure	0-2000
Oxidizer Divider Valve Pressure	0-1400
Oxidizer Primary Inlet Pressure	0-1400
Oxidizer Secondary Manifold Pressure	0-1400
Oxidizer Primary Injection Differential Pressure	0-500
Oxidizer Secondary Injection Differential Pressure	0-200
Oxidizer Primary Plate Differential Pressure	0-500
Oxidizer Secondary Plate Differential Pressure	0-500
Fuel Run Tank Supply Pressure	0-5000
Fuel Run Tank Pressure	0-3000
Fuel Orifice Inlet Pressure	0-3000
Fuel Orifice Differential Pressure	0-300
Fuel Orifice Differential Pressure	0-300
Fuel Orifice Differential Pressure	0-100
Fuel Orifice Differential Pressure	0-100
Fuel Control Valve Pressure	0-3000
Fuel Injector Manifold Pressure	0-2000
Fuel Injection Differential Pressure	0-200
Coolant Orifice Inlet Pressure	0-3000
Coolant Orifice Differential Pressure	0-150
Coolant Orifice Differential Pressure	0-150
Coolant Pressure Control Valve Pressure	0-3000
Coolant Jacket Inlet Pressure	0-3000
Coolant Jacket Exit Pressure	0-2000
Nozzle Extension Inlet Pressure	0-1500
Nozzle Extension Exit Pressure	0-1000

(U) Table XIV. Instrumentation for High Chamber Pressure Tests (Continued)

Chamber Pressure	0-1000
Chamber Pressure	0-500
Chamber Pressure	0-1000
Chamber Pressure	0-500
Seal Cavity Orifice Pressure	0-1400
Seal Cavity Pressure	0-1400
Half-Shell Pressure	0-15
Half-Shell Pressure	0-15
Half-Shell Pressure	0-15
Half-Shell Pressure	0-15
Mae West Discharge Pressure	0-1000
Mae West Orifice Differential Pressure	0-100
Temperatures	**Range, °R**
Oxidizer Nozzle Inlet Temperature	140-360
Oxidizer Nozzle Exit Temperature	140-360
Oxidizer Control Valve Temperature	140-360
CV 120 Body Temperature	140-540
CV 130 Body Temperature	140-540
Oxidizer Primary Inlet Temperature	140-360
Oxidizer Secondary Manifold Temperature	140-360
Fuel Orifice Inlet Temperature	460-600
Fuel Injector Manifold Temperature	460-600
Coolant Orifice Inlet Temperature	460-600
Coolant Jacket Inlet Temperature	460-600
Coolant Jacket Exit Temperature	500-1000
Nozzle Extension Inlet Temperature	500-1000
Nozzle Extension Exit Temperature	500-1500
Coolant Wall Chamber Temperature	500-1000
Coolant Wall Chamber Temperature	500-1000
Coolant Wall Throat Temperature	500-1000
Coolant Wall Throat Temperature	500-1000
Injector Coolant Exit Temperature	140-250
Run Line Jacket Vent Temperature	140-160
Oxidizer Sample Bottle Temperature	140-360
Mae West Discharge Temperature	500-1000
Miscellaneous	
CV 120 Position	0-100%
CV 130 Position	0-100%
CV 100 Position	0-100%
CV 140 Position	0-100%
CV 150 Position	0-100%
CV 110 Position	0-100%
Start Signal Voltage	
Prestart Signal Voltage	
Thrust	-9000
	+9000
Thrust	-9000
	+9000
Mixture Ratio	6-16
Coolant Weight Flow	0-3 lb/sec

(U) Table XV. Instrumentation for Low Chamber Pressure Tests

Pressures	Range, psia
Oxidizer Run Tank Supply Pressure	0-5000
Oxidizer Run Tank Pressure	0-2000
Oxidizer Nozzle Inlet Pressure	0-1000
Oxidizer Nozzle Differential Pressure	0-100
Oxidizer Nozzle Differential Pressure	0-100
Oxidizer Control Valve Pressure	0-1000
Oxidizer Primary Inlet Pressure	0-200
Oxidizer Divider Valve Pressure	0-200
Oxidizer Secondary Manifold Pressure	0-50
Oxidizer Primary Injection Differential Pressure	0-100
Fuel Run Tank Supply Pressure	0-5000
Fuel Run Tank Pressure	0-3000
Fuel Orifice Inlet Pressure	0-1500
Fuel Orifice Differential Pressure	0-150
Fuel Orifice Differential Pressure	0-150
Fuel Orifice Differential Pressure	0-100
Fuel Orifice Differential Pressure	0-100
Fuel Control Valve Pressure	0-1500
Fuel Injector Manifold Pressure	0-50
Fuel Injection Differential Pressure	0-15
Coolant Orifice Inlet Pressure	0-3000
Coolant Orifice Differential Pressure	0-20
Coolant Orifice Differential Pressure	0-20
Coolant Pressure Control Valve Pressure	0-3000
Coolant Jacket Inlet Pressure	0-3000
Coolant Jacket Exit Pressure	0-2000
Nozzle Extension Inlet Pressure	0-1500
Nozzle Extension Exit Pressure	0-1000
Chamber Pressure	0-50
Chamber Pressure	0-25
Chamber Pressure	0-50
Chamber Pressure	0-25
Chamber Pressure	0-100
Seal Cavity Orifice Pressure	0-300
Seal Cavity Orifice Differential Pressure	0-50
Seal Cavity Pressure	0-300
Half-Shell Pressure	0-15
Half-Shell Pressure	0-15
Half-Shell Pressure	0-15
Half-Shell Pressure	0-15

Temperatures	Range, ^{o}R
Oxidizer Nozzle Inlet Temperature	140-360
Oxidizer Nozzle Exit Temperature	140-360
CV 320 Body Temperature	140-540
CV 130 Body Temperature	140-540
Oxidizer Primary Inlet Temperature	140-360
Oxidizer Secondary Manifold Temperature	140-360

(U) Table XV. Instrumentation for Low Chamber Pressure Tests (Continued)

Fuel Orifice Inlet Temperature	460-600
Fuel Injector Manifold Temperature	460-600
Coolant Orifice Inlet Temperature	460-600
Coolant Jacket Inlet Temperature	460-600
Coolant Jacket Exit Temperature	500-1000
Nozzle Extension Inlet Temperature	500-1000
Nozzle Extension Exit Temperature	500-1000
Coolant Wall Chamber Temperature	500-1000
Coolant Wall Chamber Temperature	500-1000
Coolant Wall Throat Temperature	500-1000
Coolant Wall Throat Temperature	500-1000
Injector Coolant Exit Temperature	140-250
Run Line Jacket Vent Temperature	140-160
Oxidizer Sample Bottle Temperature	140-360
Miscellaneous	
CV 320 Position	0-100%
CV 130 Position	0-100%
CV 360 Position	0-100%
CV 140 Position	0-100%
CV 110 Position	0-100%
CV 150 Position	0-100%
Start Signal Voltage	
Prestart Signal Voltage	
Thrust	-9000
	-8000
Thrust	-9000
	-8000
Coolant Weight Flow	0-4 lb/sec
Mixture Ratio	6-16

2. Propellant Flow Measurements

(C) Fluorine was measured using convergent flow nozzles and hydrogen flow was measured using flow orifices. Three sets of nozzles and orifices were used to cover the following three chamber pressure ranges: (1) 850 to 300 psia, (2) 30 to 15 psia and (3) 10 to 5 psia. Table XVI gives the orifice and nozzle sizes used. Also given in the table are the transducer sizes used with the respective nozzles and orifices. The nozzle and orifice for the low chamber pressure tests were installed in close proximity to the low-thrust flow control valves to minimize errors resulting from storage effects in the supply lines, which are sized for maximum thrust. (See figure 100.) As in the previous 8.5K tests, fluorine temperature measurements were made both upstream and downstream of the flow nozzle and an average of the two measurements was used to calculate fluorine flow. Redundant measurements of orifice and nozzle pressure drops were also taken to improve accuracy. Furthermore, as indicated in table XVI, two size ΔP transducers were used to cover the 850 to 300 psia range. For fluorine nozzle pressure drop measurements, a 0-100 psid transducer was used in the 850, 750 and 600 psia

chamber pressure tests and a 0-25 psid transducer was used in the 450 and 300 psia test. For gaseous hydrogen flow, a 0-300 psid transducer was used for the 850, 750 and 600 psia tests and a 0-100 psid transducer was used in the 450 and 300 psia tests.

The equations used in computing flow rates are as follows.

LF_2:

$$\dot{w}_o = (AC_d)_o \sqrt{2g\rho_o \Delta P_o}$$

GH_2:

$$\dot{w}_f = (AC_d)_f \left(1 - \frac{K\,\Delta P_f}{P_f}\right) \sqrt{2g\rho_f \Delta P_f}$$

where:

$\dot{w}_o$ = fluorine flow

$\dot{w}_f$ = hydrogen flow

$(AC_d)_o$ = effective flow area of the oxidizer flow nozzle, see table XVI.

ρ_o = fluorine density, which is a function of temperature and pressure

ΔP_o = fluorine flow nozzle pressure drop

$(AC_d)_f$ = effective flow area of the fuel flow orifice see table XVI.

K = a factor that accounts for expansion through the orifice (Reference 9)

P_f = fuel flow orifice upstream pressure

ρ_f = fuel density which is a function of temperature and pressure

ΔP_f = fuel orifice pressure drop.

(C) Table XVI. LF_2 Nozzle and GH_2 Orifice Measurements

Pressure Range, psia	LF_2 Nozzle Dia, in.	LF_2 Nozzle AC_d, in^2	LF_2 Nozzle ΔP Transducer Range, psid	GH_2 Orifice Dia, in.	GH_2 Orifice AC_d, in^2	GH_2 Orifice ΔP Transducer Range, psid
850 to 600	0.7325	0.424	0-100	0.810	0.312	0-300
450 to 300	0.7325	0.424	0-25	0.810	0.312	0-100
30 to 15	0.140	0.0152	0-100	0.240	0.0297	0-150
10 to 5	0.088	0.0059	0-100	0.182	0.0154	0-100

(U) Errors in any of the measured or calibrated parameters in these equations introduce errors in the computed flow rate. The more significant sources of error include: (1) errors in the effective flow areas, which are determined on a flow bench, (2) flow orifice ΔP measurement errors, and (3) density errors resulting from the use of erroneous temperature measurements. The 3-sigma magnitude of these errors are given for several chamber pressure levels in table XVII. The errors were calculated by using the following basic instrumentation errors:

Absolute Pressure Transducers	$\pm$ 0.5% of full scale
ΔP Transducers	$\pm$ 0.6% of full scale
Thermocouples	$\pm$ 3°R
Resistance Thermometers	$\pm$ 1°R

With these errors, the computed 3-sigma errors, by the method described in (Reference 10), for propellant flows are as given in figure 106 for the high-pressure tests and figure 107 for the low-pressure tests.

(C) Table XVII. Propellant Flow Errors in ± %

P_c,	LF_2 Flow				GH_2 Flow				
psia	$(AC_d)_{ox}$	ΔP_{ox}	ρ_{ox}	W_{ox}	AC_d	ΔP_f	P_f	T_f	W_f
850	1.72	0.86	0.2	1.78	2.5	0.97	0.7	0.55	2.59
300	1.72	1.5	0.2	1.88	2.5	1.95	0.7	0.55	2.73
30	2.0	0.54	0.2	2.02	2.5	1.05	0.7	0.55	2.58
5	2.0	3.6	0.2	2.69	2.5	4.3	1.05	0.55	3.39

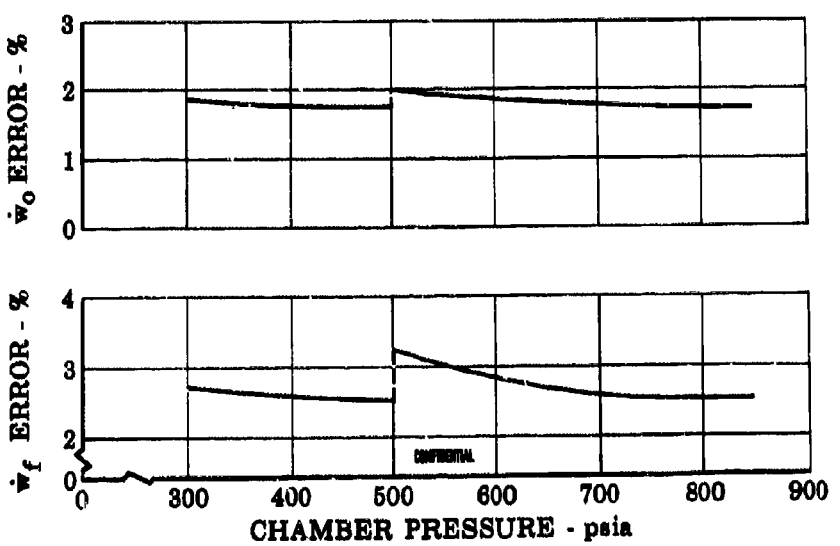

Figure 106. Flow Errors for High Chamber Pressure Tests FD 20938

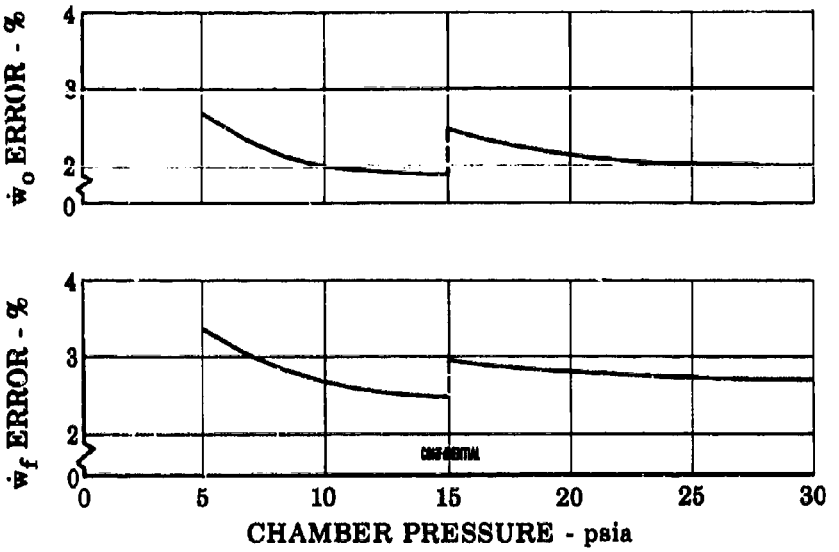

Figure 107. Flow Errors for Low P_c Tests FD 20963

3. Chamber Pressure Measurements

(U) Chamber pressure measurements were taken at two axial chamber locations: one at the injector face and another at the nozzle inlet. To accurately cover the chamber pressure range the transducers listed in table XVIII were used. With these transducers, the 3-sigma errors as a function of chamber pressure are as shown in figure 108 for the low-pressure tests and figure 109 for the high-pressure tests.

(C) Table XVIII. Pressure Transducers

P_c, psia	Pressure Transducer Range, psia
850, 750, and 600	0-1000
450 and 300	0-500
30, 25, and 20	0-50
15, 10, and 5	0-25

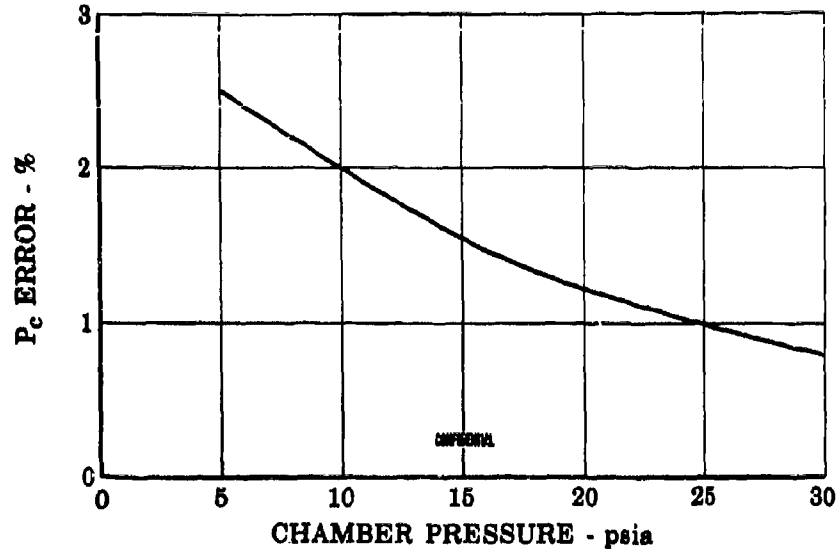

Figure 108. Chamber Errors for Low P_c Tests FD 20958

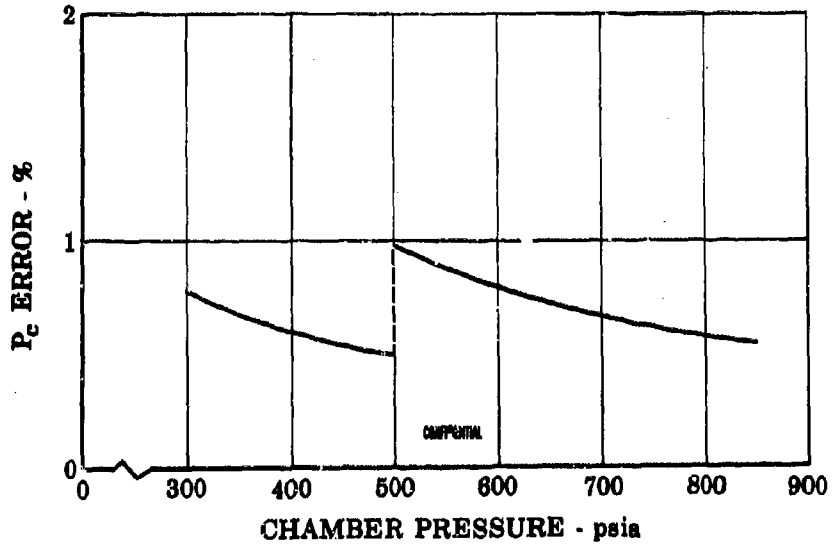

Figure 109. Chamber Pressure Errors for High P_c Tests FD 20962

4. Thrust Measurements

(U) Figure 110 shows the installation of the 8.5K engine with the RL10 nozzle extension in the LPRF altitude system. The measured engine vacuum thrust is dependent upon several factors that affect the accuracy of the thrust measurement. The equation for computing vacuum thrust is as follows:

$$F_{vac} = F_m + F_T + P_a A_a + P_{HS}(A_e - A_a)$$

where:

F_{vac} = vacuum thrust
F_m = measured thrust
F_T = test stand tare force
P_a = ambient pressure
A_a = engine projected area subjected to ambient pressure
A_e = engine exit area
P_{HS} = half-shell pressure.

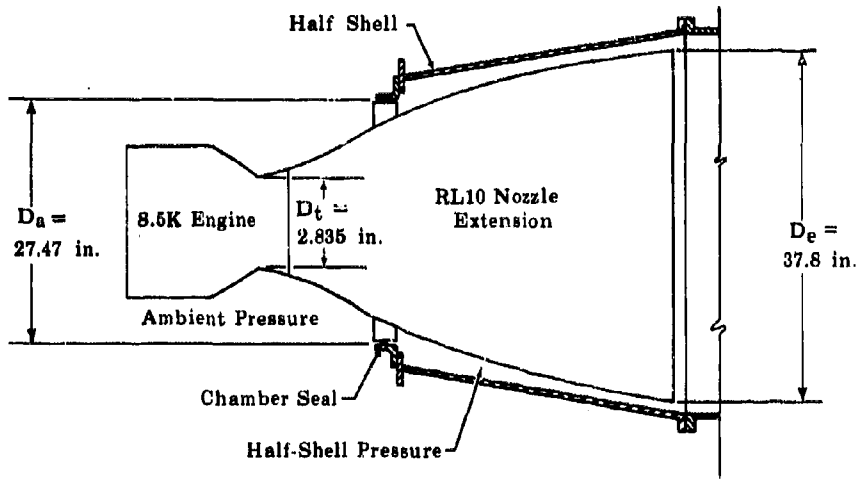

Figure 110. 8.5K Engine Installation in the Altitude System FD 14889A

(U) The accuracy of the vacuum thrust in the previous sea level tests was approximately ± 65 lb. This error results from a thrust system calibration error of approximately ± 45 lb and a tare measurement error of approximately ± 20 lb. In the altitude tests, measurement of the half-shell pressure resulted in an additional measurement error that could contribute approximately ± 35 lb. Thus, in the altitude tests, the thrust error was approximately ± 100 lb. Figure 111 presents the percentage error in the thrust measurements as a function of percentage thrust.

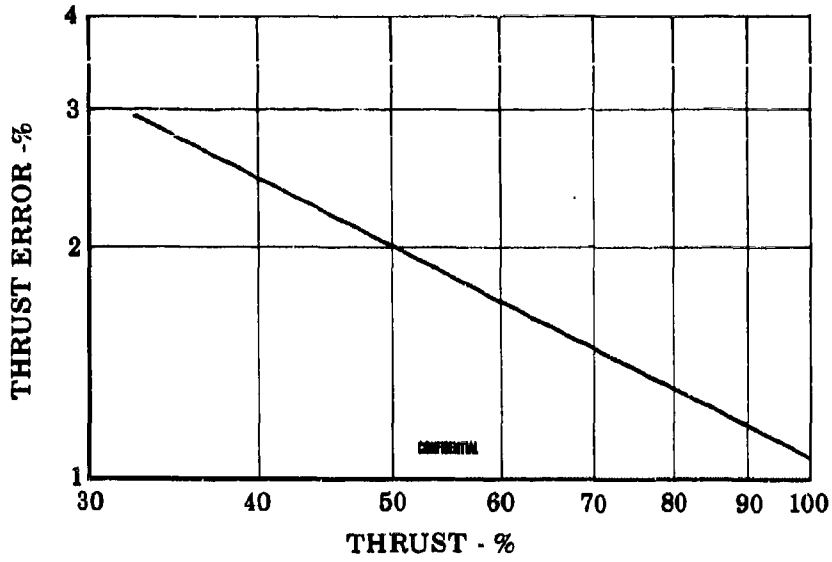

Figure 111. Thrust Error FD 20992

5. Characteristic Exhaust Velocity Data Errors

(U) The errors in propellant flow rates and chamber pressure introduce errors in the c* data. Also the error in the chamber throat area discharge coefficient introduces another error in the c* data. The calculated 3-sigma c* errors are given in figures 112 and 113 for the high- and low-pressure tests, respectively. Two curves are given. The lower curve is for only the propellant flow and chamber pressure errors, which are normally the only sources of error considered in c* data. The upper curve includes the error in the throat area discharge coefficient. The errors presented in these figures are representative of the c*-efficiency errors also because although there are errors in the reference mixture ratio and chamber pressure values used in determining the theoretical c* values, the theoretical c* curves are practically invariant for small changes in either mixture ratio or chamber pressure.

6. Specific Impulse Data Errors

(U) The combined effect of errors in thrust and propellant flow rates results in the specific impulse errors presented in figure 114. As for c* data errors, the specific impulse data and specific impulse efficiency data errors are essentially the same.

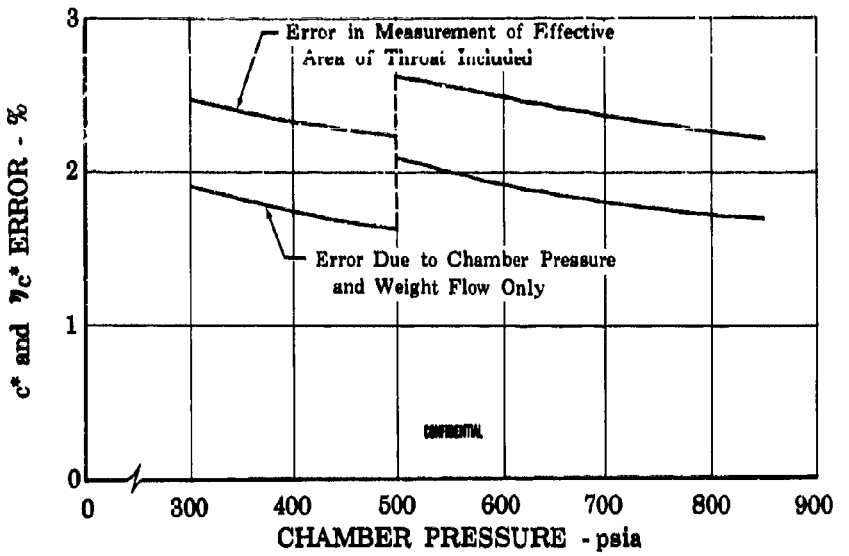

Figure 112. c* Performance Errors - High Chamber Pressure Tests

FD 20973

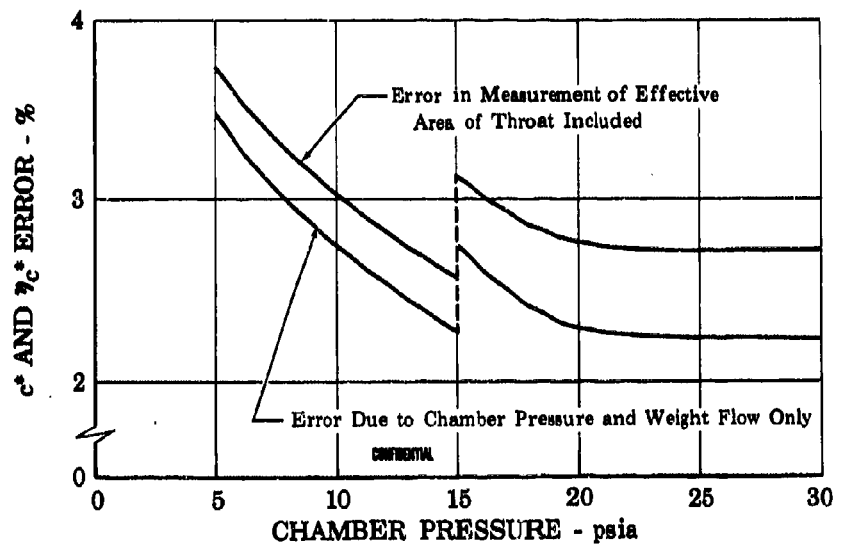

Figure 113. c* Performance Errors - Low Chamber Pressure Tests

FD 20959

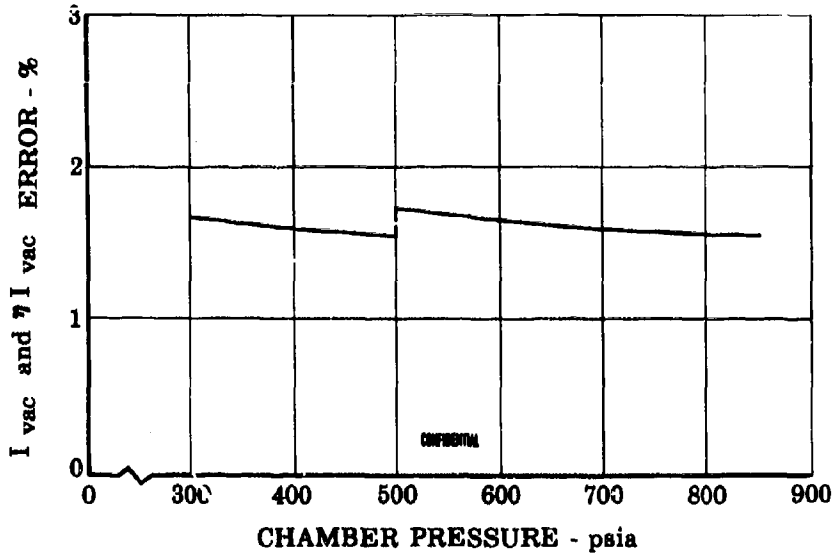

Figure 114. I_{vac} Performance Errors FD 20960

APPENDIX I
DUAL ORIFICE INJECTOR CONCEPT

(C) Dual-orifice injectors have two separate injection paths and injector orifices for the propellant. The two injector orifices are concentric, as shown in the dual-orifice element detail in figure 115. The inner orifice is the primary injector; the outer orifice is the secondary injector. The stream from the primary orifice has a high velocity at all levels of thrust; the velocity of the secondary stream decreases with decreasing thrust as with a fixed thrust injector. High-fluid-injection velocities, which are required for combustion stability and which enhance propellant mixing and thereby provide high combustion efficiency, are provided over a wide flow range by the dual-orifice injector system because of the pumping effect of the high velocity, low flow rate primary stream on the surrounding concentric low velocity, high flow rate secondary stream.

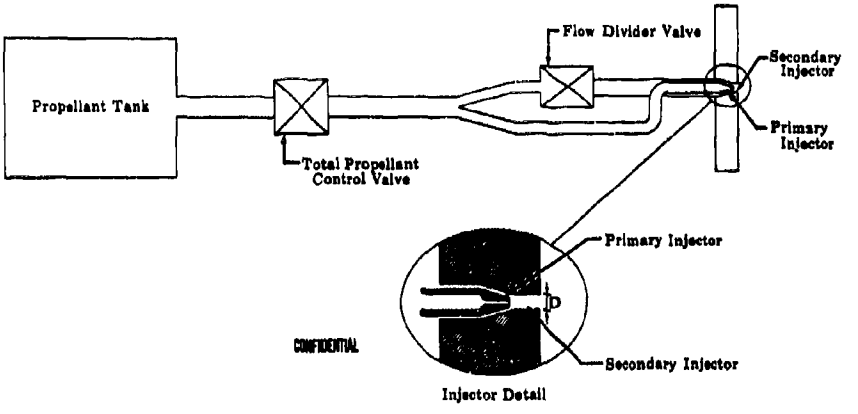

Figure 115. Dual-Orifice Injector Flow System Schematic FD 7530A

(C) Dual-orifice injectors are fixed-area injectors. Flow control (and therefore thrust control), as well as control of the primary-to-secondary injector flow split is accomplished by flow control valves located upstream of the injector (as shown schematically in figure 115). This method of controlling flow avoids the complexities and problems associated with mechanisms exposed to the hot combustion gases, or the inherently difficult and dangerous practice of incorporating sliding seals in propellant passages internal to the injector.

(C) At a high flow rate (high thrust level), where the injector pressure drop is high, almost all the flow is programed through the large-injection-area secondary passages. As the total flow rate is reduced, the primary-to-secondary flow ratio is increased until at the minimum flow level all or almost all the flow is programed through the small-injection-area primary passages. Therefore, high fluid injection velocities are maintained over very wide ranges of flow and thrust.

(U) Dual-orifice injector systems have been used successfully for years for fuel injection in turbojet engines. The feasibility of dual-orifice injector systems for use in liquid bipropellant rocket engines was demonstrated experimentally for the storable propellants N_2O_4/50% N_2H_4-50% UDMH under Contract AF 04(611)-9575 and for fluorine/hydrogen propellants under Contract AF 04(611)-9965.

(C) The dual-orifice principle can be used in most conventional liquid bipropellant rocket injector patterns. In Contract AF 04(611)-9575, dual-orifice injectors having impinging elements were evaluated with storable propellants. In that contract two 15,000-lb (maximum) thrust injectors were tested: one had 2-fuel-on-1 oxidizer triplet elements and the other had 2-fuel-on-2 oxidizer quadruplet elements.

(C) The dual-orifice fluorine/hydrogen injectors that were tested under Contract AF 04(611)-9965 and this contract have concentric-type injection elements with the fuel being injected from annular orifices surrounding the oxidizer injector spuds as shown in figure 116. These injectors were evaluated for potential use in a pump-fed regeneratively cooled engine in which thrust modulation is accomplished by P_c throttling. Dual-orifice injectors were used only for the liquid fluorine and not for the gaseous hydrogen fuel.

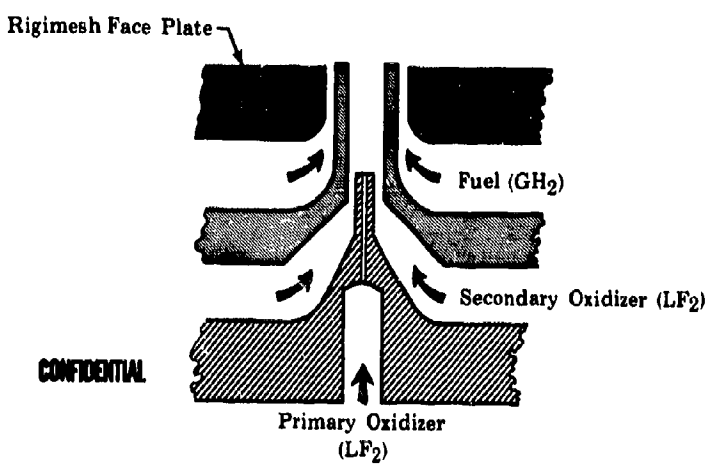

Figure 116. Dual-Orifice Injection Element for Liquid Fluorine/Gaseous Hydrogen Propellants FD 11265B

APPENDIX II
PERFORMANCE PARAMETER DEFINITIONS

1. Test Duration and Scan Time

(U) The scan time, data average period, and test duration are identified in the sketch below:

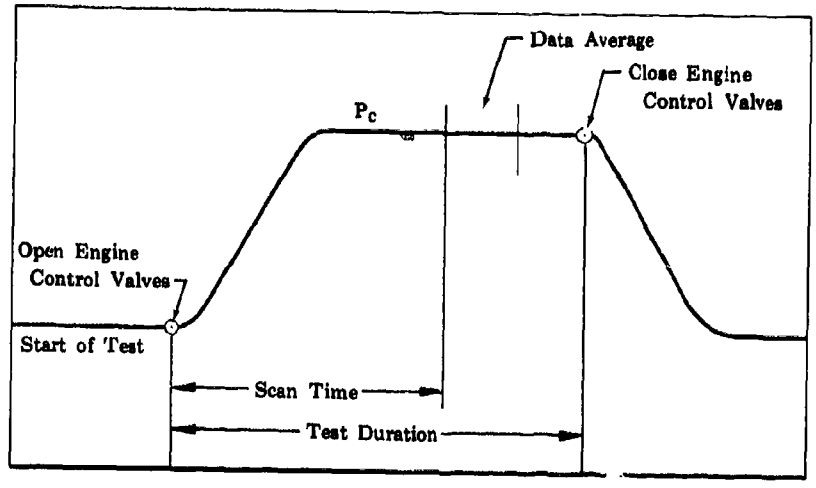

Figure 117. Typical P_c Trace Showing Base for Firing Duration and Data Period FD 20929

2. Chamber Pressure, P_c

(U) When P_c used was measured at the injector face, it was corrected for momentum losses of 0.5% to obtain throat stagnation pressure. The P_c measured at the nozzle entrance was used directly as the throat stagnation pressure.

3. Percentage Thrust

(U) $$\text{Thrust - \%} = \frac{P_c \times 100}{850 \text{ (maximum nominal } P_c)}$$

4. Total Propellant Flow, $\dot{w}_t$

(U) $\dot{w}_t = \dot{w}_f + \dot{w}_o$

5. Mixture Ratio, r

(U) $r = \dot{w}_o/\dot{w}_f$

6. Characteristic Exhaust Velocity, c*

(U) $$c^* = \frac{P_c (AC_d)_t \, g}{\dot{w}_t}$$

where $(AC_d)_t$ is the throat effective area determined from cold flow data.

7. Characteristic Exhaust Velocity Efficiency, η_{c^*}

(U) $$\eta_{c^*} = \frac{c^*}{c^*_c} \times 100$$

where c^*_c is the theoretical shifting equilibrium characteristic exhaust velocity corrected for heat loss to the chamber.

8. Vacuum Thrust for Altitude Tests, F_{vac}

(U) F_{vac} = Measured Thrust - Tare + (Half-Shell Pressure)(553.14) + (Ambient Pressure)(592.66)

9. Vacuum Thrust for Sea Level Tests, F_{vac}

(U) F_{vac} = Measured Thrust + (Ambient Pressure)$(A_t)(\epsilon)$

where ϵ = expansion ratio for sea level chamber = 4.2.

10. Vacuum Specific Impulse, I_{vac}

(U) $$I_{vac} = \frac{F_{vac}}{\dot{w}_t}$$

11. Vacuum Specific Impulse Efficiency, $\eta_{I_{vac}}$

(U) $$\eta_{I_{vac}} = \frac{I_{vac}}{(I_{vac})_c}$$

where $(I_{vac})_c$ is the theoretical shifting equilibrium vacuum specific impulse corrected for heat loss.

12. Thrust Coefficient Efficiency

(U) $$\eta_{C_F} = \frac{I_{vac}}{\eta_{c^*}}$$

13. Oxidizer Primary Injector Pressure Drop, ΔP_p

(U) ΔP_p = Measured pressure drop across the primary injection orifices

14. Oxidizer Secondary Injector Pressure Drop, ΔP_s

(U) ΔP_s = Measured pressure drop across the secondary injection orifices

15. Oxidizer Average Injection Velocity, $(Vo)_{avg}$

(C) $$(Vo)_{avg} = \frac{\frac{\dot{w}_p^2 \times 144}{\rho_p A_p} + \frac{\dot{w}_s^2 \times 144}{\rho_s A_s}}{\dot{w}_o}$$

16. Fuel Injector Pressure Drop, ΔP_f

(U) ΔP_f = Measured pressure drop across the fuel injection orifices

17. Fuel Injection Velocity, V_f

(U) $$V_f = \left[\gamma g R T_t\right]^{1/2} \left\{\left[\left(\frac{P_c}{P_t}\right)^{\frac{1-\gamma}{\gamma}} - 1\right] \frac{2}{\gamma - 1}\right\}^{1/2}$$

18. Momentum Ratio, MR

(U) $$MR = \frac{K V_f \dot{w}_f}{(Vo)_{avg} \dot{w}_o}$$

where K equals 0.6315 and is the ratio of the fuel effective areas to the total fuel orifice and faceplate effective areas

19. Oxidizer Primary-to-Total Flow Split, FS

(C) For the low chamber pressure tests, the flow split was calculated based on pure liquid flow through both the primary and secondary oxidizer injection orifices. Some vaporization takes place in both manifolds especially at the very low chamber pressures. However, for comparison purposes the theoretical flow split is used.

For high chamber pressures:

$$FS = \frac{\dot{w}_p}{\dot{w}_o} \times 100$$

20. Peak-to-Peak Chamber Pressure Oscillations

(U) $\frac{\Delta P_c}{P_c}$ = Ratio of the peak-to-peak chamber pressure oscillations to the mean level of chamber pressure

APPENDIX III
B-29 THRUST SYSTEM INVESTIGATIONS

(U) Post-test analysis of the test data acquired at chamber pressure levels of 300, 450, and 600 psia (tests No. 9, 10, and 11, respectively) indicated that the associated thrust levels were erroneously high.

(U) As thrust is calculated from the algebraic addition of net measured and existing pressure area force terms, it was first suspected that nozzle separation and the attendant use of nozzle exit rather than separation area had given rise to the erroneous thrust values. Subsequent analysis indicated that nozzle separation would not occur at chamber pressure levels in excess of approximately 250 psia.

(U) Further analysis clearly showed (figures 118 and 119) the problem to be associated with thrust system binding. Figure 118 depicts the rate of change of thrust for both the start and shutdown transients on the 600-psia chamber pressure tests. Because of low chamber pressure nozzle separation and erratic early transient half-shell pressures resulting from diffuser starting characteristics, only start transient data above a chamber pressure of 300 psia are considered valid. For chamber pressures above 300 psia, an estimate of what the vacuum thrust (F_{vac}) should be can be made by assuming a 95% thrust coefficient efficiency. When the measured F_{vac} values taken during the start and shutdown transients are compared to this curve, the following can be noted. First, during the start transient and at chamber pressures in the 300 to 400 psia range, the measured F_{vac} is above the estimated curve, indicating that the thrust system is binding. Between 400 and 450 psia chamber pressure, the system apparently broke loose, although the curve is still erratic. Above 500 psia, the slope of the measured F_{vac} curve is greater than the estimated F_{vac} curve. Furthermore, the measured F_{vac} value at 600 psia is above the estimated F_{vac} value. Based on this data, it is believed that below the 500 psia level thrust system binding occurred, which, when freed, resulted in a thrust overshoot to the level seen at a chamber pressure of 600 psia.

(U) The shutdown transient is seen to be much less erratic than that of the start. Post-test inspection of the rig revealed that the rig-to-diffuser seal had shaken loose during the hot firing permitting increased rig freedom of movement.

(U) Figure 119 depicts the thrust, chamber pressure, half-shell pressure, flow rate, and measured force with respect to time for the 600-psia test. Note that thrust decayed at all mixture ratios throughout the test independent of changes in the remaining parameters. This decay served only to further emphasize the previously drawn conclusion concerning thrust system binding.

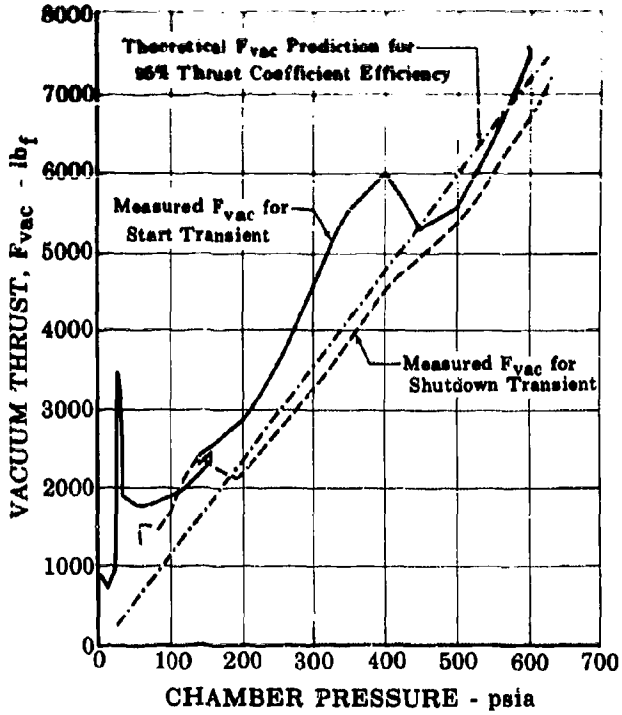

Figure 118. Variation of Vacuum Thrust With Chamber Pressure (Test No. 11) FD 20966

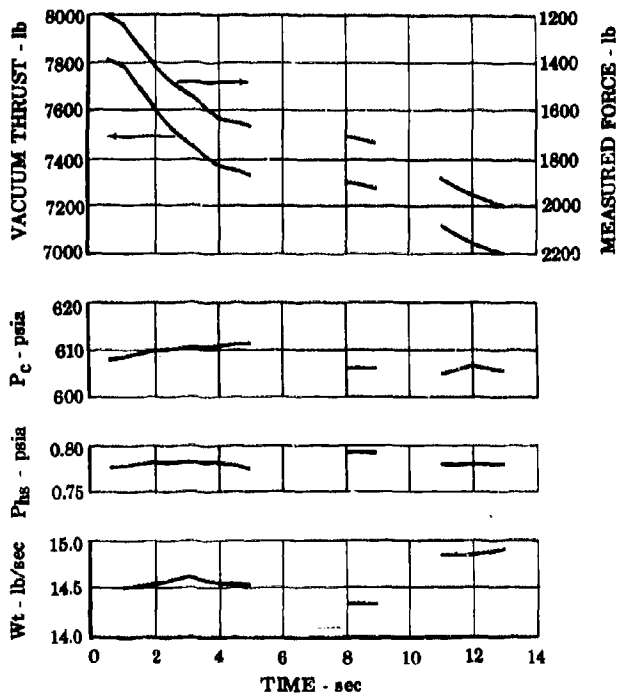

Figure 119. Steady-State Performance Parameters (Test No. 11) FD 20956

(U) An extensive investigation was immediately undertaken to uncover and eliminate all possible sources of thrust system binding. Discovered as possible sources of system binding were the following:

1. Post-test rig inspection revealed a badly scarred Teflon O-ring in the rig to diffuser seal as well as a deformed horizontal gimbal arm mount bracket, both of which it was believed could have contributed to the problem.

2. Rig axial and circumferential thermal growth might possibly result in communication between the rig and diffuser.

3. Rig installation was found to be offset in such a fashion that thermal growth would only give rise to diffuser-to-rig interference.

4. Rig-to-diffuser seal tightness could possibly result in rig-to-diffuser interference.

(U) Item No. 1 resulted in the immediate replacement and repair of the O-ring and bracket, respectively.

(U) Existing rig installation procedures were found to be sufficiently adequate to preclude item No. 2 as a possible thrust error source.

(U) Rig installation procedures were modified in such a manner as to correct the offset error set forth in item No. 3.

(U) Rig-to-diffuser seal installation procedures were established and verified through a series of thrust calibration tests. Seal installation techniques were varied in these tests until differences between the thrust system calibrations with the seal removed and with the seal installed were minimized.

(U) A special thrust tare investigation test was then accomplished to define the contributions of the various stand pressures and temperatures to total system tare.

(U) Using procedures established during the above investigation subsequent hot firings were accomplished at chamber pressure levels of 300, 750, and 850 psia. Pretest to post-test and test to test tare values are summarized below and were found to be in close agreement with that determined during the investigation.

Test No.	Chamber Pressure, psia	Pretest Tare, lb_f*	Post-Test Tare, lb_f*
9	300	328.9	302.1
10	750	345.4	327.3
11	850	306.5	–

*Data adjusted to ambient stand calibration base.

The absence of previously encountered thrust problems and tare repeatability demonstrated by these tests gives rise to confidence in the fact that adherence to the revised rig and seal installation techniques will yield thrust and nozzle performance values of high quality.

APPENDIX IV
FLOW NOZZLE AND ORIFICE CALIBRATION

(U) Propellant flow to the 8.5K injector was metered with orifices and nozzles. Fluorine was measured using convergent flow nozzles and hydrogen flow was measured with flow orifices. Prior to testing, the nozzles and orifices were calibrated over the range of Reynolds numbers that were to be encountered during testing.

(C) The three sets of orifices used to cover the following three chamber pressure ranges (1) 850 to 300 psia, (2) 30 to 15 psia and (3) 10 to 5 psia were calibrated with air. The equation for computing flow rate was written in the following form.

$$\dot{w}_f = (AC_d)\left(1 - \frac{K\Delta P_f}{P_f}\right)\sqrt{2g\rho_f \Delta P_f}$$

The flow coefficient, C_d, was determined by calibration. The variation of discharge coefficient with Reynolds number (figure 120), is sufficiently small enough to have negligible effect on weight flow and mixture ratio calculations. The expansion coefficient, K, which is a function of orifice geometry, was determined from ASME data.

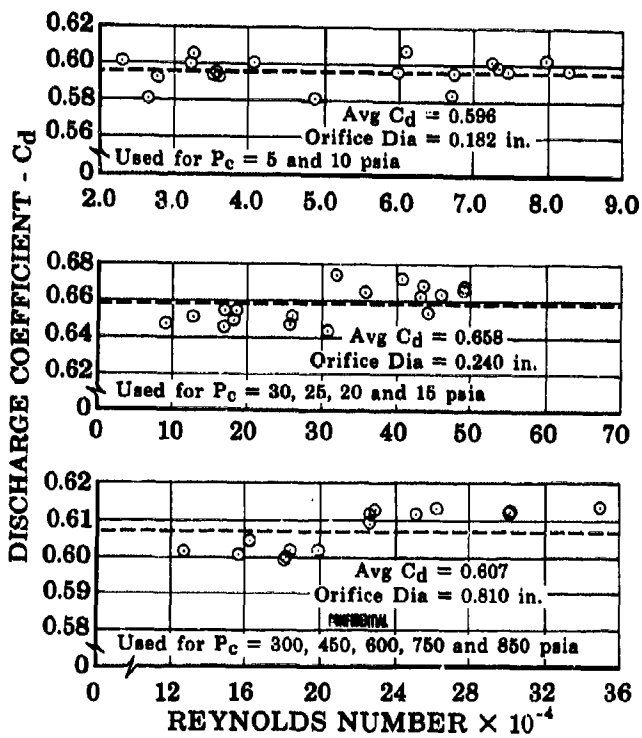

Figure 120. Hydrogen Flow Orifice Discharge Coefficients FD 20935

(C) The largest hydrogen-flow orifice used for the 300- to 850-psia chamber pressure tests was not calibrated until after testing. However, the weight flow equation, as predicted by ASME data, did not differ greatly enough from the calibration equation to introduce significant errors in weight flow calculations.

(C) The fluorine nozzles used to cover the 30 to 15 psia and 10 to 5 psia chamber pressure ranges were calibrated with air at the Reynolds number range anticipated during testing. Liquid oxygen was used to calibrate the nozzle used in the high chamber pressure tests. It was necessary to use liquid oxygen to obtain a Reynolds number similar to that anticipated in testing. The fluorine nozzle discharge coefficients appear in figure 121 as functions of Reynolds number.

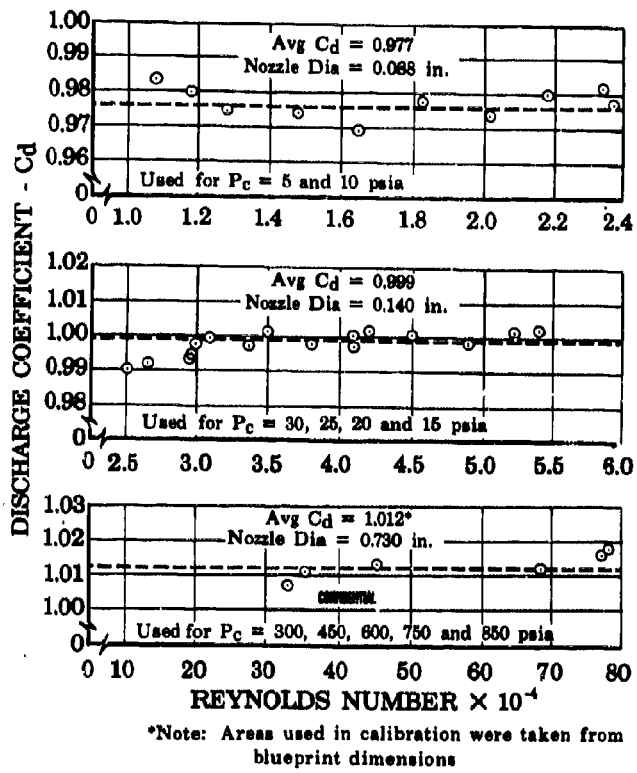

Figure 121. Fluorine Flow Nozzle Discharge Coefficients FD 20934

APPENDIX V
REFERENCES

1. "Final Report of High Energy Advanced Throttling Concept Study," Contract AF 04(611)-9965, AFRPL-TR-66-43, PWA Report No. FR-1573, 7 March 1966 (Confidential).

2. "Digital Computer Programs for Rocket Nozzle Design and Analysis," Volume III, PWA FR-1021.

3. "Journal of Fluid Mechanics," Bray, K. N. C., Volume 6, No. 1, 1959.

4. "Rocket Propulsion Elements," Sutton, G. P., John Wiley and Sons, Inc. Third Edition, 1963.

5. "Performance Characteristics of Compound A/Hydrazine Propellant Combinations," Contract AF 04(611)-9573, May 1965 (Confidential).

6. "Fluid Meters, Their Theory and Application," The American Society of Mechanical Engineers, New York, N. Y., 1959.

7. "Materials of Construction for Handling Fluorine," White, Earl L. and Frederick W. Fink, Proceedings of the Propellant Thermodynamics and Handling Conference, 20-21 July 1959.

8. "Flow Separation in a Rocket Nozzle," Schilling, M. T., M. S. Thesis University of Buffalo, Buffalo, New York, June 1962.

9. Report of ASME Research Committee on Fluid Meters, 1959.

10. "Mathematical Formulation of Tolerancy by the Statistical or Differential Method: Mean and Variances of Functions of One or More Variables," Berretoni, J. N., Western Reserve University.

CONFIDENTIAL
Security Classification

DOCUMENT CONTROL DATA - R&D
(Security classification of title, body of abstract and indexing annotation must be entered when the overall report is classified)

1. ORIGINATING ACTIVITY (Corporate author) Pratt & Whitney Aircraft Division of United Aircraft Corporation Florida Research and Development Center	2a. REPORT SECURITY CLASSIFICATION Confidential 2b GROUP 4

3. REPORT TITLE

Final Report of High Energy Advanced Throttling Concept Study

4. DESCRIPTIVE NOTES (Type of report and inclusive dates)

Final Report, May 1966 to May 1967

5. AUTHOR(S) (Last name, first name, initial)

Mitchell, James P.

6. REPORT DATE	7a. TOTAL NO. OF PAGES	7b. NO. OF REFS
15 May 1967	130	10

8a. CONTRACT OR GRANT NO. AF 04(611)-11611 b. PROJECT NO. 3058 c. BPSN: 623058 d. Program Element No.: 62405184	9a. ORIGINATOR'S REPORT NUMBER(S) PWA FR-2366 9b. OTHER REPORT NO(S) (Any other numbers that may be assigned this report) AFRPL-TR-67-140

10. AVAILABILITY/LIMITATION NOTICES

Qualified requestors may obtain copies of this report from DDC.

11. SUPPLEMENTARY NOTES	12. SPONSORING MILITARY ACTIVITY
	Rocket Propulsion Laboratory Air Force Systems Command Edwards Air Force Base, California

13. ABSTRACT

This report presents the results of an experimental program conducted under Contract AF 04(611)-11611 to evaluate (1) the throttling capability of dual-orifice injectors with F_2/H_2 propellants and (2) performance of the F_2/H_2 propellants in a high-expansion-ratio (180 to 1) thrust chamber. In the program, 15 combustion firing tests were made with an 8500-lb maximum thrust dual-orifice-injector-chamber assembly at simulated altitude conditions. Tests were made at chamber pressures from 850 to 5 psia, and therefore over a throttling range of 170 to 1. The 6 to 14 mixture ratio range was evaluated. Extremely high performance was recorded in the test program. Specific impulse values of from 441 to 475 seconds were measured at high chamber pressures. Outstanding injector and chamber hardware durability were demonstrated. The total test time accumulated in the tests was 1032 seconds, the longest test being of 184 seconds duration.

DD FORM 1473

CONFIDENTIAL
Security Classification

14. KEY WORDS	LINK A		LINK B		LINK C	
	ROLE	WT	ROLE	WT	ROLE	WT
Throttling						
Variable Thrust						
Dual-Orifice Injector						
Manuevering Satellite Applications						
Fluorine/Hydrogen						

INSTRUCTIONS

1. ORIGINATING ACTIVITY: Enter the name and address of the contractor, subcontractor, grantee, Department of Defense activity or other organization *(corporate author)* issuing the report.

2a. REPORT SECURITY CLASSIFICATION: Enter the overall security classification of the report. Indicate whether "Restricted Data" is included. Marking is to be in accordance with appropriate security regulations.

2b. GROUP: Automatic downgrading is specified in DoD Directive 5200.10 and Armed Forces Industrial Manual. Enter the group number. Also, when applicable, show that optional markings have been used for Group 3 and Group 4 as authorized.

3. REPORT TITLE: Enter the complete report title in all capital letters. Titles in all cases should be unclassified. If a meaningful title cannot be selected without classification, show title classification in all capitals in parenthesis immediately following the title.

4. DESCRIPTIVE NOTES: If appropriate, enter the type of report, e.g., interim, progress, summary, annual, or final. Give the inclusive dates when a specific reporting period is covered.

5. AUTHOR(S): Enter the name(s) of author(s) as shown on or in the report. Enter last name, first name, middle initial. If military, show rank and branch of service. The name of the principal author is an absolute minimum requirement.

6. REPORT DATE: Enter the date of the report as day, month, year; or month, year. If more than one date appears on the report, use date of publication.

7a. TOTAL NUMBER OF PAGES: The total page count should follow normal pagination procedures, i.e., enter the number of pages containing information.

7b. NUMBER OF REFERENCES: Enter the total number of references cited in the report.

8a. CONTRACT OR GRANT NUMBER: If appropriate, enter the applicable number of the contract or grant under which the report was written.

8b, 8c, & 8d. PROJECT NUMBER: Enter the appropriate military department identification, such as project number, subproject number, system numbers, task number, etc.

9a. ORIGINATOR'S REPORT NUMBER(S): Enter the official report number by which the document will be identified and controlled by the originating activity. This number must be unique to this report.

9b. OTHER REPORT NUMBER(S): If the report has been assigned any other report numbers *(either by the originator or by the sponsor)*, also enter this number(s).

10. AVAILABILITY/LIMITATION NOTICES: Enter any limitations on further dissemination of the report, other than those imposed by security classification, using standard statements such as:

(1) "Qualified requesters may obtain copies of this report from DDC."

(2) "Foreign announcement and dissemination of this report by DDC is not authorized."

(3) "U. S. Government agencies may obtain copies of this report directly from DDC. Other qualified DDC users shall request through _____."

(4) "U. S. military agencies may obtain copies of this report directly from DDC. Other qualified users shall request through _____."

(5) "All distribution of this report is controlled. Qualified DDC users shall request through _____."

If the report has been furnished to the Office of Technical Services, Department of Commerce, for sale to the public, indicate this fact and enter the price, if known.

11. SUPPLEMENTARY NOTES: Use for additional explanatory notes.

12. SPONSORING MILITARY ACTIVITY: Enter the name of the departmental project office or laboratory sponsoring *(paying for)* the research and development. Include address.

13. ABSTRACT: Enter an abstract giving a brief and factual summary of the document indicative of the report, even though it may also appear elsewhere in the body of the technical report. If additional space is required, a continuation sheet shall be attached.

It is highly desirable that the abstract of classified reports be unclassified. Each paragraph of the abstract shall end with an indication of the military security classification of the information in the paragraph, represented as *(TS)*, *(S)*, *(C)*, or *(U)*.

There is no limitation on the length of the abstract. However, the suggested length is from 150 to 225 words.

14. KEY WORDS: Key words are technically meaningful terms or short phrases that characterize a report and may be used as index entries for cataloging the report. Key words must be selected so that no security classification is required. Identifiers, such as equipment model designation, trade name, military project code name, geographic location, may be used as key words but will be followed by an indication of technical context. The assignment of links, roles, and weights is optional.